Investigating the phase space dynamics of conservative dynamical systems by the Lagrangian descriptors method.

Sebastian Zimper
ZMPSEB001

Thesis presented for the degree
Master of Science in Applied Mathematics

Supervisor: Associate Professor Haris Skokos
Co-supervisor: Dr Arnold Ngapasare

Department of Mathematics and Applied Mathematics
University of Cape Town
South Africa
May 2023

Abstract

In this work, we numerically investigate the dynamics of conservative dynamical systems using the method of Lagrangian descriptors (LDs), which has been extensively used to visualise characteristic features (like fixed points, periodic orbits and their associated manifolds) in the phase space of nonlinear dynamical systems. The computation of LDs is based on the accumulation of a positive scalar value along any orbit of the dynamical system, making them a rather easily evaluated quantity. Firstly, we use the method of LDs to study the escape of stars in an analytic model of a rotating galaxy. We find that the LDs are able to visually describe the lobe structure of manifolds which govern the escape of stars, thereby providing a computationally cheap and simple way to depict and analyse the model's phase space structures. Secondly, we develop and validate chaos detection techniques which use computations of the LDs of nearby orbits, to characterise the chaoticity of generic conservative systems. More specifically, we introduce the difference and ratio of the LDs of neighbouring orbits as chaos detection diagnostics, and include in our study a quantity related to the second spatial derivative of LDs, which was recently developed by other researchers. Applying these techniques to three basic, prototypical models, namely the two degrees of freedom Hénon-Heiles system, the two-dimensional (2D) standard map, and the 4D standard map, we find that these indices identify chaotic orbits with an accuracy of $\gtrsim 90\%$ when compared to the Smaller Alignment Index (SALI) method, which is a well-established chaos detection technique. Furthermore, we determine the effect on the indices' performance of (i) the orbits' integration time, (ii) the grid spacing between the considered neighbouring orbits, (iii) the number and arrangement of the nearby orbits used to evaluate the indicators and (iv) the overall extent of chaos in the system. A basic outcome of our work is that these indicators can be used to efficiently characterise chaotic behaviour of both low and high-dimensional dynamical systems at short integration times, without solving the so-called variational equations for continuous time systems, or evaluating the tangent map for discrete time models, needed by other, traditional chaos detection techniques.

Acknowledgements

I want to thank my supervisor, Associate Professor Haris Skokos, and co-supervisor, Dr Arnold Ngapasare, for their invaluable input and continuous support. I would also like to thank my colleagues in the Nonlinear Dynamics and Chaos group (Dr Malcolm Hillebrand, Henok Moges, Samuel Cheong, Jean-Jacq du Plessis, Sané Erasmus, and Dylan Theron) for the useful discussions and help in editing my thesis, as well as Professor Steve Wiggins and Dr Matthaios Katsanikas for their collaboration in the two papers emanating from this thesis. Lastly, I would like to thank the Center for High-Performance Computing and the High-Performance Computing facility of UCT, for providing the computational facilities used for this work.

Publications related to this work

Parts of the work in this thesis have been presented in the following papers:

1. M. Hillebrand, **S. Zimper**, A. Ngapasare, M. Katsanikas, S. Wiggins, and Ch. Skokos. Quantifying chaos using Lagrangian descriptors. *Chaos: An Interdisciplinary Journal of Nonlinear Science*, 32(12), 2022.

2. **S. Zimper**, A. Ngasapare, M. Hillebrand, M. Katsanikas, S. Wiggins, and Ch. Skokos. Performance of chaos diagnostics based on Lagrangian descriptors. Application to the 4D standard map. 2023. Available on the arXiv at https://arxiv.org/abs/2305.00978.

Contents

List of abbreviations

- dof: degrees of freedom
- ftmLE: finite time maximal Lyapunov Exponent
- HPC: high performance computing
- IC: initial condition
- LD: Lagrangian descriptor
- mLCE: maximal Lyapunov Characteristic Exponent
- ND: N-dimensional
- PSS: Poincaré surface of section
- RK: Runge-Kutta
- SALI: Smaller Alignment Index
- SVD: singular value decomposition

Chapter 1

Introduction

The mathematical modelling of processes using either systems of differential equations for continuous times, or iterative maps for discrete times, is fundamental to numerous scientific disciplines. The majority of these models are nonlinear and therefore typically do not permit analytical solutions. To describe the solutions of nonlinear models, a variety of numerical techniques have been developed to give either a qualitative or quantitative description of the system. Qualitative descriptions rely on a visual inspection of the properties of the system, in general giving information faster and on a larger scale than quantitative descriptions. Quantitative descriptions give exact information about the system, be it the location of specific solution classes or a characterisation of the properties of these solutions. The information gained from a qualitative analysis can then be used to identify regions of interest in the solution space of the system, where a more exact description using quantitative methods can be found.

Fixed points, periodic orbits and their associated stable and unstable manifolds form the most basic structures in the solution space of a dynamical system. Knowledge of these basic structures gives one a great deal of information on how generic solutions of the dynamical system behave. A key characteristic of a dynamical system is its chaoticity. Chaos is a phenomenon in nonlinear dynamical systems where some solutions appear as random, even though they are governed by deterministic equations. This is due to the solutions of a chaotic system being extremely sensitive to the initial conditions (ICs). Chaos has been an ongoing field of study in nonlinear dynamics, where a variety of quantitative indicators have been developed to detect chaotic orbits.

The novel contributions of our work are twofold. Firstly, we apply the recently developed qualitative technique, the method of Lagrangian descriptors (LDs) [1], to study the dynamics of a rotating galactic potential, i.e., a dynamical system which models the motion of stars in a galaxy [2]. Specifically, we demonstrate how LDs can be used to visualise the lobe structures created by the manifolds of two

unstable periodic orbits which govern the escape of stars from the potential well.

Secondly, based on LDs, we develop quantitative chaos detection indicators to study orbits of generic systems. We introduce two chaos quantifiers, the difference and ratio of the LDs of nearby orbits (the D_L^n and R_L^n indices respectively) and we also study the second derivative of the LDs (S_L^n), which is a chaos quantifier initially presented in [3]. The ability of these indices to correctly characterise orbits as regular or chaotic is tested in various prototypical conservative dynamical systems: the Hénon-Heiles system [4], the two-dimensional (2D) standard map [5], and the 4D standard map [6]. We find that these indicators are accurate for $\gtrsim 90\%$ of cases when compared to a standard chaos indicator, the Smaller Alignment Index (SALI) [7].

The thesis is organised as follows. In Chapter 2, the theoretical background and existing literature for the various topics of this work are discussed in detail, emphasising the numerical techniques we implement in our investigations. In Chapter 3, the results from applying LDs to study a galactic potential are presented. In Chapter 4, the quantitative chaos detection techniques based on LD calculations are introduced and their application to three test systems is studied. Some of the results from this chapter are presented in [8, 9]. Lastly, in Chapter 5, the conclusions of this thesis are given.

Chapter 2

Theoretical background and literature review

2.1 Dynamical systems

Differential equations lay the foundation for mathematically modelling any process that evolves continuously in time and space, while maps are used to model iteratively evolving processes. The mathematical study of systems of differential equations and maps, referred to in general as dynamical systems, is therefore extremely important. Such systems can be split into two categories: linear and nonlinear systems. Linear systems consist of only linear terms (the variables of the system are at most of degree one), while nonlinear ones have one or more nonlinear terms (at least one of the variables of the system does not have a degree of zero or one). Analytical solutions to linear differential equations can usually be found in a straightforward manner, but for nonlinear differential equations, in general, no analytical solutions exist [10]. Poincaré was the first to use a qualitative description to study nonlinear dynamical systems in [11]. Since this pioneering work, a variety of qualitative and quantitative techniques have been developed to study nonlinear dynamical systems and their solution structures.

2.1.1 Differential equations and iterative maps

Let us briefly recall some of the basic aspects of ordinary differential equations. We note that the materials covered in this section are adapted from the discussion found in Chapter 1 of [10].

In general a system of differential equations has the form

$$\dot{\mathbf{x}} = \mathbf{f}(\mathbf{x}, t), \quad \mathbf{x} \in \mathbb{R}^N, \tag{2.1}$$

where the dot ($\dot{}$) represents the derivative with respect to time t, $\mathbf{x}$ is a real vector (often called the "state vector") and $\mathbf{f}$ a vector field which is defined for some subset $S \subset \mathbb{R}^N$. If $\mathbf{f}$ is explicitly independent of t, (2.1) is called an autonomous system, while if $\mathbf{f}$ has explicit time dependency, (2.1) is called non-autonomous. The vector field $\mathbf{x}$ generates a flow $\boldsymbol{\phi}(\mathbf{x}, t)$ which is a smooth function, satisfying equation (2.1), i.e.,

$$\frac{d}{dt}(\boldsymbol{\phi}(\mathbf{x}, t))\bigg|_{t=\tau} = \mathbf{f}(\boldsymbol{\phi}(\mathbf{x}, \tau)), \tag{2.2}$$

for all $\mathbf{x} \in S$ and τ in some time interval I. Given some IC $\mathbf{x}_0$ such that $\boldsymbol{\phi}(\mathbf{x}_0, 0) = \mathbf{x}_0$, the flow $\boldsymbol{\phi}(\mathbf{x}_0, t)$ defines the trajectory of this IC, i.e., an orbit of the system. As the solutions of well-posed sets of differential equations are unique, orbits cannot cross each other at the same time t.

For nonlinear dynamical systems, a variety of different classes of solution structures can be obtained, allowing for the study of the system without necessarily having an analytical expression of its solution. Most of these types of solution structures are forms of invariant sets of the system. In order to explain this term, we note that for some autonomous dynamical systems described by (2.1), a set $S \subset \mathbb{R}^N$ is invariant if, for any IC in S ($\mathbf{x}_0 \in S$) the time-evolution of the orbit from this IC, $\boldsymbol{\phi}(\mathbf{x}_0, t)$, remains in S, i.e., $\boldsymbol{\phi}(\mathbf{x}_0, t) \in S$ for all $t \in I$, where I is the time interval of the existence of this solution.

The simplest class of such solutions are those corresponding to a fixed point. For a fixed point, $\mathbf{x}_f$, $\mathbf{f}(\mathbf{x}_f) = \mathbf{0}$, i.e., the trajectory of this point will remain stationary for all time. Fixed points can be further characterised by their stability, which defines how trajectories close to the fixed point behave. If all solutions $\mathbf{x}(t)$ in a small neighbourhood of the fixed point $\mathbf{x}_f$ stay close to the fixed point for all time, then the fixed point is stable. Furthermore, if $\mathbf{x}(t) \to \mathbf{x}_f$ as $t \to \infty$ then the fixed point is called asymptotically stable (see p. 3 of [10]). A fixed point which is not stable is called unstable.

The stability of the fixed points of sets of ordinary differential equations of the general form (2.1), where $\mathbf{f}$ is a nonlinear function, is determined by studying the linearised version of the system close to the fixed points (as in p. 8 of [10]). This linearisation is given by

$$\dot{\mathbf{w}} = D\mathbf{f}(\mathbf{x}) \cdot \mathbf{w}, \tag{2.3}$$

where $\mathbf{w}(t) = (\delta x_1(t), \delta x_2(t), \ldots, \delta x_N(t))$ is a deviation vector denoting small perturbations around the fixed point and $D\mathbf{f}(\mathbf{x})$ (D being a differential operator) the Jacobian of the system,

$$D\mathbf{f}(\mathbf{x}_f) = \begin{pmatrix} \frac{\partial f_1}{\partial x_1} & \cdots & \frac{\partial f_1}{\partial x_N} \\ \vdots & \ddots & \vdots \\ \frac{\partial f_N}{\partial x_1} & \cdots & \frac{\partial f_N}{\partial x_N} \end{pmatrix}\Bigg|_{\mathbf{x}=\mathbf{x}_f}. \tag{2.4}$$

The stability of this linearised system is determined by the eigenvalues of the Jacobian, λ_i. The linearisation, however, only determines the stability of the nonlinear system if the fixed point is non-degenerate, i.e., if (2.4) has no eigenvalues with zero real part (see the Hartman-Grobman theorem on p. 13 of [10]). If this is the case and all the eigenvalues of (2.4) have $\mathrm{Re}(\lambda_i) < 0$, the fixed point is stable; if they all have $\mathrm{Re}(\lambda_i) > 0$, the fixed point is unstable; if some eigenvalues have $\mathrm{Re}(\lambda_i) < 0$ and others $\mathrm{Re}(\lambda_j) > 0$, the fixed point is a saddle with corresponding stable and unstable manifolds, the directions of which are determined by the eigenvectors of the Jacobian.

The local stable $W^s(\mathbf{x}_f)$ and unstable $W^u(\mathbf{x}_f)$ manifolds are defined as

$$W^s(\mathbf{x}_f) = \{\mathbf{x} \in S : \boldsymbol{\phi}(\mathbf{x}, t) \to \mathbf{x}_f \text{ as } t \to \infty \text{ and } \boldsymbol{\phi}(\mathbf{x}, t) \in S \text{ for all } t \geq 0\},$$

$$W^u(\mathbf{x}_f) = \{\mathbf{x} \in S : \boldsymbol{\phi}(\mathbf{x}, t) \to \mathbf{x}_f \text{ as } t \to -\infty \text{ and } \boldsymbol{\phi}(\mathbf{x}, t) \in S \text{ for all } t \leq 0\},$$

where $S \subset \mathbb{R}^N$ is a neighbourhood of the fixed point. For a 2D dynamical system, the fixed points and their 1D stable and unstable manifolds can be used to divide the 2D phase space into different regions of interest, as trajectories cannot cross these manifolds.

Another class of solutions displaying both stable and unstable manifolds are periodic orbits. A periodic orbit is a solution $\boldsymbol{\gamma}(t)$ such that $\boldsymbol{\gamma}(t) = \boldsymbol{\gamma}(t + \rho)$ for all t where $\rho > 0$ is the period of the orbit. Following the discussion in Chapter 1.5 of [10], the manifolds and stability of a periodic orbit can be studied by reformulating the evolution of the orbit as a map, known as the Poincaré map. For a system of differential equations (2.1), the Poincaré map is constructed by taking the intersection of the orbits of the system with a cross-section $S \subset \mathbb{R}^{N-1}$ of dimension $N - 1$. The Poincaré map for a cross-section S, $P : S \longrightarrow S$, has the form

$$P(\mathbf{q}) = \boldsymbol{\phi}(\mathbf{q}, t_C), \tag{2.5}$$

where $\mathbf{q}$ is a point of intersection of a specific orbit with S, $\mathbf{q} \in S$, and $t_C = t_C(\mathbf{q})$ is the time taken for the orbit starting at $\mathbf{q}$ to return to the cross-section. Applying the Poincaré map iteratively will therefore show all the points of intersection of a specific trajectory with S.

A periodic orbit $\boldsymbol{\gamma}$ which initially intersects S at $\mathbf{x}_p$ and crosses S j times before returning to $\mathbf{x}_p$ is called a periodic orbit of order j. Applying the map $P^j(\mathbf{q})$ [the Poincaré map (2.5) applied j times] to $\boldsymbol{\gamma}$ will return only one point of intersection, i.e., this point $\mathbf{x}_p$ is a fixed point of the map P^j.

The stability of a fixed point of a nonlinear map with the generic form

$$\mathbf{x}_{i+1} = \mathbb{M}(\mathbf{x}_i), \quad i = 0, 1, \ldots, \tag{2.6}$$

where $\mathbb{M}$ is a nonlinear vector valued function which iteratively evolves a point $\mathbf{x}_i$ to $\mathbf{x}_{i+1}$, is found in a similar fashion to that of a continuous time dynamical

system (2.1), from the eigenvalues of the associated Jacobian matrix $D\mathbb{M}(\mathbf{x})$. Once again, the linear approximation only holds if the fixed point of the map is non-degenerate, i.e., if $D\mathbb{M}(\mathbf{x})$ has no eigenvalues of unit modulus (see p. 17 of [10]). The stability of the fixed points can further be characterised by the magnitude of the eigenvalues λ_j of $D\mathbb{M}(\mathbf{x})$. If $|\lambda_j| < 1$ for all eigenvalues then the periodic orbit is an asymptotically stable "sink"; if $|\lambda_j| < 1$ for some j values and $|\lambda_j| > 1$ for the remaining indices, the fixed point is a saddle; if $|\lambda_j| > 1$ for all j values then the fixed point is an unstable source.

The stability of a fixed point $\mathbf{x}_p$ of the Poincaré map, which corresponds to a periodic orbit γ of a continuous time dynamical system, reflects the stability of γ for the dynamical system. The periodic orbit also has stable and unstable manifolds, with the manifolds of $\mathbf{x}_p$ being the cross-section of the manifolds of γ with S. The manifolds of the orbit are therefore one dimension greater than the corresponding dimension of the Poincaré map manifolds. Periodic orbits (and their associated manifolds) are crucial in understanding the behaviour of dynamical systems, as they form the "skeleton" of the dynamics.

2.1.2 Hamiltonian mechanics

Let us now turn our attention to the specific type of systems of differential equations studied throughout this work, namely Hamiltonian systems. There exist various equivalent formulations of the equations of motion modelling the movement of particles, such as Newton's classical mechanics, Lagrangian mechanics and Hamiltonian mechanics. Newton formulated his equations of motion as

$$\ddot{\mathbf{x}} = \mathbf{F}(\mathbf{x}, \dot{\mathbf{x}}), \tag{2.7}$$

where $\mathbf{x}$ is the position of some particle in space and $\mathbf{F}$ the applied force. The kinetic energy of the system is given by $K = \frac{1}{2}m\dot{\mathbf{x}}^2$, where m is the mass of the particle. For conservative systems, where we can find some potential $U(x)$ such that $\mathbf{F}(\mathbf{x}) = -\nabla U$, the total energy of the system, $E = K + U$, remains constant.

An equivalent reformulation of Newtonian mechanics is Lagrangian mechanics. A Lagrangian system is defined by its Lagrangian function

$$\mathcal{L}(\mathbf{q}, \dot{\mathbf{q}}, t) = K(\mathbf{q}, \dot{\mathbf{q}}) - U(\mathbf{q}, t), \tag{2.8}$$

where $\mathbf{q}$ is the vector of the generalised coordinates, defined in the system's configuration space, and $\dot{\mathbf{q}} = (\dot{q}_1, \ldots, \dot{q}_N)$ the generalised velocities (see p. 7 of [12]). The Euler-Lagrange equations of motion for a Lagrangian function $\mathcal{L}$ (2.8) are shown below

$$\frac{d}{dt}\left(\frac{\partial \mathcal{L}}{\partial \dot{\mathbf{q}}}\right) - \frac{\partial \mathcal{L}}{\partial \mathbf{q}} = 0. \tag{2.9}$$

An advantage the Lagrangian formulation offers over the Newtonian formulation is that it makes finding the trajectories of particles which are constrained to some region in the configuration space far simpler. To account for these constraints, a normal force is required in the Newtonian formalism, while in the Lagrangian formalism the configuration space is restricted to the specific region. The use of generalised coordinate variables in the Euler-Lagrange equations also makes problems in different coordinate systems far simpler than the Newtonian one, which primarily utilises a Cartesian coordinate system.

A further reformulation of the Lagrangian formalism is the Hamiltonian formalism. The Hamiltonian reformulation derives the equations of motion of a system from the corresponding Hamiltonian

$$H(\mathbf{q}, \mathbf{p}, t) = \sum_{i=1}^{N} p_i \dot{q}_i - \mathcal{L}(\mathbf{q}, \dot{\mathbf{q}}, t), \quad i = 1, 2, \ldots, N, \tag{2.10}$$

where $\mathcal{L}$ is the Lagrangian of the system (2.8) and $\dot{\mathbf{q}}$ is found from the equation $\mathbf{p} = \frac{\partial \mathcal{L}}{\partial \dot{\mathbf{q}}}$ where p_i is known as the conjugate momenta of the q_i coordinate ([12] p. 8). In this formalism, the $2N$D set of coordinates $(\mathbf{q}, \mathbf{p})$ defines the phase space of the system. In general, we refer to a Hamiltonian having N degrees of freedom (dof) if the system has N generalised coordinates which are independent of each other. From the Lagrange equations we can then find Hamilton's equations of motion to be

$$\frac{d\mathbf{q}}{dt} = \frac{\partial H}{\partial \mathbf{p}} \quad , \quad \frac{d\mathbf{p}}{dt} = -\frac{\partial H}{\partial \mathbf{q}} \quad , \quad \frac{\partial H}{\partial t} = -\frac{\partial \mathcal{L}}{\partial t}, \tag{2.11}$$

which gives a system of $2N$D first-order ordinary differential equations for the positions and momenta of the system. For an autonomous Hamiltonian system, the value of the Hamiltonian is conserved as

$$\frac{dH(\mathbf{q}, \mathbf{p})}{dt} = \frac{\partial H}{\partial \mathbf{p}} \left(\frac{d\mathbf{p}}{dt} \right) + \frac{\partial H}{\partial \mathbf{q}} \left(\frac{d\mathbf{q}}{dt} \right) = \frac{\partial H}{\partial \mathbf{p}} \left(-\frac{\partial H}{\partial \mathbf{q}} \right) + \frac{\partial H}{\partial \mathbf{q}} \left(\frac{\partial H}{\partial \mathbf{p}} \right) = 0, \tag{2.12}$$

where Hamilton's equations (2.11) were used as a substitution. For such an autonomous Hamiltonian system where the kinetic energy has a quadratic form with respect to $\dot{\mathbf{q}}$, the Hamiltonian is given by $H = K + U$, i.e., the Hamiltonian is the total energy of the system (see [13] p. 66). In this thesis we study autonomous mechanical systems, so the conserved Hamiltonian quantity will simply be referred to as the energy of the system E. For an N-dof autonomous Hamiltonian system, the energy conservation restricts the $2N$D phase space to the $(2N-1)$D energy surface defined by $H(\mathbf{q}, \mathbf{p}) = E$ (we refer to regions of the phase space for which the energy conservation does not allow orbits as not energetically permissible). By fixing the system's energy to a constant value, the dimensionality of the phase

space is decreased by one and thereby the complexity of studying this model is reduced.

Another important property of Hamiltonian systems is that the flow $\boldsymbol{\phi}(\mathbf{x}, t)$, which is the operator advancing an initial solution of the system in time t, is a symplectic transformation wherever it is defined (following the proof in [14] p. 184). A map $\mathbb{M}$ is symplectic if

$$D\mathbb{M}^T J_{2N} D\mathbb{M} = J_{2N}, \tag{2.13}$$

where $D\mathbb{M}$ is the Jacobian, $D\mathbb{M}^T$ the transpose and

$$J_{2N} = \begin{pmatrix} 0_N & \mathbb{I}_N \\ -\mathbb{I}_N & 0_N \end{pmatrix}, \tag{2.14}$$

with $\mathbb{I}_N$ and 0_N being the $N \times N$ identity and zero matrices respectively. Since the flow of Hamiltonian systems is symplectic, it also preserves volume in phase space: for some open bounded set $S \subset \mathbb{R}^{2N}$,

$$\text{vol}(\boldsymbol{\phi}(S, t)) = \text{vol}(S), \tag{2.15}$$

for all time t, where $\text{vol}(S)$ is the volume of S (see [14] p. 227 and Liouville's Theorem on p. 14 of [13]). The symplectic nature of Hamiltonian systems is an important feature which allows for the construction of integration schemes which cap the error of the numerical integration at some upper limit (see Section 2.2.2).

As an example of a Hamiltonian system we consider the Hénon-Heiles system [4] given by the Hamiltonian

$$H = \frac{1}{2}(p_x^2 + p_y^2) + \frac{1}{2}(x^2 + y^2) + x^2 y - \frac{1}{3}y^3. \tag{2.16}$$

This model stems from the study of galaxies and is a prototypical, low-dimensional conservative system with rich dynamics, which has been used as a test model for a variety of different nonlinear dynamical techniques. Because of the prior use of this system in nonlinear dynamics, we utilise it to demonstrate the implementation of a variety of techniques throughout this thesis. The Hamiltonian (2.16) can be split into its kinetic $K = \frac{1}{2}(p_x^2 + p_y^2)$ and potential $U = \frac{1}{2}(x^2 + y^2) + x^2 y - \frac{1}{3}y^3$ energy parts respectively. The corresponding Hamilton's equations of motion (2.11) are

$$\begin{aligned} \dot{x} &= p_x \\ \dot{y} &= p_y \\ \dot{p_x} &= -x - 2xy \\ \dot{p_y} &= y^2 - x^2 - y, \end{aligned} \tag{2.17}$$

giving a system of nonlinear differential equations.

2.2 Numerical integrators

Since, in general, the Hamilton's equations of motion result in a system of first-order nonlinear differential equations, all but the simplest Hamiltonian systems will not be solvable using analytical methods. To approximate individual solutions of the system, given some ICs, numerical integrators are used. Such integrators are constructed by discretising the continuous differential equations of the system. More specifically, discretisation is the process of turning a continuous differential equation into a discrete difference equation, which is used to approximate the solutions of the original differential equation. The continuous time interval of the solution $[t_0, t_f]$ is split into a discrete set,

$$t_0, \quad t_1 = t_0 + h, \quad t_2 = t_0 + 2h, \ \ldots, t_f = t_0 + Rh, \tag{2.18}$$

where h is the time step size and $R + 1 = (t_f - t_0 + h)/h$ is the total number of discretised time steps used. At each instance of the discrete set of times, the solution of the system is approximated using the numerical integrator. Because this discretisation does not solve for the solutions of the differential equation exactly, there will be some errors between the computed and the exact solutions.

As the energy is conserved in autonomous Hamiltonian systems, this constant quantity is used to determine whether a numerical solution approximates the solutions accurately or not. The relative energy error is given by

$$E_r(t) = \left| \frac{E - H(\mathbf{q}(t), \mathbf{p}(t))}{E} \right|, \tag{2.19}$$

where E is the energy of the system at $t = 0$, i.e., $E = H(\mathbf{q}(0), \mathbf{p}(0))$; $\mathbf{q}(t)$ and $\mathbf{p}(t)$ are the numerically obtained values of the position and momentum using the integrator at time t; $H(\mathbf{q}(t), \mathbf{p}(t))$ is the related, computed value of the Hamiltonian function. For the computations performed in this thesis, we consider a numerical solution to be accurate if the relative error $E_r(t) < 10^{-6}$ for all t for which the solution is considered.

The errors of numerical integrators stem from two sources: rounding-off errors and discretisation errors. A rounding-off error occurs due to the computer not being able to store a number exactly. For example, the number 1/3 is not stored as a fraction, but as a decimal, which the computer truncates after a certain number of digits. In our work, double-precision accuracy is used, meaning that numbers are stored with a total of 16 significant digits. At this accuracy, the accumulation of rounding-off errors occurs at an order of 10^{-16} and are therefore not a big concern for the accuracy of the integration scheme.

Discretisation errors are usually the primary source of errors in numerical integrators. The global discretisation error at a specific point in time t_i, $i = 0, 1, 2, \ldots,$

is the difference between the exact solution and the computed approximation. This error comes from two sources: the fact that the difference equation only approximates the differential equation, and that at the point $t_{i-1} = t_i - h$, the difference equation is starting at the incorrect point due to the inaccuracy of the previous approximation to the solution. The error of the computed solution at time t_i, assuming that the solution for t_{i-1} is correct, is known as the local truncation error of the method. The local truncation error can be quantified in terms of the time step size h used in the integration method. A numerical method is said to be j-th order, $\mathcal{O}(h^j)$, if when h is decreased by an order of magnitude, the error will decrease by a factor of 10^{-j}. Since higher order methods generally require more CPU time to approximate the system with the same time step, finding the optimal balance between accuracy and CPU time for the best integrator is not always straightforward.

Two types of integrators are used in this thesis, a sixth-order Runge-Kutta scheme (RK6) [15] and the ABA864 symplectic integrator [16].

2.2.1 Runge-Kutta integration methods

The Runge-Kutta (RK) methods are very popular integrators, giving high-order truncation errors and not requiring the evaluation of any derivatives (see Chapter 5.4 of [17]). These schemes are constructed using Taylor's Theorem as outlined in [17]. The method used in our work is the RK6 scheme [15], which solves iteratively the evolution of the orbit using the following algorithm for an autonomous system of differential equations of the form (2.1),

$$
\begin{aligned}
\mathbf{k}_1 &= h\mathbf{f}\big(\mathbf{x}(t_i)\big) \\
\mathbf{k}_2 &= h\mathbf{f}\big(\mathbf{x}(t_i) + \mathbf{k}_1\big) \\
\mathbf{k}_3 &= h\mathbf{f}\big(\mathbf{x}(t_i) + [3\mathbf{k}_1 + \mathbf{k}_2]/8\big) \\
\mathbf{k}_4 &= h\mathbf{f}\big(\mathbf{x}(t_i) + [8\mathbf{k}_1 + 2\mathbf{k}_2 + 8\mathbf{k}_3]/27\big) \\
\mathbf{k}5 &= h\mathbf{f}\big(\mathbf{x}(t_i) + \big[3(3\cdot\sqrt{21} - 7)\mathbf{k}_1 - 8(7 - \sqrt{21})\mathbf{k}_2 + 48(7 - \sqrt{21})\mathbf{k}_3 \\
&\quad - 3(21 - \sqrt{21})\mathbf{k}_4\big]/392\big) \\
\mathbf{k}_6 &= h\mathbf{f}\big(\mathbf{x}(t_i) + \big[-5(231 + 51\sqrt{21})\mathbf{k}_1 - 40(7 + \sqrt{21})\mathbf{k}_2 - 320\cdot\sqrt{21}\mathbf{k}_3 \\
&\quad + 3(21 + 121\cdot 2)\mathbf{k}_4 + 392(6 + \sqrt{21})\mathbf{k}_5\big]/1960\big) \\
\mathbf{k}_7 &= h\mathbf{f}\big(\mathbf{x}(t_i) + \big[15(22 + 7\cdot\sqrt{21})\mathbf{k}_1 + 120\mathbf{k}_2 + 40(7\cdot\sqrt{21} - 5)\mathbf{k}_3 \\
&\quad - 63(3\cdot\sqrt{21} - 2)\mathbf{k}_4 - 14(49 + 9\cdot\sqrt{21})\mathbf{k}_5 + 70(7 - \sqrt{21})\mathbf{k}_6\big]/180\big) \\
\mathbf{x}(t_{i+1}) &= \mathbf{x}(t_i) + (9\mathbf{k}_1 + 64\mathbf{k}_3 + 49\mathbf{k}_5 + 49\mathbf{k}_6 + 9\mathbf{k}_7)/180.
\end{aligned}
\tag{2.20}
$$

While the step size h of the integration scheme can be adjusted to achieve a desired accuracy, the error (2.19) of the RK methods always grow linearly with integration time. This becomes problematic for longer integration times, as even a small h can result in large errors at the end of the integration.

2.2.2 Symplectic integrators

The class of integrators used for the majority of computations in this thesis are symplectic integrators (for some recent applications of these, see [16, 18, 19, 20, 21]). This is because for symplectic integrators the energy error (2.19) is capped at some upper limit, while for non-symplectic ones, the error increases linearly with time. A thorough investigation of numerical techniques and symplectic integrators can be found in [14]. In this thesis, symplectic integrators constructed using the splitting method are utilised. For a given Hamiltonian, H, the Hamilton's equations of motion can be rewritten as

$$\frac{d}{dt}\mathbf{z} = \{H, \mathbf{z}\} = L_H \mathbf{z}, \tag{2.21}$$

where $\mathbf{z} = (\mathbf{q}, \mathbf{p})^T$ is the vector of generalised coordinates and their conjugate momenta, $\{\cdot, \cdot\}$ is the Poisson bracket and $L_H = \{H, \cdot\}$ is a differential operator. We note that for any arbitrary functions of the generalised coordinates and momenta $u(\mathbf{q}, \mathbf{p})$ and $v(\mathbf{q}, \mathbf{p})$, the Poisson brackets are defined as

$$\{u, v\} = \sum_i \left(\frac{\partial u}{\partial q_i}\frac{\partial v}{\partial p_i} - \frac{\partial v}{\partial q_i}\frac{\partial u}{\partial p_i} \right). \tag{2.22}$$

The solution of the differential equation (2.21) is simply expressed as

$$\mathbf{z}(h) = e^{hL_H}\mathbf{z}(0), \tag{2.23}$$

where h is the integration time step used. If the Hamilton's equation of motion are nonlinear, equation (2.23) does not usually have an analytic expression. For a large number of Hamiltonian systems, however, the Hamiltonian can be split into its kinetic and potential energy, $H(\mathbf{z}) = K(\mathbf{p}) + U(\mathbf{q}) = H_A(\mathbf{p}) + H_B(\mathbf{q})$ where the kinetic K and potential U energies are explicitly independent of $\mathbf{q}$ and $\mathbf{p}$ respectively. As we show below, from this splitting a symplectic integration scheme can be constructed. Applying this splitting to (2.23) gives

$$\mathbf{z}(h) = e^{h(L_A+L_B)}\mathbf{z}(0). \tag{2.24}$$

Since L_A and L_B are differential operators which do not commute, the exponential cannot be written as a simple product of exponential terms. Instead, the Baker-Campbell-Hausdorff ([14] p. 86) formula has to be used so that

$$e^{hL_A}e^{hL_B} = e^{h(L_A+L_B)+\frac{h^2}{2}[L_A,L_B]+\frac{h^3}{12}([L_A,[L_A,L_B]]-[L_B,[L_A,L_B]])+\ldots}, \tag{2.25}$$

where the commutator $[L_A, L_B] = L_A L_B - L_B L_A$. From (2.25) one can obtain the following simple approximation

$$\mathbf{z}(h) = e^{h(L_A+L_B)}\mathbf{z}(0) \approx e^{hL_A}e^{hL_B}\mathbf{z}(0), \tag{2.26}$$

for (2.24). Higher order approximations of the form

$$e^{h(L_A+L_B)} = \prod_{i=1}^{p} e^{ha_i(L_A)}e^{hb_i(L_B)} + \mathcal{O}(t^{p+1}), \tag{2.27}$$

are constructed by considering higher order terms of (2.25).

The constants a_i, b_i in (2.27) can be found numerically as outlined, for example, in [22]. Using the approximation (2.27) we obtain a map from $\mathbf{z}(0)$ to $\mathbf{z}' = \mathbf{z}(h)$ as

$$\mathbf{z}' = \prod_{i=1}^{p} e^{ha_i(L_A)}e^{hb_i(L_B)}\mathbf{z}, \tag{2.28}$$

which results in the following succession of symplectic Euler maps

$$\begin{aligned} \mathbf{q}_i &= \mathbf{q}_{i-1} + ha_i \frac{\partial H_A}{\partial \mathbf{p}}(\mathbf{p}_{i-1}) \\ \mathbf{p}_i &= \mathbf{p}_{i-1} - hb_i \frac{\partial H_B}{\partial \mathbf{q}}(\mathbf{q}_i), \end{aligned} \tag{2.29}$$

for $i = 1, \ldots, p$, with $(\mathbf{q}_0, \mathbf{p}_0) = \mathbf{z}$ and $(\mathbf{q}_p, \mathbf{p}_p) = \mathbf{z}'$. The succession of maps (2.29), advances the solution of the Hamiltonian system $\mathbf{z}(0)$ by one time step h to $\mathbf{z}' = \mathbf{z}(h)$, so repeated applications of the maps describe the evolution of a solution.

The map (2.29) exactly solves a Hamiltonian system, which is an approximation of the original Hamiltonian system given by (2.27). In doing so, the map (2.29) preserves both the symplectic nature of the approximate Hamiltonian and the value of its associated energy, meaning that the energy error does not grow with respect to the integration time but remains bounded for all t.

The specific symplectic integrator used in our work is the ABA864 scheme [16]. The ABA864 method is a fourth-order symplectic integrator with the following form

$$\begin{aligned} \mathbf{z}' = &e^{a_1 hL_A}e^{b_1 hL_B}e^{a_2 hL_A}e^{b_2 hL_B}e^{a_3 hL_A}e^{b_3 hL_B}e^{a_4 hL_A}e^{b_4 hL_B} \\ &e^{a_4 hL_A}e^{b_3 hL_B}e^{a_3 hL_A}e^{b_2 hL_B}e^{a_2 hL_A}e^{b_1 hL_B}e^{a_1 hL_A}\mathbf{z}, \end{aligned} \tag{2.30}$$

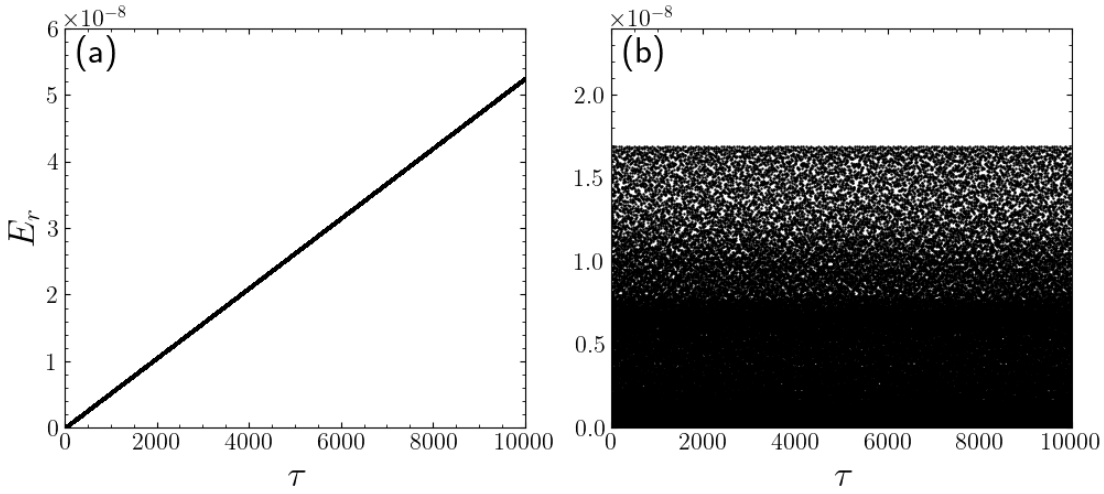

Figure 2.1: (a) The E_r (2.19) of the integrator RK6 for a trial orbit of the Hénon-Heiles system (2.16) at an energy of $H = 1/8$ with IC $x = 0$, $y = 0$ and $p_y = 0$ with $p_x > 0$ for a total integration time of 10^4 using a step size of $h = 0.05$. (b) Similar to (a) but for the symplectic integrator ABA864 with $h = 0.1$.

where the constants a_i, b_j, $i, j = 1, 2, 3$ and 4 are given in [16].

While symplectic integrators are used throughout this work for separable Hamiltonian systems, the galactic Hamiltonian discussed in Chapter 3 is not separable and the RK6 (2.20) integration scheme is used instead.

To demonstrate the difference in the evolution of E_r (2.19) between RK methods and symplectic integrators, the E_r of a test orbit of the Hénon-Heiles system (2.16) is shown with respect to the integration time τ for the integrators RK6 [Fig. 2.1(a)], and ABA864 [Fig. 2.1(b)]. The energy of the system is set to $H = 1/8$ and the IC of the test orbit is $x = 0$, $y = 0$ and $p_y = 0$ with $p_x > 0$ calculated from the Hamiltonian. Both integrators are computed for a final time of $\tau_f = 10^4$ time units, with a step size of $h = 0.05$ for RK6 and $h = 0.1$ for ABA864. For both integrators, E_r stays below 10^{-7} up until the final time, but it can be clearly seen from the results of Fig. 2.1 that E_r grows linearly for RK6, while the maximum E_r for ABA864 remains bounded below 2×10^{-8}. While the linear growth of the error for RK6 does not cause issues for short integration times, for integrations up to very long times symplectic methods are far superior.

2.3 Chaos

Alongside the different types of solutions discussed in Section 2.1.1, another important characteristic in studying nonlinear systems is their chaotic behaviour. Chaos

theory is the mathematical study of dynamical models whose evolution might seem random due to the fact that the deterministic equations governing the system's solutions are extremely sensitive to the ICs. A dynamical system is said to be extremely sensitive to its ICs, if orbits which are initially close diverge exponentially as they evolve in time. The exponential divergence of nearby orbits makes predicting the long time behaviour of an orbit impossible. While there are early examples of dynamical systems in which chaos was displayed, such as Hadamard's dynamical billiard system from 1898 [23], chaos theory only arose in the latter half of the 20th century. At that point in time, computers were becoming far more available and powerful, meaning that numerical techniques to solve dynamical systems were becoming commonplace. From these numerical solutions, it was noticed that some systems were extremely sensitive to their ICs. An early example of a numerical solution revealing the chaoticity of a model was the Lorenz system, introduced by Edward Lorenz in 1963 to study weather patterns [24]. The system is a fairly simple nonlinear model consisting of the three coupled differential equations given below,

$$\begin{aligned} \frac{dx}{dt} &= a(y-x) \\ \frac{dy}{dt} &= x(b-z)-y \\ \frac{dz}{dt} &= xy-cz, \end{aligned} \tag{2.31}$$

where a, b and c are some constants, x is the rate of convection, y the horizontal temperature variation and z the vertical temperature variation in the considered weather model. Since this system is nonlinear, Lorenz used a numerical scheme to solve it and, when doing so, he discovered that a small change in the ICs would give completely different final results. During this time period similar observations were being made for other systems as well, prompting the study of this phenomenon now known as chaos.

A wide variety of definitions have been used to try and define when a system is chaotic, one of these being the following by Devaney [25]. Let V be a set and $f : V \to V$ a map on this set. f is said to be chaotic on V if:

1. f has sensitive dependence on the ICs.

2. f is topologically transitive.

3. Unstable periodic orbits are dense in V.

The first point of this definition has already been discussed, so let us give a brief overview of the second and third points. If a map f is topologically transitive

on V, then an orbit whose evolution is determined by f will visit every non-empty subset of V at some time in the orbit's evolution. Because of the topological transitivity of chaos, we cannot divide a chaotic region into smaller, independent regions and thus often refer to the chaotic region as a chaotic sea. To address the third point, we note that unstable periodic orbits are dense in a set V if for every infinitesimally small neighbourhood in V, an unstable periodic orbit can be found. Most commonly, chaos is detected using only the first point as a criterion.

Dynamical systems are usually not entirely chaotic, as they can exhibit both chaotic and non-chaotic, namely regular, behaviours for different orbits. As discussed in Chapter 1.4 of [12], for Hamiltonian systems, as well as conservative, symplectic maps, the regular motion occurs on the surface of hyperdimensional tori, while chaotic orbits move "randomly" throughout the chaotic sea.

2.3.1 Poincaré surface of section and its computation

A standard numerical technique for visualising the phase space structure of some dynamical system is the Poincaré surface of section (PSS). A PSS of an $(N+1)$-dof autonomous Hamiltonian system is a map showing the intersections of various orbits with a $2N$D subspace of the phase space. This is the same as the Poincaré map from the discussion of periodic orbits in Section 2.1.1. While the Poincaré map was used to give an analysis of the stability and manifolds of periodic orbits, here we outline how the PSS is practically computed and how it is used to visually identify structures of interest in the phase space. The subspace of the phase space on which the PSS is plotted is usually chosen to be the cross-section where some variable, without loss of generality let us consider it to be q_{N+1}, is a constant, thereby reducing the dimensions of the system by one. The energy conservation of the Hamiltonian system then reduces another dimension, usually to determine the corresponding conjugate momenta p_{N+1} of the specific orbit. The PSS is computed on the cross-section of the other variables $q_1, \ldots, q_N, p_1, \ldots, p_N$. For some arbitrary orbit, the PSS is generated by plotting all the intersections of that orbit with the cross-section under consideration for some given time interval. Generating the PSS of a variety of orbits on the same cross-section can be used to reveal the dynamics of a system.

Since the continuous time systems are usually integrated numerically, it is not straightforward to find the intercepts of an orbit with some cross-section. A very accurate and computationally inexpensive method to find the intercepts was described by Hénon in [26] which we outline below.

Let us consider a set of $2(N+1)$ Hamilton's equations of motion

$$\begin{aligned}
\frac{dq_1}{dt} &= f_1(q_1, \ldots, q_{N+1}, p_1, \ldots, p_{N+1}) \\
&\vdots \\
\frac{dq_{N+1}}{dt} &= f_{N+1}(q_1, \ldots, q_{N+1}, p_1, \ldots, p_{N+1}) \\
\frac{dp_1}{dt} &= f_{N+2}(q_1, \ldots, q_{N+1}, p_1, \ldots, p_{N+1}) \\
&\vdots \\
\frac{dp_{N+1}}{dt} &= f_{2N+2}(q_1, \ldots, q_{N+1}, p_1, \ldots, p_{N+1}),
\end{aligned} \tag{2.32}$$

for which we want to compute the PSS for $q_{N+1} = A$, with A being a fixed real number. If for some orbit, whose evolution we evaluate using some numerical integrator with step size h, we have that at i time integration steps $q_{N+1}(ih) < A < q_{N+1}(h(i+1))$, we know that the orbit crosses the PSS in between time steps i and $i+1$. To accurately compute this intercept, we integrate the dynamical system with respect to q_{N+1} starting from time ih with a step size of $A - q_{N+1}(ih)$, as after one integration step this will give the exact intercept on the PSS. The equations which need to be integrated with respect to q_{N+1} can be found by applying the chain rule to the original system of equations (2.32), giving the following system

$$\begin{aligned}
\frac{dq_1}{dq_{N+1}} &= \frac{f_1}{f_{N+1}} \\
&\vdots \\
\frac{dq_{N+1}}{dq_{N+1}} &= 1 \\
\frac{dp_1}{dq_{N+1}} &= \frac{f_{N+2}}{f_{N+1}} \\
&\vdots \\
\frac{dp_{N+1}}{dq_{N+1}} &= \frac{f_{2N+2}}{f_{N+1}} \\
\frac{dt}{dq_{N+1}} &= \frac{1}{f_{N+1}}.
\end{aligned} \tag{2.33}$$

The implementation of this approach provides an accurate determination of the intercept and is also not computationally expensive.

As a demonstration of the ability of the PSS to reveal the phase space structure of a Hamiltonian system, we produce in Fig. 2.2 the PSS for the Hénon-Heiles system 2.16 at an energy of $H = 1/8$, setting $x = 0$ and determining $p_x > 0$ from the Hamiltonian. From this plot, both the regular and chaotic regions can be seen. The regular regions consist of the cross-section of the tori on which regular motion occurs, represented as solid curves forming deformed rings, while the chaotic region is represented as the points which look randomly scattered on the PSS.

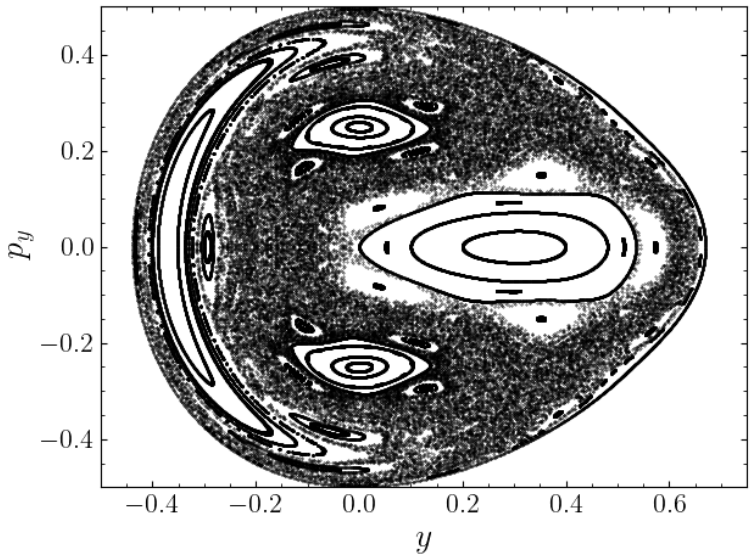

Figure 2.2: The PSS of the Hénon-Heiles Hamiltonian system (2.16) with $H = 1/8$ on the cross-section $x = 0$, $p_x > 0$.

While the PSS can be efficiently used to visualise the phase space of low-dimensional systems, its applications to a higher-dimensional setting are severely limited. For example, for a 3-dof autonomous Hamiltonian system, the energy surface is 5D, so fixing a coordinate to compute the PSS would result in a 4D PSS which cannot be easily visualised. Instead of solely relying on visualisation techniques, quantitative indicators, which can be used in both low and high-dimensional settings, have been developed to characterise orbits as either chaotic or regular. These chaos indicators are discussed in the upcoming sections and are used widely throughout this work.

2.3.2 Tangent map and variational equations

As mentioned in the beginning of Section 2.3, a key characteristic of chaoticity is the exponential divergence of initially close orbits. To measure this divergence,

the time-evolution of the deviation vector, the vector from one nearby orbit to another, is computed. A large set of chaos indicators make use of deviation vectors to characterise an orbit's chaoticity, so this subsection outlines the theory and computation of the deviations vectors.

For some ND continuous dynamical system (2.1), an infinitesimally small perturbation of $\mathbf{x}$, $\delta\mathbf{x}$, is governed by the linearised dynamics around $\mathbf{x}$. As discussed in Section 2.1.1, to study the linearised dynamics, the Jacobian of the system has to be computed, giving the time-evolution of the deviation vectors, $\mathbf{w}(t) = (\delta x_1(t), \delta x_2(t), \ldots, \delta x_N(t))$ as (see also (2.3))

$$\dot{\mathbf{w}} = D\mathbf{f}(\mathbf{x}(t)) \cdot \mathbf{w}. \tag{2.34}$$

For a N-dof Hamiltonian system, the variational equations simplify to

$$\dot{\mathbf{w}} = J_{2N} \cdot D^2 H(\mathbf{x}(t)) \cdot \mathbf{w}, \tag{2.35}$$

where $D^2H(\mathbf{x}(t))$ is the Hessian matrix of the Hamiltonian function H calculated on the reference orbit, $\mathbf{x}(t) = \boldsymbol{\phi}(\mathbf{x}(0), t)$,

$$D^2H(\mathbf{x}(t))_{i,j} = \left.\frac{\partial^2 H}{\partial x_i \partial x_j}\right|_{\mathbf{x}(t)}, \quad i,j = 1,2,\ldots,2N, \tag{2.36}$$

and J_{2N} being the matrix given in (2.14).

On the other hand, the linearised dynamics of conservative maps $\mathbb{M}$ (2.6) are governed by the corresponding tangent map. More specifically, the tangent map of $\mathbb{M}$ is calculated as

$$\mathbf{w}(i+1) = D\mathbb{M}|_i \cdot \mathbf{w}(i), \tag{2.37}$$

where $\mathbf{w}(i)$ is the deviation vector after i iterations of the map and $D\mathbb{M}|_i$ the Jacobian of $\mathbb{M}$ evaluated at iteration i.

Symplectic integrators can be used to give an accurate, numerical computation of the variational equations of continuous dynamical systems (2.35) through the so-called "Tangent map method". This method was introduced in [27] and [28], where it was shown to be more efficient and accurate for solving the variational equations than non-symplectic schemes. For a separable Hamiltonian system (see Section 2.2.2), the Hamilton's equations of motion and variational equations can be written as the following set of first-order differential equations,

$$\begin{aligned}
\dot{\mathbf{q}} &= \frac{\partial K(\mathbf{p})}{\partial \mathbf{p}} \\
\dot{\mathbf{p}} &= -\frac{\partial U(\mathbf{q})}{\partial \mathbf{q}} \\
\delta\dot{\mathbf{q}} &= D^2 K \delta\mathbf{p} \\
\delta\dot{\mathbf{p}} &= -D^2 U \delta\mathbf{q},
\end{aligned} \tag{2.38}$$

where $K(\mathbf{p})$ and $U(\mathbf{q})$ are the kinetic and potential energies of the system respectively. This set of equations (2.38) can be approximated using the splitting method discussed in Section 2.2.2 giving

$$L_A : \begin{cases} \dot{\mathbf{q}} &= \mathbf{p} \\ \dot{\mathbf{p}} &= 0 \\ \delta\dot{\mathbf{q}} &= D^2K\delta\mathbf{p} \\ \delta\dot{\mathbf{p}} &= 0 \end{cases}. \qquad L_B : \begin{cases} \dot{\mathbf{q}} &= 0 \\ \dot{\mathbf{p}} &= -\frac{\partial U(\mathbf{q})}{\partial \mathbf{q}} \\ \delta\dot{\mathbf{q}} &= 0 \\ \delta\dot{\mathbf{p}} &= -D^2U\delta\mathbf{q} \end{cases}. \tag{2.39}$$

From the corresponding operators e^{hL_A} and e^{hL_B}, symplectic integrators can be constructed in the same manner as for the usual Hamiltonian systems. For example, we consider the Hénon-Heiles system (2.16), which has the following the variational equations

$$\begin{aligned} \delta\dot{x} &= \delta p_x \\ \delta\dot{y} &= \delta p_y \\ \delta\dot{p_x} &= -(1+2y)\delta x - 2x\delta y \\ \delta\dot{p_y} &= -2x\delta x + (-1+2y)\delta y. \end{aligned} \tag{2.40}$$

Since this system can be split into its kinetic and potential energy terms, the symplectic integrators constructed in Section 2.2.2 using the splitting method can be applied to also integrate its variational equations. The two propagators for the Hénon-Heiles system with a time step size of h are shown below

$$e^{hL_A} = \begin{cases} x' &= x + p_x h \\ y' &= y + p_y h \\ p_x' &= p_x \\ p_y' &= p_y \\ \delta x' &= \delta x + \delta p_x h \\ \delta y' &= \delta y + \delta p_y h \\ \delta p_x' &= \delta p_x \\ \delta p_y' &= \delta p_y \end{cases} \qquad e^{hL_B} = \begin{cases} x' &= x \\ y' &= y \\ p_x' &= p_x - x(1+2y)h \\ p_y' &= p_y + (y^2 - x^2 - y)h \\ \delta x' &= \delta x \\ \delta y' &= \delta y \\ \delta p_x' &= \delta p_x - [(1+2y)\delta x + 2x\delta y]h \\ \delta p_y' &= \delta p_y - [2x\delta x + (1-2y)\delta y]h \end{cases} \tag{2.41}$$

2.3.3 The Lyapunov exponents

Let us now discuss the chaos indicators used in our work, starting with the most well known one, the maximal Lyapunov Characteristic Exponent (mLCE). The mLCE is the greatest of the Lyapunov exponents, which measures the average rate of growth of small perturbations of a system's orbits [29]. Oseledec's multiplicative

ergodic theorem [30] guarantees the existence of the Lyapunov exponents (given some general conditions) and provides the theoretical basis for their evaluation.

We base our discussion in this section on the work presented in [31] and [32]. An infinitesimally small spherical region of initial values in the phase space around an orbit $\mathbf{x}$, will be stretched into an ellipsoid as the orbit and initial values evolve (see p. 3 of [31]). This ND ellipsoid will have N principal axes, which are the line segments from the centre of the ellipse along the perpendicular axes of symmetry. The Lyapunov exponents are calculated using the lengths of the principal axes of the tangent space, φ_i. Below, we discuss how the length of φ_i is calculated from (2.34).

Solving (2.34) we have that $\mathbf{w}(t) = Y(t) \cdot \mathbf{w}(0)$, where $Y(t)$ is known as the fundamental matrix of solutions. This matrix satisfies the following set of ordinary differential equations

$$\frac{d}{dt}Y = D\mathbf{f}(\boldsymbol{\phi}(\mathbf{x}, t)) \cdot Y, \tag{2.42}$$

with $Y(t)$ being a square matrix, such that $Y(0) = \mathbb{I}_N$ and $D\mathbf{f}(\boldsymbol{\phi}(\mathbf{x}, t))$ the Jacobian of the system at the location of the flow $\boldsymbol{\phi}(\mathbf{x}, t)$ at time t. To analyse this, a singular value decomposition (SVD) technique is applied to $D\boldsymbol{\phi}(\mathbf{x}, t)$ (as discussed in [31] p. 3 and p. 4). This decomposition gives

$$D\boldsymbol{\phi}(\mathbf{x}, t) = R \cdot Q \cdot V^T, \tag{2.43}$$

where Q is an $N \times N$ diagonal matrix containing the singular values $\varphi_1 \geq \varphi_2 \geq \cdots \geq \varphi_N \geq 0$ and R and V are $N \times N$ orthogonal matrices ($RR^T = R^T R = \mathbb{I}_N = VV^T = V^T V$, with R^T and V^T being the transpose of R and V respectively). Since $V^T = V^{-1}$ (due to V being orthogonal),

$$D\boldsymbol{\phi}(\mathbf{x}, t)V = R \cdot Q, \tag{2.44}$$

i.e.,

$$D\boldsymbol{\phi}(\mathbf{x}, t)\mathbf{v}^{(i)} = \varphi_i \mathbf{r}^{(i)}, \quad i = 1, \ldots, N, \tag{2.45}$$

where $\mathbf{v}^{(i)}$ and $\mathbf{r}^{(i)}$ are the i-th column vectors of V and R respectively. The singular values therefore give the lengths of the principal semi-axes of the evolved region around an orbit. The Lyapunov exponents are then given as

$$\Lambda_i = \lim_{t \to \infty} \frac{1}{t} \ln \varphi_i(t), \tag{2.46}$$

which are the mean logarithmic growth rates of the lengths of the principal axes. The set of all Lyapunov exponents of a dynamical system is known as the Lyapunov spectrum. For chaotic orbits, small perturbations grow exponentially fast, so the mLCE Λ_1 will have a positive value as this corresponds to the greatest mean

logarithmic growth rate of the perturbations. On the other hand, for regular orbits of symplectic systems the mLCE will be zero, as perturbations do not diverge exponentially. This allows one to determine whether an orbit is chaotic or regular based on the value of the mLCE. For $2N$D symplectic systems, the spectrum of Lyapunov exponents has the property that (see p. 90 of [32])

$$\Lambda_i = \Lambda_{2N-i+1}, \quad i = 1, 2, \ldots, N. \tag{2.47}$$

Furthermore, for Hamiltonian models

$$\Lambda_N = \Lambda_{N+1} = 0. \tag{2.48}$$

The mLCE can be calculated for a general orbit with IC $\mathbf{x}(0)$ using some initial deviation vector $\mathbf{w}(0)$. Given that $\mathbf{w}(0)$ does not point in the direction of one of the principal axes, $\mathbf{w}(t)$ will start aligning with the vector in which small perturbations of the orbit are growing at the greatest rate. This vector $\mathbf{w}^{max}$ corresponds to the largest singular value φ_1. Dividing by the initial magnitude of $\mathbf{w}(0)$ will therefore give that

$$\lim_{t\to\infty} \frac{\|\mathbf{w}(t)\|}{\|\mathbf{w}(0)\|} = \varphi_1. \tag{2.49}$$

From this the mLCE can then be calculated as

$$\Lambda_1 = \lim_{t\to\infty} \frac{1}{t} \ln \frac{\|\mathbf{w}(t)\|}{\|\mathbf{w}(0)\|}. \tag{2.50}$$

It was demonstrated in [33, 34] that when computing the mLCE with the initial deviation vector chosen in the direction of one of the other Lyapunov exponents, the deviation vectors will still align with the direction of the mLCE due to the accumulation of computational errors.

The mLCE has been used to efficiently study chaos in a variety of models, such as the motion of planetary satellites [35], disordered granular chains [36, 37], DNA molecules [38], graphene nanoribbons [39], neural networks [40], black holes [41] and soft architected structures [42]. However, due to the long CPU times required to calculate the long time limit estimation of the mLCE (2.50), a variety of faster chaos indicators have been developed. These include the Fast Lyapunov Indicator [43] and its variants [44], the Mean Exponential Growth Factor of Nearby Orbits [45], as well as the SALI [7] and Generalised Alignment Index [46]. An overview of these numerous methods can be found in [47].

2.3.4 The Smaller Alignment Index

Alongside the mLCE, the SALI will be used as a chaos indicator in our work. Let us recall from Section 2.3 that for autonomous Hamiltonian systems, as well as

symplectic maps, regular motion occurs on the surface of a torus in the phase space. As discussed in Section 5.3 of [32], the deviation vectors of a regular trajectory will fall on the surface of the tangent space of this torus, with their magnitude growing approximately linearly. For chaotic trajectories on the other hand, the deviation vectors will be stretched in the direction of the mLCE, aligning with the direction of the mLCE eventually. The SALI, first introduced in [7], makes use of the alignment of the deviation vectors of an orbit in the direction of the greatest growth in perturbations to identify chaos. For two randomly generated initial deviation unit vectors, $\hat{\mathbf{w}}_1(0)$ and $\hat{\mathbf{w}}_2(0)$ [$(\hat{})$ denotes a unit vector], where $\hat{\mathbf{w}}_1(t)$ and $\hat{\mathbf{w}}_2(t)$ are the deviation vectors at time $t > 0$, the SALI is given by

$$\text{SALI}(t) = \min\{||\hat{\mathbf{w}}_1(t) + \hat{\mathbf{w}}_2(t)||, ||\hat{\mathbf{w}}_1(t) - \hat{\mathbf{w}}_2(t)||\}. \tag{2.51}$$

The minimum of the sum and difference of the deviation vectors is considered in (2.51), as for chaotic orbits both deviation vectors will be stretched in the direction of φ_1, aligning to have either the same or opposite directions. For regular trajectories the deviation vectors will lie on the tangent space of the torus, but for systems of a dimension $N > 2$ the deviation vectors will not coincide, so the SALI will saturate to some positive constant. The SALI of a chaotic orbit, on the other hand, will approach zero at an exponential rate due to the deviation vectors aligning, letting one distinguish between regular and chaotic motion. To summarise the behaviour of the SALI for systems of $N > 2$:

$$\text{SALI}(t) \propto \begin{cases} \text{constant} & \text{for regular orbits} \\ e^{-(\Lambda_1 - \Lambda_2)t} & \text{for chaotic orbits} \end{cases}, \tag{2.52}$$

where Λ_1 and Λ_2 are the first and second largest Lyapunov exponents respectively (see [48] and p. 136 of [49]).

For 2D maps, the regular torus is a 1D curve, so any deviation vectors on it will be in the same or opposite directions. It was, however, demonstrated in [50] that the rate of the alignment is exponentially fast for chaotic trajectories and polynomially fast for regular ones, thus,

$$\text{SALI}(t) \propto \begin{cases} \frac{1}{t^2} & \text{for regular orbits} \\ e^{-2\Lambda_1 t} & \text{for chaotic orbits} \end{cases}, \tag{2.53}$$

letting one distinguish between the two types of orbits.

While the integration of two deviation vectors is required to compute the SALI and only one deviation vector for the mLCE, since the SALI approaches zero (to numerical accuracy) exponentially fast for chaotic orbits the computation can be stopped when the SALI has reached this threshold and successfully identified the orbit as chaotic. This results in the SALI being, in general, faster than the mLCE

in determining whether a set of ICs are regular or chaotic. The SALI has been used successfully in studying accelerator models [51, 52], problems in nuclear physics [53], predator-prey populations [54], galactic potentials [55, 56], and Bose-Einstein condensates [57].

2.3.5 The numerical computation of the mLCE and SALI

By numerically solving the Hamilton's equations of motion and the variational equations, the mLCE can be computed as the long time limit of

$$X_1(t) = \frac{1}{t} \ln \frac{\|\mathbf{w}(t)\|}{\|\mathbf{w}(0)\|}, \tag{2.54}$$

i.e., $\Lambda_1 = \lim_{t\to\infty} X_1(t)$. We refer to the quantity X_1 as the finite time maximal Lyapunov exponent (ftmLE). Because regular orbits diverge at most polynomially and chaotic orbits exponentially, the behaviour of $X_1(t)$ is (see Section 5.3 of [32])

$$X_1(t) \propto \begin{cases} \ln(t)/t & \text{for regular orbits} \\ \text{constant} & \text{for chaotic orbits} \end{cases}. \tag{2.55}$$

Due to the exponential growth rate of $\|\mathbf{w}(t)\|$ for chaotic orbits, this implementation (2.54) fails numerically when $\|\mathbf{w}(t)\|$ grows too large for the computer to store. This issue was however circumvented in [33, 34], where the standard method for the computation of the mLCE estimator is described. Instead of computing (2.54), every kh time units (where k is an integer and h the time step used) the deviation vector is normalised to $\hat{\mathbf{v}}(kh)$ and its magnitude $\alpha_i = \|\mathbf{w}(kh)\|$ recorded. Then the ftmLE $X_1(kh)$ can be computed as

$$X_1(kh) = \frac{1}{kh} \sum_{i=1}^{k} \ln \alpha_i. \tag{2.56}$$

For the next iteration $\hat{\mathbf{w}}(kh)$, i.e., a unit vector, is used as the initial deviation vector, thereby preventing computational blow-ups (for a more detailed description see Section 5 of [32]). The SALI is computed in a similar fashion with the two tangent vectors being normalised at every k time steps with the SALI then being computed as (2.51).

To demonstrate the behaviour of the ftmLE, X_1, and SALI for $(N > 2)$D dynamical systems, we consider a regular and chaotic orbit of the Hénon-Heiles system (2.16). In Fig. 2.3(a) the PSS of the system at $H = 1/8$ on the cross-section $x = 0$, $p_x > 0$ is shown. The PSS of a regular orbit, with IC $x = 0$, $y = 0.2$ and $p_y = 0$, and a chaotic orbit, with IC $x = 0$, $y = -0.15$ and $p_y = 0$, are shown as

light-blue and red points in Fig. 2.3(a) respectively. The evolution of X_1 (2.54) with respect to the integration time τ of the two orbits is shown in Fig. 2.3(b). The dashed light-blue line in Fig. 2.3(b) corresponds to a slope of $\ln(\tau)/\tau$, which is identical to the slope of X_1 of the regular orbit at later times. The values of X_1 of the chaotic orbit can be seen to saturate to a constant value, as we would expect from (2.55). In Fig. 2.3(c) the SALI of the regular and chaotic orbit is shown, with the dashed black line corresponding to a slope of $e^{-\Lambda_1 \tau}$ (since $\Lambda_2 = 0$ for 2-dof Hamiltonian models). As expected from (2.52), the SALI of the regular orbit remains at some positive constant, while that of the chaotic orbit decreases exponentially fast, with a similar evolution to the dashed black line.

Double computer precision is used in all computations, so values at an order of magnitude 10^{-16} correspond numerically to 0 (since only 16 significant digits are used in the calculations). This means we can stop computing the SALI for an orbit once it reaches 10^{-16} and can identify this orbit as chaotic. The SALI of the chaotic orbit in Fig. 2.3 reaches this threshold at approximately $\tau = 1,000$.

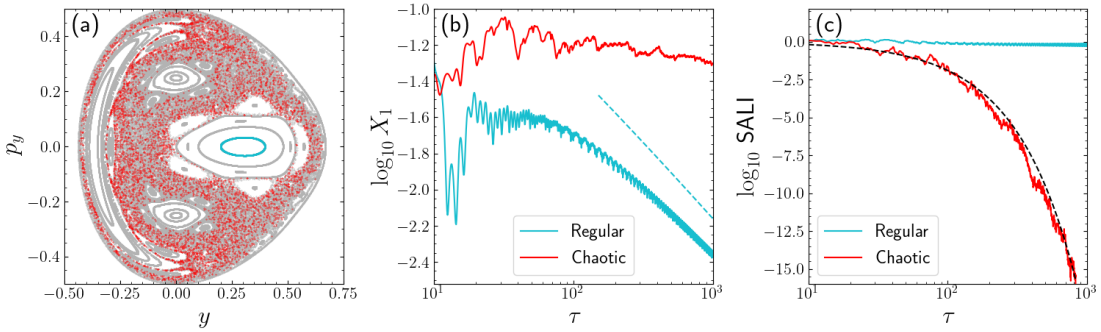

Figure 2.3: (a) The PSS of the Hénon-Heiles system (2.16) at an energy of $H = 1/8$ on the cross-section $x = 0$, $p_x > 0$. Light-blue and red points correspond to the PSS of a regular orbit with IC $x = 0$, $y = 0.2$ and $p_y = 0$ and of a chaotic orbit with IC $x = 0$, $y = -0.15$ and $p_y = 0$ respectively, while the intersections of several other orbits are plotted by grey points. (b) The time evolution of the mLCE estimator X_1 (2.54) for the regular and chaotic orbit considered in (a), for a total integration time of $\tau = 1,000$. The dashed blue line corresponds to a function proportional to $\ln(\tau)/\tau$. (c) Similar to (b), but for the SALI of the two orbits considered in (a). The dashed black line corresponds to a function proportional to $e^{-\Lambda_1 \tau}$.

As stated in Section 2.3.4, the SALI of a regular orbit for a 2D map will tend to zero at a linear rate, while for chaotic orbits it will decrease at an exponential rate (2.53). As a demonstration of the SALI's behaviour for such systems, we consider the 2D standard map [5], as a test case of a 2D iterative, symplectic map having

the form

$$\begin{aligned} x_1' &= x_1 + x_2' \\ x_2' &= x_2 + \frac{K}{2\pi}\sin(2\pi x_1) \end{aligned} \quad (\text{mod } 1), \tag{2.57}$$

with K being a real parameter and x_i' denoting the next iteration of x_i, $i = 1, 2$. Since both coordinates are modulo 1, we have $x_1, x_2 \in [0, 1)$ with the phase space forming the surface of a 2-torus. This system is a prototypical model of a low-dimensional, conservative map, which will be used throughout our work to demonstrate a variety of numerical techniques. In Fig. 2.4(a) the evolution of a regular (light-blue) and chaotic (red) orbit are shown for $K = 1.5$. The ICs of the regular and chaotic orbits are $(x_1, x_2) = (0.6, 0.2)$ and $(x_1, x_2) = (0.2, 0.1)$ respectively. The regular orbit forms a ring, which appears discontinuous due to the modulo, while the chaotic orbit creates points which look randomly distributed. In Fig. 2.4(b) the ftmLEs, X_1, of both orbits are shown for $T = 1,000$ total iterations, with the dashed light-blue line indicating a function proportional to $\ln(T)/T$. As expected, the ftmLE of the regular orbit decreases following the law $\ln(T)/T$, while that of the chaotic orbit saturates to some positive constant. In Fig. 2.4(c) the time evolution of the SALI is shown for both orbits. The dashed light-blue and black lines in 2.4(c) correspond to functions proportional to $1/T^2$ and $e^{-2\Lambda_1 T}$ respectively. The SALI of the chaotic orbit is seen to decrease exponentially, as in the case of the Hénon-Heiles system [Fig. 2.3 (b)], but the SALI of the regular orbit also shows a decrease with a slope -2 in the log-log scale of Fig. 2.4(c). When using the SALI to differentiate between regular and chaotic orbits of a 2D map, caution must be exercised, as the long-term limits of the SALI of the regular and chaotic orbits are both zero.

The different behaviours of the ftmLE and SALI for regular and chaotic orbits allow us to identify the chaoticity of both individual and large ensembles of orbits. Colouring each IC of a set of orbits according to its ftmLE and/or SALI value after some final integration time (or number of iterations in the case of maps), produces plots from which the distinct regions of regular and chaotic motion can be seen. When creating colour plots using the SALI, the two initial deviation vectors for each IC should be randomly generated. Otherwise, the SALI plot will have some artificial "structures" as discussed in pp. 161-164 of [49].

2.4 The method of Lagrangian descriptors

Recently, a new method to study the phase space of dynamical systems has been developed: the method of LDs. This method is straightforward to implement, it relies on simple numerical computations along the trajectories of various ICs, and provides high resolution, lower-dimensional slices which can be used to study

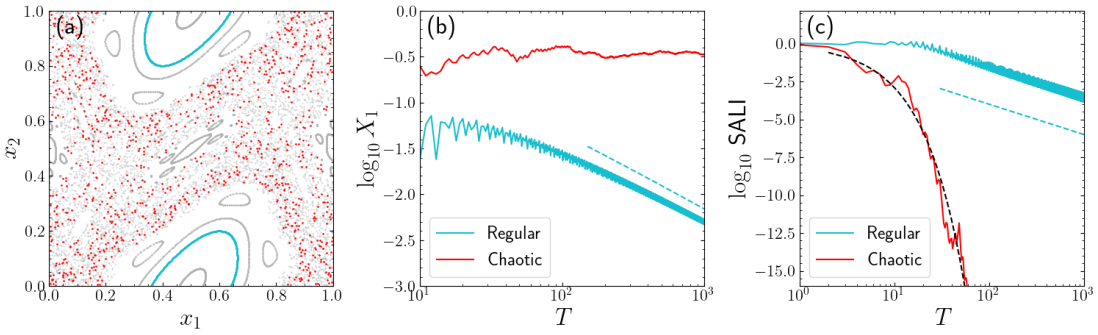

Figure 2.4: (a) The evolution of a regular orbit (light-blue) with IC $(x_1, x_2) = (0.6, 0.2)$ and a chaotic orbit (red) with IC $(x_1, x_2) = (0.2, 0.1)$ of the 2D standard map (2.57) with $K = 1.5$ for $T = 1,000$ iterations. The consequents of various other ICs are shown in grey, to reveal the structure of the system. (b) The time evolution of the ftmLE, X_1, for the regular and chaotic orbits considered in (a). At later times, the evolution of the mLCE of the regular orbit matches that of the dashed blue line with the functional form $\ln(T)/T$. (c) The time evolution of the SALI for the regular and chaotic orbits considered in (a). The dashed blue and black lines correspond to functions proportional to $1/T^2$ and $e^{-2\Lambda_1 T}$ respectively.

the dynamics of high-dimensional systems. Introduced in [1] this method was referred to as the M function until in [58] the use of the M function as an LD was first described. While LDs were initially developed to study ocean flows, since its inception this technique has seen use in a wide variety of fields: transition state theory [59, 60, 61], dissipative systems [62, 63], stochastic systems [64], ozone hole formation [65], the study of dividing surfaces [66], 3D vector fields [67], molecular systems [68, 69], open and unbounded maps [70, 71], cardiovascular flows [72], and the study of bifurcations of periodic orbits [73].

For deterministic dynamical systems, the ICs determine all aspects of the evolution of the orbits in the phase space. The method of LDs makes use of this fact by assigning to each IC in some grid in the phase space a positive number, calculated by accumulating values of some chosen positive quantity along the trajectory when it is propagated both forward and backward in time. The most intuitive choice of this positive quantity is the arclength of the trajectory (referred to as the arclength LDs). If we have some dynamical system, described by a set of first-order differential equations as in (2.1), and some IC $\mathbf{x}_0 = \mathbf{x}(t_0)$ at time t_0, the forward time arclength LD, of the trajectory is

$$M^f(\mathbf{x}_0, t_0, \tau) = \int_{t_0}^{t_0+\tau} \|\dot{\mathbf{x}}\| dt, \tag{2.58}$$

where τ is some fixed integration time for which we follow the trajectory, and $\|\cdot\|$

is the Euclidean norm. Similarly, the backward time arclength LD is

$$M^b\left(\mathbf{x}_0, t_0, \tau\right) = \int_{t_0-\tau}^{t_0} \|\dot{\mathbf{x}}\| dt. \tag{2.59}$$

The arclength LDs characterise the phase space of the system by how far the orbits move through the phase space. Although simple, this method reveals a wide variety of information about a dynamical system's solution structure. At any fixed points of the system, the LD will be zero, as the solutions are stationary. Orbits which do not start at a fixed point will not remain stationary, and therefore will have positive LD values. Thus, from the scalar LD field on some grid of ICs, the fixed points will be easily recognisable as the minima of the field (see for example Figs. 24, 26 and 36 of [74]).

Similarly, LDs also detect the stable and unstable manifolds around a saddle fixed point. In order to explain in more detail the behaviour of LDs for manifolds, let us consider an orbit starting on the stable manifold and calculate its arclength in forward time. Since orbits on the stable manifold approach the fixed point, they have a finite distance they can travel, i.e., their LD values are bounded from above. On the other hand, any other nearby solutions not on the stable manifold will continue moving throughout the phase space, thereby increasing their LD values. If an appropriate integration time is chosen so that trajectories not on manifolds move further through the phase space than the distance of the points on the manifolds to the fixed point, the stable manifold will be at a trough of the LD scalar field leading to the fixed point. Integrating in backward time will reveal the unstable manifolds in a similar fashion, so from the combined forward (2.58) and backward (2.59) time integrals, both the stable and unstable manifolds can be identified (with the saddle fixed point at their intersection).

To demonstrate the ability of LDs to detect manifolds, we consider the 1-dof linear saddle system [74], whose Hamiltonian is

$$H(q,p) = \frac{1}{2}(p^2 - q^2). \tag{2.60}$$

From the system's corresponding Hamilton's equations of motion,

$$\begin{aligned} \dot{q} &= p \\ \dot{p} &= q, \end{aligned} \tag{2.61}$$

a fixed point can be identified at the origin. Solving this simple system of differential equations, we find that the origin is a saddle fixed point, with the corresponding stable and unstable manifold's functional form being $p = \pm q$. The colour plots of the forward, backward, and combined LDs [using the arclength definition (2.58) and (2.59)] with a total integration time of $\tau = 10$ are shown in Fig. 2.5 for a grid

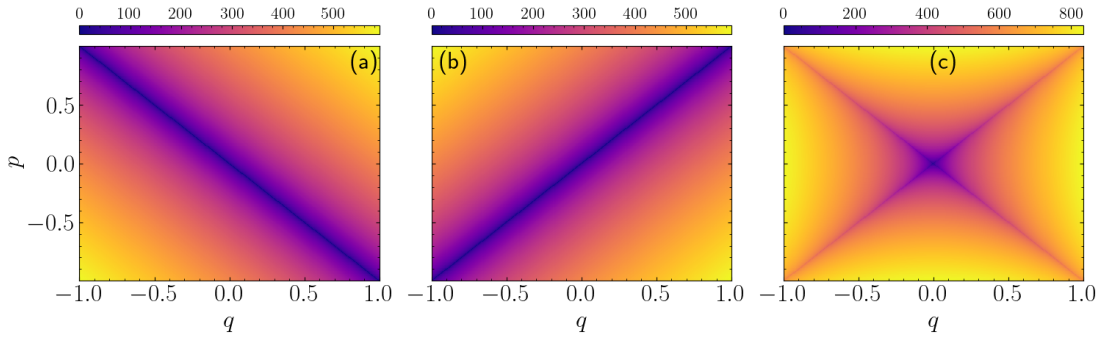

Figure 2.5: (a) The forward LDs of the 1-dof linear saddle system, (2.60), calculated using the arclength definition (2.58) on a grid of 401×401 evenly spaced ICs on the intervals $q, p \in [-1, 1]$ for a total forward integration time of $\tau = 10$. (b) The backward LDs computed on the same grid of ICs as (a) for a total backward integration time of $\tau = 10$. (c) The total LDs (combined forward and backward LDs) for the grid of ICs considered in (a). In each panel, the ICs are coloured according to their LD values using the colour scale on top of each panel.

of 401×401 ICs on the intervals $q, p \in [-1, 1]$. The ICs are coloured according to their LD values using the colour scale seen at the top of each panel. The manifolds and the fixed point can already be clearly seen from these plots at the places where the LDs have minimum values. For generic dynamical systems it was demonstrated in [75] and [76] that the invariant manifolds are represented as singular features in the LD scalar field, i.e., the gradient of the LDs at the manifolds is discontinuous. Numerically, this discontinuity is represented as a high LD gradient at the location of the manifold. For a 2D grid of ICs, we calculate the magnitude of the gradient of the LD field as

$$M_{grad} = \sqrt{M_x^2 + M_y^2}, \tag{2.62}$$

where M_x and M_y are the gradients of the LDs in the x and y directions, calculated using a finite difference scheme, respectively. Plotting the gradient of the LDs in Fig. 2.6, we see the manifolds as the regions where the gradient is at a maximum.

The arclength serves as a good introduction to LDs as it gives an easy-to-understand explanation of why this method works. A wide variety of definitions of LDs have been introduced since their inception, using different quantities that are accumulated along the trajectory. In [77] it is described how to construct LDs in general, suggesting that using any function that encodes some intrinsic property of the phase space, not only the velocity, will reveal the properties of the phase space. For example, the acceleration, time-derivative of the acceleration or even the curvature, could be accumulated along an orbit's evolution to compute the LDs. Since all of these functions are time-dependent, they will display the

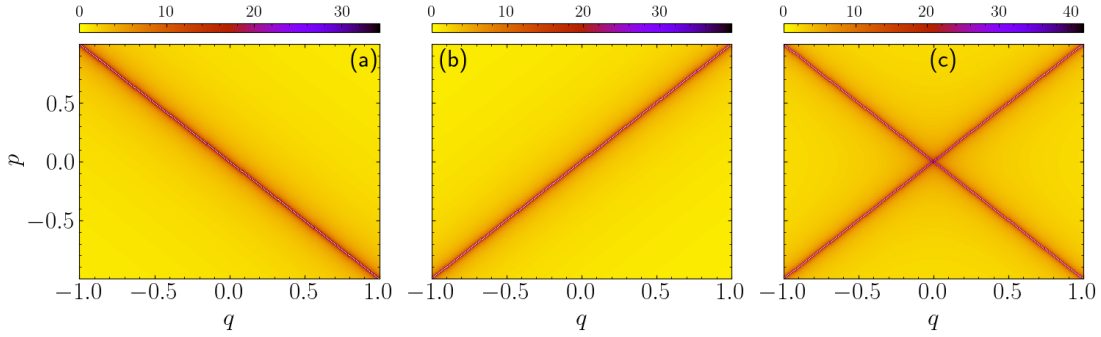

Figure 2.6: (a)-(c) The gradient of the results presented in Figs. 2.5(a)-(c) respectively.

boundary of regions with different time evolutions as an abrupt change in the LDs plot. Not only can we change the function which we accumulate along the trajectory, but also how we take the magnitude of this function. So far only the Euclidean norm has been used, but a variety of different norm-like quantities have been used in the literature to better indicate the geometry of the phase space.

The most popular of these "norms" is the so-called "p-norm", introduced in [76] as

$$M_p(\mathbf{x}_0) = \int_{-\tau}^{\tau} \sum_{k=1}^{N} |\mathcal{F}_k(\mathbf{x}(t), t)|^p dt \quad , \quad p \in (0, 1], \tag{2.63}$$

where $\mathcal{F}_k$ is the k-th component of the arbitrary vector quantity $\mathcal{F}$ which is accumulated along an orbit's path. It should be noted that for $p < 1$, the "p-norm" is not actually a norm, hence the quotation marks in its name. Usually p is taken to be $\frac{1}{2}$, as this gives the most noticeable discontinuity in the LD gradient at the manifolds (see, for example, the results in [71, 78, 79]).

The LDs can be also be calculated for ND iterative maps (2.6) with the "p-norm" LD, given by

$$M_p(\mathbf{x}_0) = \sum_{j=-T}^{T-1} \sum_{i=1}^{N} \left| x_{j+1}^{(i)} - x_j^{(i)} \right|^p, \quad p \in (0, 1], \tag{2.64}$$

where $2T$ is the total number of iterations of the map, the subscript j denotes the j-th iteration, and the superscript i indexes the N elements of the state vector $\mathbf{x}$.

The integration time/number of iterations, τ/T (for continuous time systems and maps respectively) plays a key role in the calculation of the LDs of a system. It needs to be long enough so that the LDs can display the different behaviours and structures of the phase space, but also short enough so that not too much CPU time is required for the calculation. Sadly, there is no rule of thumb to determine

how to choose τ/T for different models and instead a method of trial and error has to be used to determine what τ/T is best suited for every specific problem.

So far, we have considered what are known as fixed time LDs because they are computed for a fixed value of time τ or iterations T (2.58). This approach works efficiently for systems where orbits do not escape to infinity and, for example, are trapped in a potential well. However, it can result in issues for open systems, where the motion is not confined to some phase space region. In open systems, some trajectories may escape to infinity in finite time, causing the LDs to blow up if we accumulate the trajectories for long enough. This will hide certain regions of the phase space, as the range of LD values is so large (with the LDs of escaping trajectories far bigger than those of trapped orbits) that the LDs in the trapped regions will be indistinguishable. Integrating for shorter periods of time often does not fix this problem, as it does not allow for the trajectories to evolve long enough to display the intricacies of the phase space. A way to tackle this problem is to compute LDs at variable times, as discussed in [80]. According to that approach, instead of only integrating for some fixed time, the trajectories are accumulated for either some fixed time τ/T or until they leave some predefined region of the phase space at time $\tau^{\pm}/T^{\pm}$ (the superscript $+$ denotes the forward and $-$ the backward integrations), whichever one is shorter. This restricts the calculation of the LDs of trajectories which escape to infinity to some reasonable finite value, as the evolution of these trajectories is stopped once they have left a predefined region of the phase space, and also allows for non-escaping trajectories to evolve for long enough time to display the underlying dynamical structure.

A relatively simple system, which we use to demonstrate this approach, is a model having a cubic potential corresponding to the Hamiltonian function [81]

$$H = \frac{1}{2}p^2 - \mu q + \frac{1}{3}q^3. \tag{2.65}$$

For $\mu > 0$, this system consists of a saddle fixed point at $(q_0, p_0) = (-\sqrt{\mu}, 0)$ and a centre at $(q_0, p_0) = (\sqrt{\mu}, 0)$. However, when plotting the fixed time LDs (on a grid of 401×401 evenly spaced ICs on the intervals $q \in [-1.5, 1.75]$ and $p \in [-1.25, 1.25]$ with $\mu = 0.25$ for a total integration time of $\tau = 8$) in Fig. 2.7(a), we see that certain parts of the phase space are obscured by the blown up LD values for which the orbits have escaped to infinity (the white regions in the plot). In Fig. 2.7(b) we show variable time LDs, with the restriction that trajectories stay in the region defined by the circle of radius 15 centred at the origin of the plane (q, p), on the same grid of ICs and integration time. From this figure, both the saddle fixed point and centre can be clearly seen, with the manifolds forming a fish-like shape. This figure reproduces some results reported in [81]. We note that for an arbitrary dynamical system with escapes, choosing an appropriate phase space region for variable integration time LDs is not always straightforward and

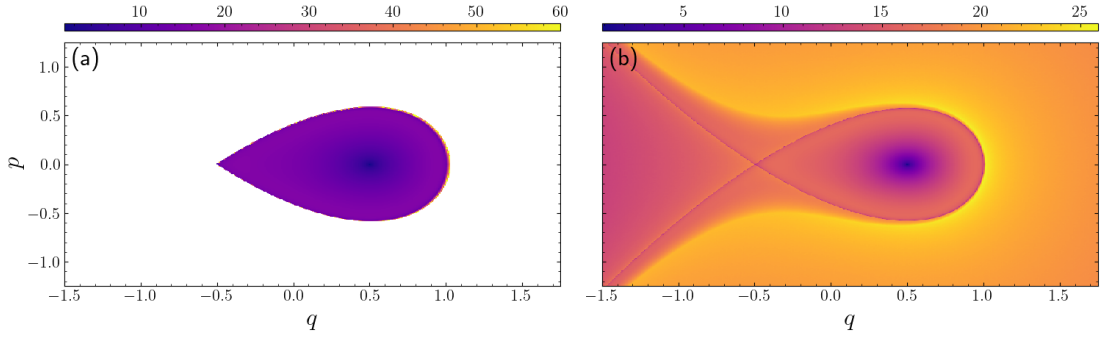

Figure 2.7: (a) Fixed time LDs on a grid of 401×401 evenly spaced ICs for the cubic potential (2.65), for a total integration time of $\tau = 8$ both forward and backward in time. The white regions in (a) correspond to ICs where the LDs have blown up due to the escapes. (b) The variable integration time LDs for the same set of ICs as (a), for $\tau = 8$, with the trajectories restricted to a circle of radius 15 centred at the origin (if a trajectory leaves the circle for $\tau < 8$, the corresponding IC is coloured according to the LD value at the time of crossing). Both panels are coloured according to the colour scale seen at the top of each panel.

requires some investigation to find.

Let us now discuss what advantages LDs offer over the standard technique for visualising phase space structures, the PSS (Section 2.3.1). The first problem with constructing the PSS is that we need the trajectories of our ICs to return to our phase space slice, something which is not guaranteed. This requirement places a restriction on what trajectories we may want to consider for our PSS, a problem we do not have with the method of LDs, as it is unimportant where the trajectories of our ICs travel in the phase space, only what LD values they obtain from their time evolution.

The next advantage that LDs offer over the PSS is that one immediately knows what resolution of grid is being calculated for the LD plot, as the LD scalar field has the same resolution as the grid of ICs we selected to calculate the LDs on. However, for the PSS, we do not know how many points we will end up with, as we have no indication of how many ICs and how much integration time is required to find enough intersections for the PSS to reveal the phase space structure.

It should also be mentioned that LDs can be calculated for autonomous and non-autonomous Hamiltonian systems in the exact same manner. This is not the case for the PSS, which can only be calculated for non-autonomous systems if the time-dependence is periodic [74].

Not only do LDs offer technical advantages over the PSS, but they also produce additional information about the phase space, revealing the manifolds in regions of both regular and chaotic motion. The PSS, on the other hand, simply repre-

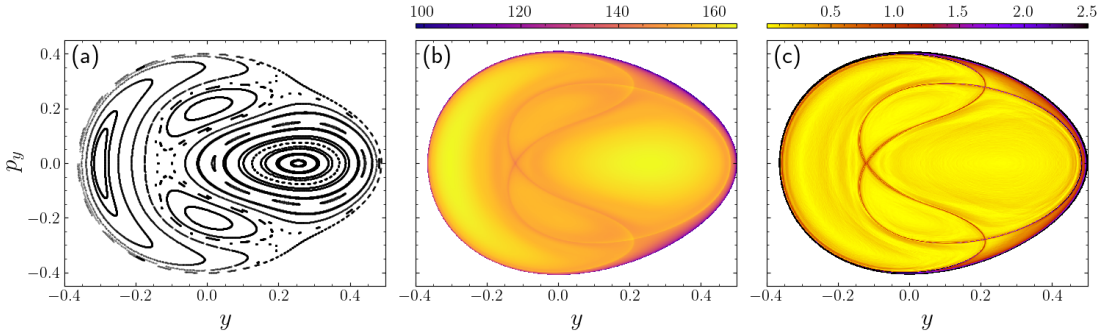

Figure 2.8: (a) PSS of the Hénon-Heiles system, (2.16), at $H = 1/12$, with $x = 0$ and $p_x > 0$. (b) The combined forward and backward LDs on a grid of $1,001 \times 1,001$ evenly spaced ICs on the intervals $y \in [-0.4, 0.5]$, $p_y \in [-0.4, 0.4]$ for a total integration time of $\tau = 50$. (c) The corresponding LD gradient of (b). Panels (b) and (c) are coloured according to the colour scales at the top of the panels.

sents chaos as a collection of random-looking points from which we can gather no information other than that a region is indeed chaotic, and represents the regular regions as consisting of deformed rings which do not indicate the presence of manifolds. The LDs, however, will reveal the manifolds as a steep change in the LD gradient in both regular and chaotic regions, letting us study the complexity of the phase space (see for example [82]).

As a comparison between the PSS and LDs plots, let us consider their application to the Hénon-Heiles system (2.16). Letting $H = 1/12$ the PSS on the y, p_y slice for $x = 0$ and $p_x > 0$ is shown in Fig. 2.8(a). At this energy, no chaotic orbits can be seen, which would be characterised on the PSS by a region of points which appear randomly distributed. Instead, only the cross-section of the invariant tori on which regular motion occurs can be seen. While this plot does show some of the structure of the phase space, the manifolds of unstable periodic orbits cannot be identified from it.

To reveal these manifolds, the LD and LD gradient plots for a grid of $1,001 \times 1,001$ evenly spaced ICs on the same cross-section for a final integration time of $\tau = 50$ is shown in Figs. 2.8(b) and (c) respectively. From the LD gradient in Fig. 2.8(c), the manifolds can be seen as the darker curves. These manifolds do not originate from the fixed points of the system, like in the case of the 1-dof systems, but instead correspond to the manifolds of some unstable periodic orbits located at the intersections of the stable and unstable manifolds.

So far, we have only considered a 2-dof Hamiltonian, but the drawbacks of the PSS become even more pronounced when considering systems with higher dimensions. If, for example, we consider a 3-dof autonomous Hamiltonian model, we will be working on a 5D energy surface which we can restrict to a 4D PSS

by letting some phase space coordinate value be constant. Analysis of this high-dimensional PSS requires a combination of a 3D plot and a colour scale for the fourth coordinate, as was done for example in [83], or to use the method of 3D phase space slices [84]. For the LDs, we can create 2D subspaces of the whole phase space simply by choosing a slice with a certain resolution and calculating the LDs on that, as was done for example in [85].

2.5 Code optimisation and parallelisation

For plots of the chaos indicators, ftmLE and SALI, as well as the LDs, large ensembles of ICs are required to reveal the structure of the phase space. Since each IC has to be integrated for some total time, producing high resolution plots can require a large amount of CPU time. Writing computer code which is as efficient as possible is, therefore, highly important for producing results. All coding for this thesis is done in Python version 3.8.8. While Python is generally not as fast as other programming languages such as C or FORTRAN 90, with the use of the Numba compiler, Python can be sped up considerably. Numba translates Python functions into machine code, optimising the performance of numerical calculations. Utilising it effectively results in a significant decrease in computational time when integrating individual orbits.

To reduce the time taken to produce results on grids of ICs we make use of the Python "multiprocessing" module. This module allows for the code to be parallelised, i.e., running different parts of the code on the individual cores of the computer simultaneously (as opposed to serial computing, where all the cores are used for one task). It is straightforward to parallelise codes for computations on grids of ICs as the grid can be split into however many cores are available, with each core running a different splitting simultaneously. The obtained results can then be joined together to form the larger set of outcomes once all computations are done. The personal computer used for our work has 12 available cores, speeding up computations when code is run in parallel, but the real advantage of parallelisation comes with access to high performance computing (HPC) clusters. An HPC cluster consists of a group of computers (nodes) acting as a single system. Running parallelised code on HPC clusters greatly decreases computational time, as each node has its own set of cores. This allows for far more cores in total than on commercially available, personal computers. All the computations in this work were performed on the Centre for High Performance Computing (CHPC) Lengau cluster [86], making use of between 24 and 240 cores, depending on the size of the job. This ensured that all results typically ran within two days of CPU time. All computer codes used during our work can be found at https://github.com/sebzimp/Masters-Project.

Chapter 3

Application of LDs to a galactic potential

To demonstrate the behaviour of the LDs and what benefits they offer in studies of phase space structures, we utilise them to study the dynamics of a Hamiltonian system which describes the motion of stars in a simple galactic model. Unless otherwise stated, the LDs are computed using the "p-norm" definition (2.63), with $p = 0.5$, both forward and backward in time.

3.1 The galactic potential

The system under consideration was previously studied for example in [2], and models the transport of stars in a galaxy model rotating around the z-axis with an angular velocity Ω_b. The system is described by a 3-dof Hamiltonian given by

$$H = \frac{1}{2}(p_x^2 + p_y^2 + p_z^2) + \Phi(x, y, z) - \Omega_b(xp_y - yp_x), \tag{3.1}$$

where

$$\Phi = \frac{-GM_1}{\sqrt{x^2 + y^2/q_a^2 + \left[a_1 + (z^2/q_b^2 + b_1^2)^{\frac{1}{2}}\right]^2}} - \frac{GM_2}{\sqrt{x^2 + y^2/q_a^2 + \left[a_2 + (z^2/q_b^2 + b_2^2)^{\frac{1}{2}}\right]^2}}, \tag{3.2}$$

is the functional form of the potential which attributes two Miyamoto disks [87], with masses M_1 and M_2, to the galaxy following [2]. The variables x, y and z are the spatial coordinates of a star in the galaxy and p_x, p_y and p_z the corresponding momenta of the star. Following the work done in previous studies of the model, such as in [2], the parameter values are set to $\Omega_b = 0.28262$, $M_1 = 2.05$, $M_2 = 25.47$, $q_a = 1.2$. $q_b = 0.9$ (q_a and q_b determine the geometry of the Miyamoto

disks), $a_1 = 0$ kpc, $a_2 = 7.258$ kpc, $b_1 = 0.495$ kpc, $b_2 = 0.520$kpc (the parameters a_1, b_1, a_2, and b_2 are scaling factors), and the gravitational constant rescaled to $G = 1$ (setting the velocity unit to 209.64 km/sec and the units of M_1 and M_2 to 10^{10} solar masses). The corresponding Hamilton's equations of motion are

$$\begin{aligned} \dot{x} &= p_x + \Omega_b y & \dot{p_x} &= -\frac{\partial \Phi}{\partial x} + \Omega_b p_y \\ \dot{y} &= p_y - \Omega_b x & \dot{p_y} &= -\frac{\partial \Phi}{\partial y} - \Omega_b p_x \\ \dot{z} &= p_z & \dot{p_z} &= -\frac{\partial \Phi}{\partial z}. \end{aligned} \tag{3.3}$$

To simplify the study of this system, we restrict our investigation to the 2-dof version, by considering motion only on the symmetry plane $z = p_z = 0$. The reduced model has the following 2-dof Hamiltonian functional form

$$H = \frac{1}{2}(p_x^2 + p_y^2) - \Omega_b(x p_y - y p_x) - \frac{GM_1}{\sqrt{x^2 + y^2/q_a^2 + \left[a_1 + b_1\right]^2}} - \frac{GM_2}{\sqrt{x^2 + y^2/q_a^2 + \left[a_2 + b_2\right]^2}}, \tag{3.4}$$

with the corresponding Hamilton's equations of motion given by

$$\begin{aligned} \dot{x} &= p_x + \Omega_b y & \dot{p_x} &= -\frac{\partial \Phi}{\partial x} + \Omega_b p_y \\ \dot{y} &= p_y - \Omega_b x & \dot{p_y} &= -\frac{\partial \Phi}{\partial y} - \Omega_b p_x. \end{aligned} \tag{3.5}$$

Since the galactic system is rotating around the z-axis at a constant angular velocity Ω_b, the dynamics can be described in the rotating frame of reference (see, for example, [88]). The restriction of this potential on the reduced model (3.4) for this rotating frame is known as the effective potential, given by

$$\Phi_{\text{eff}}(x, y) = \Phi(x, y, z = 0) - \frac{1}{2}\Omega_b^2(x^2 + y^2), \tag{3.6}$$

and its contour plot shown in Fig. 3.1. The five points shown in red are the fixed points of the system, for which

$$\frac{\partial \Phi_{\text{eff}}}{\partial x} = \frac{\partial \Phi_{\text{eff}}}{\partial y} = 0, \tag{3.7}$$

i.e., $\dot{x} = \dot{y} = \dot{p_x} = \dot{p_y} = 0$. In the study of galactic dynamics, these fixed points are commonly referred to as the Lagrange points (see, for example, Section 3.1.4 of [89]). The Lagrange points L_1 and L_2 are saddle points of the effective potential, while L_3 is a local minimum, and L_4 and L_5 are local maxima. The saddle

Lagrange points L_1 and L_2 define a critical value for the energy of the system, $E_C = -4.246969670045883$, as when the energy is higher than E_C, stars can escape from the interior region of the potential around the local minimum L_3.

The escape of orbits from an interior region of a potential is an important feature in a variety of dynamical systems. LDs have been applied extensively to study this phenomenon in transition state theory (see, for example, [90, 91, 92]), which models the quantities of reactants and products in a chemical reaction using the location of an orbit in the phase space (for an overview of this topic see [93] and references therein). Of particular interest when studying escapes from a galactic potential are the Lyapunov orbits [94], which are highly unstable periodic orbits surrounding the saddle points of the potential. If an orbit crosses a Lyapunov orbit with a velocity pointing outwards, then that orbit is classified as having escaped the interior region of the galaxy [95]. We demonstrate in Section 3.3 how the LDs are utilised to identify the location of the Lyapunov orbits as well as their associated stable and unstable manifolds of the galactic model.

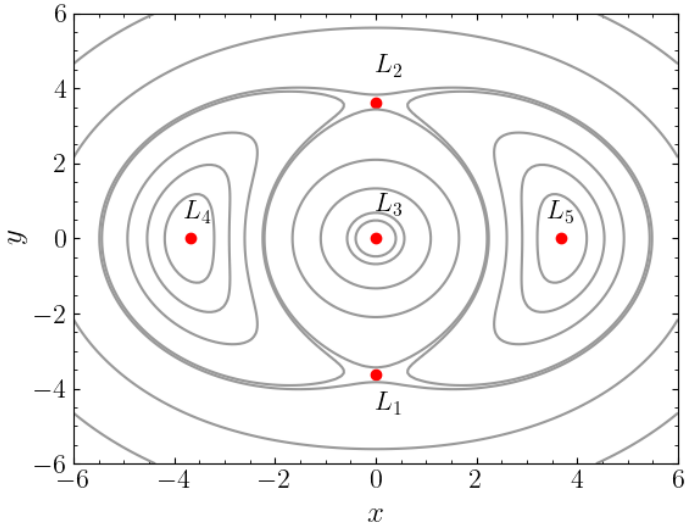

Figure 3.1: Contour plot of the effective potential (3.6) on the configuration space of the Hamiltonian system (3.4). The Lagrange points of this potential are denoted as red dots.

The Hamiltonian system (3.4) is not separable (the kinetic and potential energies are explicitly dependent on both the coordinates and conjugate momenta), so symplectic integrators cannot be straightforwardly applied to cap the relative energy error (2.19). Instead, we use the RK6 scheme (see Section 2.2.1) from [15]. Unlike the case of symplectic integrators, the relative energy error grows linearly

in time for the RK6 method. Using an integration time step of $h = 0.025$ keeps the E_r (2.19) of the orbits of this system below a threshold of 10^{-7} for integration times up to $\tau = 10^4$, so our numerical approximations to the solutions of this system are accurate.

3.2 Visualisation of the phase space dynamics of the 2-dof galactic model without escapes

Let us now start our analysis of the system (3.4) when the energy is slightly below the critical energy value at $E = -4.3 < E_C$ and escapes are not energetically permitted. We reiterate that one of the primary objectives of our work is to study the escape of orbits through L_1 and L_2, which are on the line $x = 0$, when the energy is above E_C. For this reason, we investigate the surface of section given when $x = 0$ and $\dot{x} > 0$. In Figs. 3.2(a) and (b) we show the PSS and the SALI plots for this subspace respectively. In particular, we compute the SALI on a grid of $1,001 \times 1,001$ evenly spaced ICs on the intervals $y \in [-3.5, 3.5]$ and $p_y \in [-3, 3]$ up to a final integration time of $\tau = 10^4$. We identify from the PSS [Fig. 3.2(a)] a periodic orbit in the large regular region, surrounded by the cross-sections of tori on which regular motion occurs. The chaotic regions are characterised by the "randomly" distributed dots in the PSS and the purple coloured regions in the SALI colour plot [Fig. 3.2(b)] for which SALI $< 10^{-8}$. In both panels of Fig. 3.2, we also observe smaller islands of regular motion in the chaotic sea, which are revealed more clearly through the use of a SALI plot than a PSS plot. In neither of these panels are the manifolds of the system shown.

To reveal the phase space structures in the chaotic regions, we make use of the LDs. We compute the LDs on the same grid of ICs as was used for the SALI computations in Fig. 3.2(b). Because we do not know *a priori* the integration time τ necessary for the LDs to clearly highlight the prominent manifolds, some work is required to find an appropriate τ value. In Fig. 3.3 the LD and LD gradient plots are shown for three different integration times: $\tau = 50$, 100, and 200. For relatively short integration times, such as $\tau = 50$ [Figs. 3.3(a) and (b)] some of the invariant curves around the periodic orbit in the regular region can be seen as high LD gradient values, but there are no well-defined manifolds in the chaotic regions. At $\tau = 100$ [Figs. 3.3(c) and (d)], some of the manifolds in the chaotic regions can now be seen as dark lines in the LD gradient plot. By increasing the integration time further to $\tau = 200$ [Figs. 3.3(e) and (f)], we observe a corresponding increase in the number of manifolds in the chaotic region such that it becomes difficult to identify individual manifolds. This is due to the fact that unstable periodic orbits are dense in chaotic regions, resulting in higher order periodic orbits and their

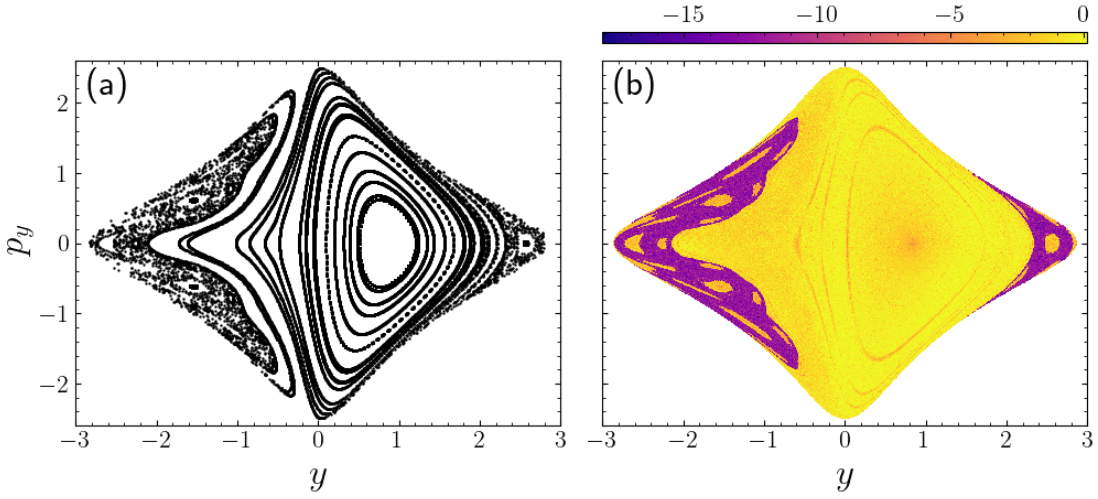

Figure 3.2: (a) The PSS of the galactic system (3.5) on the plane $x = 0$, $\dot{x} > 0$ at an energy $E = -4.3$. (b) The $\log_{10}$ SALI colour plot for the same plane as (a) for a grid of $1,001 \times 1,001$ ICs evenly distributed on the intervals $y \in [-3.5, 3.5]$ and $p_y \in [-3, 3]$, integrated for a total integration time of $\tau = 10^4$. The ICs are coloured according to their $\log_{10}$ SALI value using the colour scale at the top of the panel.

manifolds causing discontinuities in the LD gradient plot when the integration time is increased sufficiently. We will explore the relation between chaos and LDs further in Chapter 4, where we will use diagnostics based on the LDs to characterise orbits as either regular or chaotic.

From the results presented in Fig. 3.3, we identify $\tau = 100$ as the integration time which shows the manifolds in the LD gradient plot the clearest. To extract and visualise the shape of the manifolds, we zoom in on the chaotic regions we see in Fig. 3.2(b). In Figs. 3.4(a) and (b) we show the LD gradient at $\tau = 100$ (of the combined forward and backward LDs) for a grid of 1001×1001 evenly distributed ICs on the intervals, $y \in [-3, -1]$, $p_y \in [-2, 2]$ as well as $y \in [1.5, 3]$, $p_y \in [-1.2, 1.2]$ respectively.

The position of the manifolds for this grid of ICs corresponds to grid points where the LD gradient scalar field values are high (see Section 2.4). We can therefore extract the stable manifolds by considering all ICs of Figs. 3.4(a) and (b) for which the gradient of the forward LDs are above an appropriate value. Likewise, we can extract the unstable manifolds by considering the backward LD gradient values. Setting both the forward and backward LD gradient threshold to $M_{grad} > 1$, we show in Figs. 3.4(c) and (d) the stable (red) and unstable (blue) manifolds from the ICs considered in Figs. 3.4(a) and (b) respectively. The

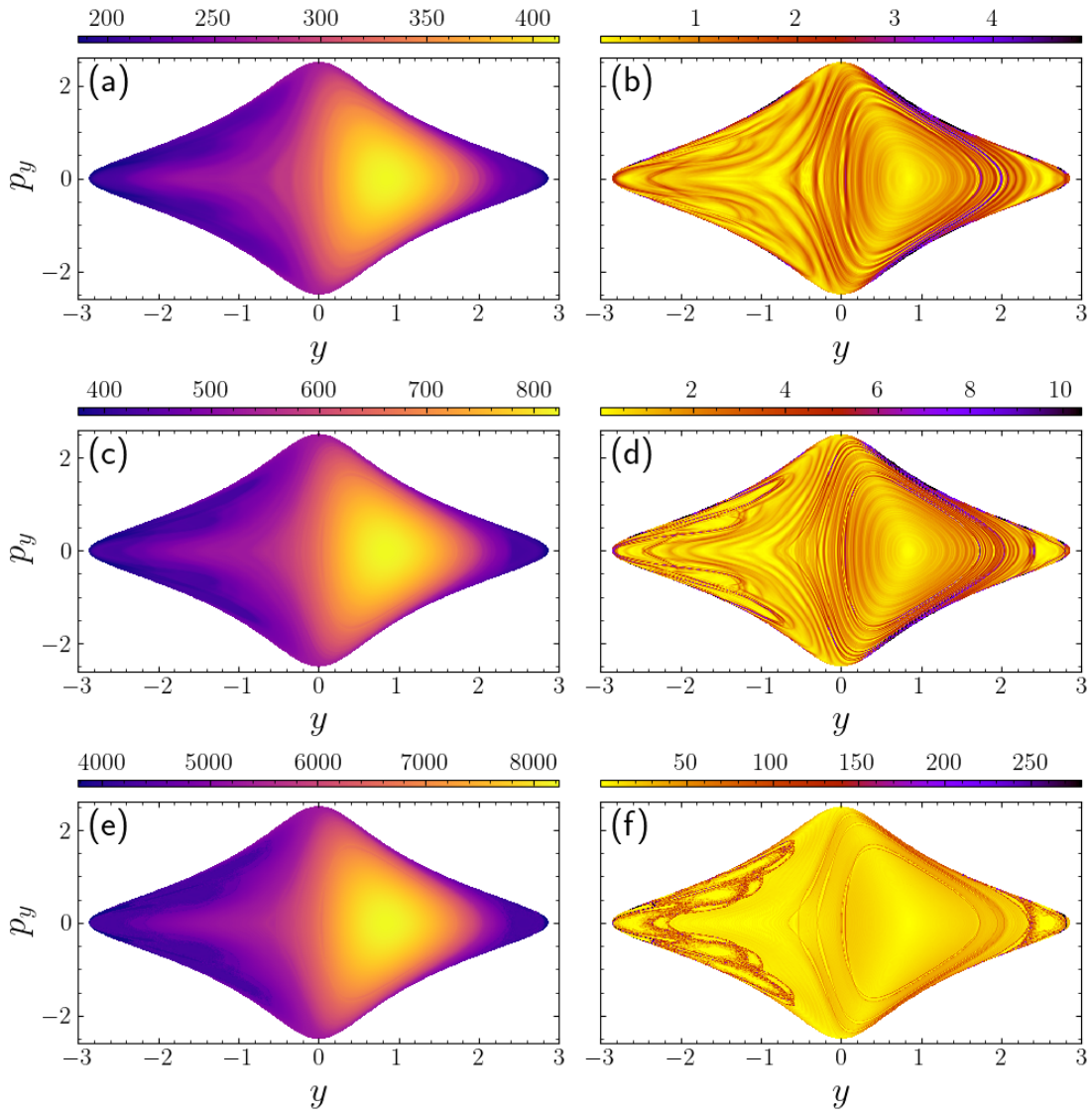

Figure 3.3: Results obtained for the same ICs as considered in Fig. 3.2(b). The ICs are coloured according to their LD values at $\tau = 50$ (a), $\tau = 100$ (c) and $\tau = 200$ (e) as well as their corresponding LD gradient in (b), (d) and (f) respectively, using the colour scale at the top of each panel.

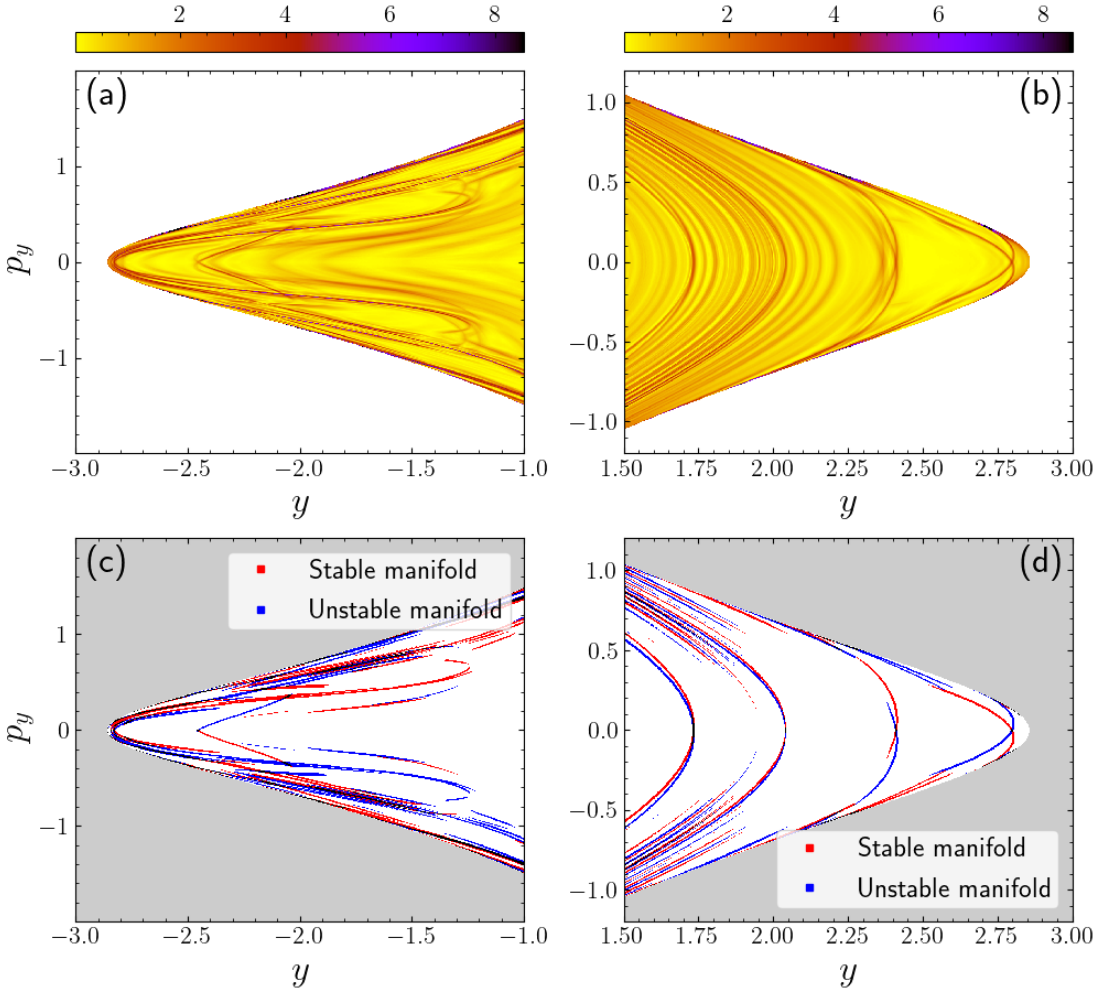

Figure 3.4: Results obtained for the 2-dof galactic model (3.5) at an energy of $E = -4.3$ on the subspace defined by $x = 0$, $\dot{x} > 0$. (a) A grid of $1,001 \times 1,001$ evenly distributed ICs on the intervals $y \in [-3, -1]$ and $p_y \in [-2, 2]$ in the subspace coloured according to the value of the gradient of the combined forward and backward LDs with a final integration time of $\tau = 100$ using the colour scale at the top of the panel. (b) Similar to (a) but for ICs on the intervals $y \in [1.5, 3]$ and $p_y \in [-1.2, 1.2]$. (c) The set of points considered in (a) for which the gradient of the forward or backward LDs is greater than 1 (coloured red and blue respectively). The region coloured in grey is the area which is not energetically permissible. (d) Similar to (c) but for the set of ICs considered in (b). We note that the red and blue curves in (c) and (d) correspond to stable and unstable manifolds of the system.

energetically forbidden regions are coloured in grey in these two plots. From these results, we can clearly visualise the complicated phase space structures created by the manifolds using relatively short CPU time. This demonstrates that the LDs can be used to efficiently study the motion of stars in the interior region of our galactic model 3.4.

3.3 Investigating the dynamics for energies permitting the escape of orbits

Let us now increase the system's energy further to $E = -4.24 > E_C$. At this higher energy, orbits can now escape the potential well through regions around the Lagrange saddle points L_1 and L_2. Plotting the PSS on the plane $x = 0$, $\dot{x} > 0$ in Fig. 3.5(a), we see orbits that have escaped the interior region as well as some forming bell-type curves [96]. Zooming in on the PSS in Fig. 3.5(b), we observe the regular and chaotic dynamics at the centre of the potential. These dynamics are shown again in the $\log_{10}$ SALI colourplot of this plane shown in Fig. 3.5(c). We note that the SALI was calculated on a grid of $1,001 \times 1,001$ evenly spaced ICs on the intervals $y \in [-4, 4]$, $p_y \in [-3, 3]$ for a total integration time of $\tau = 10^4$. Compared to the SALI plot of the system at $E = -4.3$ [Fig. 3.2(b)], we now no longer see regular islands within the chaotic sea, with the chaotic orbits escaping from the potential well.

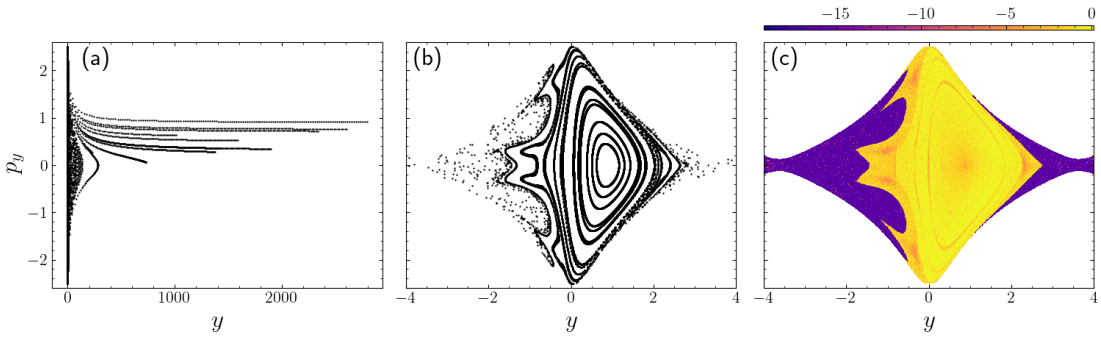

Figure 3.5: (a) The PSS of the galactic model (3.5) on the plane $x = 0$, $\dot{x} > 0$ at an energy of $E = -4.24$. (b) Zoomed in image of (a) on the intervals $y \in [-4, 4]$ and $p_y \in [-2.5, -2.5]$. (c) The $\log_{10}$ SALI colour plot (using the colour scale at the top of the panel) for the same plane as (a) for a grid of $1,001 \times 1,001$ ICs on the same intervals as (b), integrated for a total integration time of $\tau = 10^4$.

To visualise the manifold structure of the Lyapunov orbits governing the escapes through the bottlenecks, we use LDs. Using a fixed integration time of

$\tau = 40$, the LD and LD gradient for the same grid of ICs as Fig. 3.5(c) are shown in Figs. 3.6(a) and (b) respectively. We note that while the possible escape of orbits from the potential well could lead to blowups in the values of the LDs, we find that for $\tau = 40$ the LDs clearly display the phase space without any extremal LD values. In the chaotic regions around the bottlenecks, manifolds corresponding to the Lyapunov orbits can now be seen. These are characterised by the high magnitude values (dark curves) of the LD gradient plot [Fig. 3.6(b)]. The bottlenecks are however very narrow at this energy level, so it is difficult to visually identify the manifolds in Fig. 3.6(b).

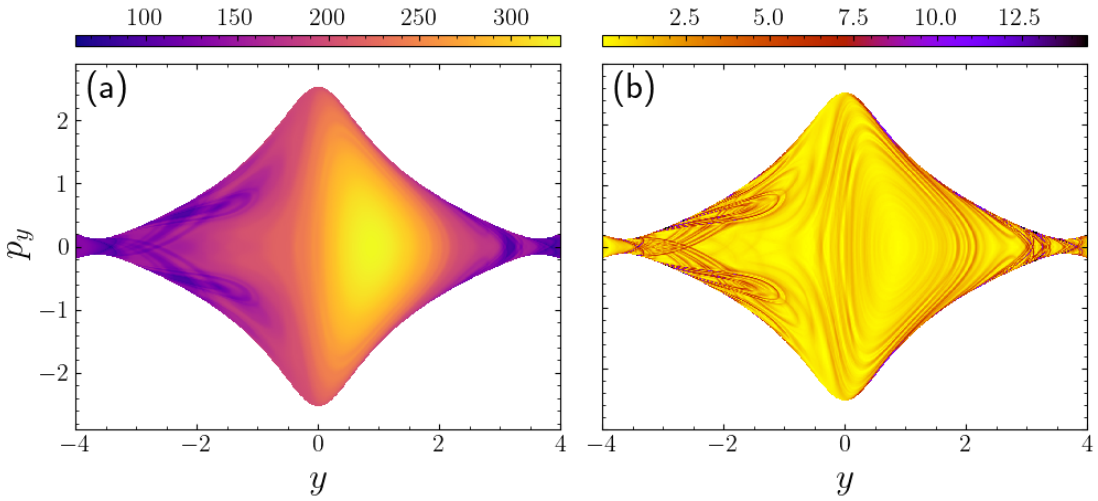

Figure 3.6: Results obtained for the same grid of ICs as in Fig. 3.5(c), with the ICs coloured according to their LD values at an integration time of $\tau = 40$ (a) and the corresponding LD gradient (b) using the colour scale at the top of the panels.

Enhancing on the two bottlenecks, we compute the gradients of the forward and backward LDs for a grid of $1,001 \times 1,001$ evenly distributed ICs on the intervals $y \in [-4, -1]$, $p_y \in [-1, 1]$ and $y \in [2, 4]$, $p_y \in [-1, 1]$. In Figs. 3.7(a) and (b) we show the two respective grids of ICs coloured according to the gradient of the combined forward and backward LDs for $\tau = 40$, using the colour scales at the top of each panel.

In these two panels, we can identify the structures created by the manifolds as regions where the LD gradient is high [a high LD gradient corresponds to the darker regions in Figs. 3.7(a) and (b) as well as the location of the manifolds]. We categorise points where the gradient of the forward/backward LD is greater than 1 as the stable/unstable manifolds respectively. The points from Fig. 3.7(a) which are identified as part of the stable (red points) and unstable (blue points) manifolds are in shown Fig. 3.7(c). Figure 3.7(d) shows the manifolds for the ICs

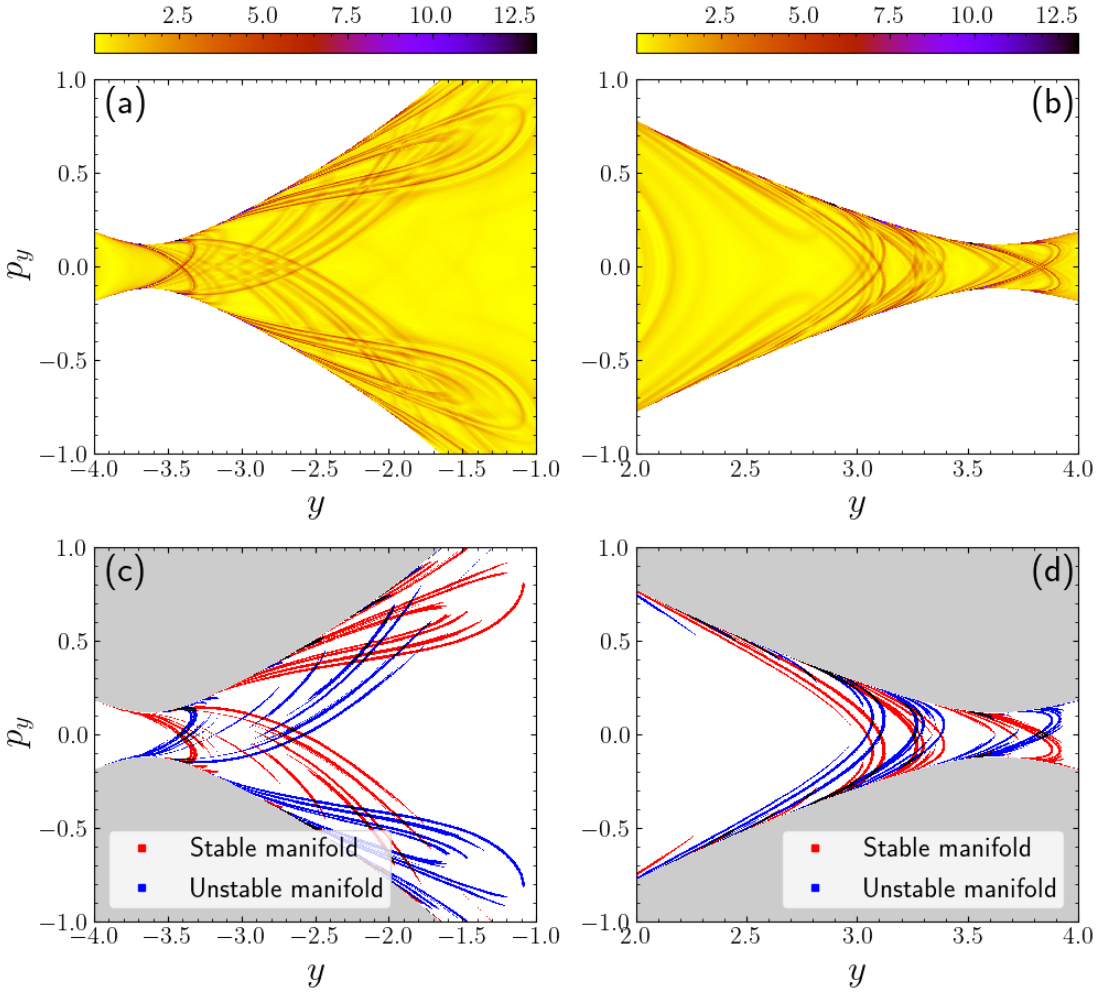

Figure 3.7: Results obtained for the 2-dof galactic model (3.5) at an energy of $E = -4.24$ on the subspace defined by $x = 0$, $\dot{x} > 0$. (a) A grid of $1,001 \times 1,001$ evenly distributed ICs on the intervals $y \in [-4, -1]$ and $p_y \in [-1, 1]$ in the subspace, coloured according to the value of the gradient of the combined forward and backward LDs with a final integration time of $\tau = 40$, using the colour scale at the top of the panel. (b) Similar to (a) but for ICs on the intervals $y \in [2, 4]$ and $p_y \in [-1, 1]$. (c) The stable (red curves) and unstable (blue curves) manifolds extracted from the LD gradient (with a threshold of the forward or backward LD gradients $M_{grad} > 1$) for the set of points considered in (a). The region coloured in grey is the area which is not energetically permissible. (d) Similar to (c) but for the set of ICs considered in (b).

from Fig. 3.7(b). In both Figs. 3.7(c) and (d), the region which is not energetically permissible is coloured grey. The manifolds identified by the LDs clearly display the complicated phase space structures responsible for the escape of orbits from the potential well.

Instead of the plane defined by $x = 0$, $\dot{x} > 0$, the manifolds can also be studied on the system's configuration space. The configuration space of the galactic model (3.4) represents the positions of the stars (their x and y coordinates) and as such is commonly used when investigating the escapes of orbits from some interior region. Identifying the position of the Lyapunov orbits and visualising their associated manifolds on the configuration space is therefore extremely important when studying the dynamics of galactic systems. We will demonstrate how LDs can be used to uncover the structures in the configuration space, with the restriction that $E = -4.24$, $\dot{y} = 0$, i.e., $p_y = \Omega_b x$, and $p_x > 0$ is determined from the system's Hamiltonian (3.4). In Figs. 3.8(a) and (b) we colour a grid of $1,001 \times 1,001$ ICs evenly spaced on the intervals $x, y \in [-5, 5]$ according to their LD and LD gradient values at $\tau = 40$ respectively. From the LD gradient, we can see the manifolds at the top and bottom bottlenecks as purple and black lines.

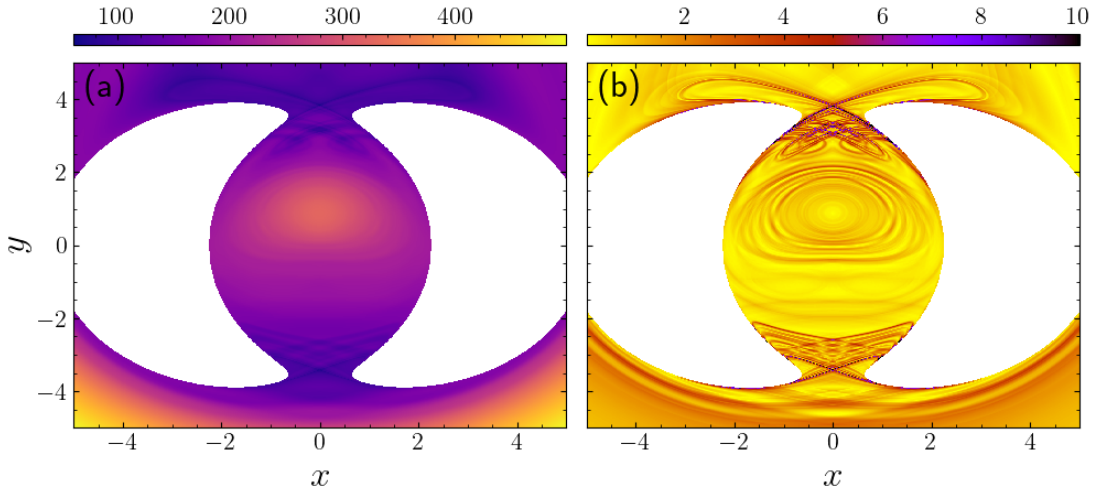

Figure 3.8: (a) The LD colour-plot of the galactic model (3.5) on the configuration space $\dot{y} = 0$, $\dot{x} > 0$ at an energy of $E = -4.24$ for a grid of $1,001 \times 1,001$ ICs on the intervals $x, y \in [-5, 5]$, with a final integration time of $\tau = 40$. (b) The corresponding LD gradient of (a).

We zoom in on the bottleneck at the top of the configuration space, showing the LD and LD gradient on a grid of $1,001 \times 1,001$ evenly spaced ICs on the intervals $x \in [-4, 4]$, $y \in [3.3, 5]$ for $\tau = 40$ in Figs. 3.9(a) and (b) respectively. We show the manifolds which are extracted from the LD gradient by setting a

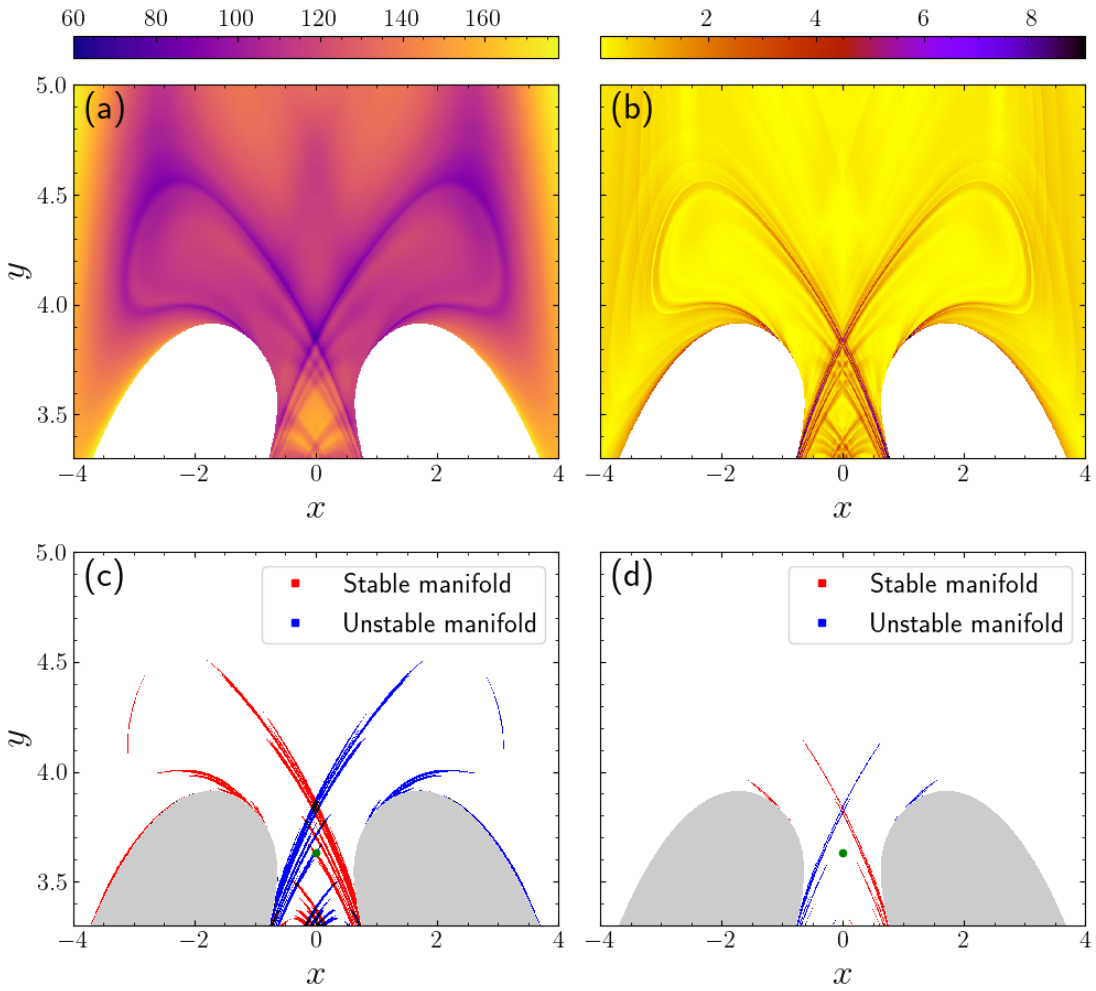

Figure 3.9: Results obtained for the 2-dof galactic model (3.5) at an energy of $E = -4.24$ for a grid of $1,001 \times 1,001$ evenly distributed ICs on the intervals $x \in [-4, 4]$ and $y \in [3.3, 5]$ on the subspace defined by $\dot{y} = 0$, $\dot{x} > 0$. The ICs are coloured according to their LD (a) and LD gradient (b) values, computed for a final integration time of $\tau = 40$. (c) The stable (red curves) and unstable (blue curves) manifolds extracted from the LD gradient for the set of points considered in (a), using an LD gradient threshold of $M_{grad} > 1$. The region coloured in grey is the area which is not energetically permissible and the green dot corresponds to the Lagrange point. (d) Similar to (c), but for an LD gradient threshold value of $M_{grad} > 3$.

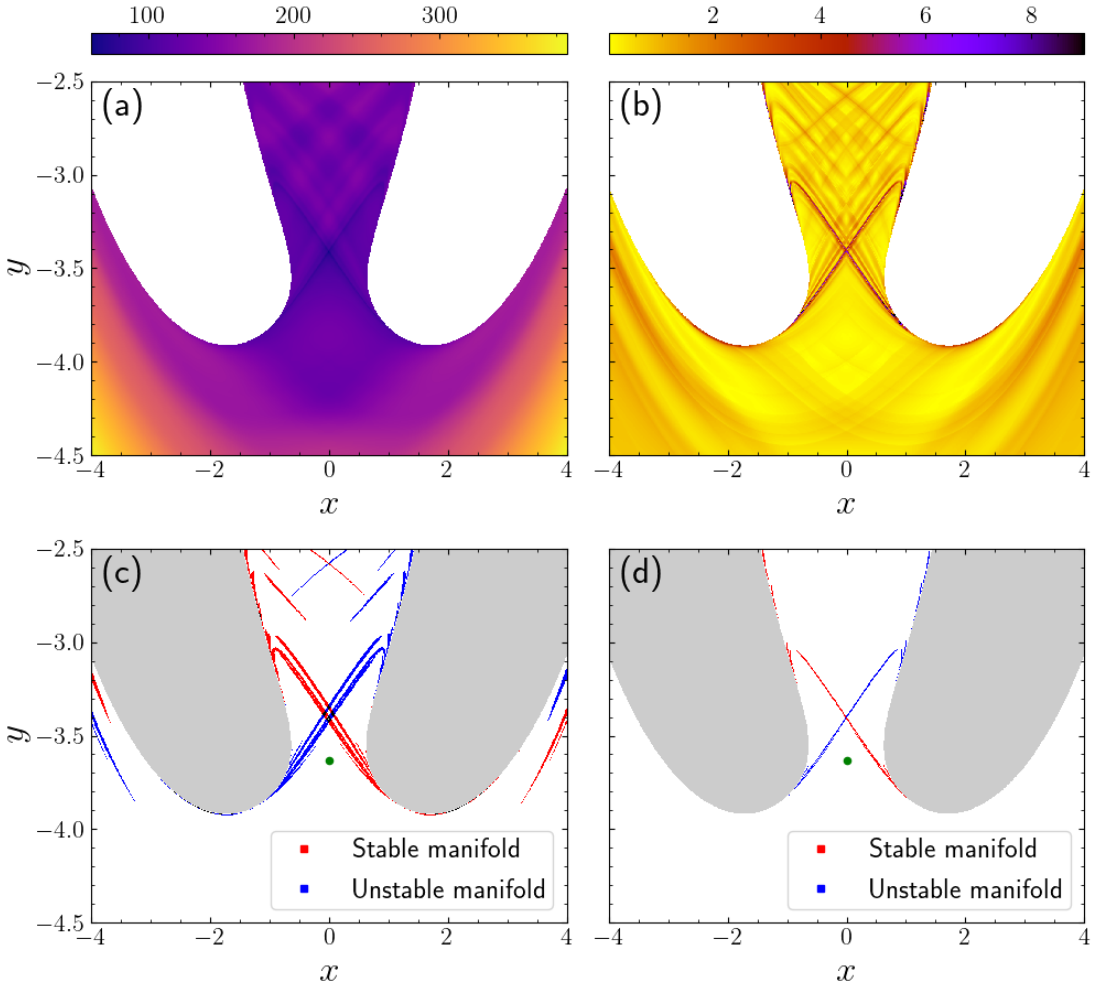

Figure 3.10: Similar to Fig. 3.9, but for a grid of $1,001 \times 1,001$ evenly distributed ICs on the intervals $x \in [-4, 4]$, $y \in [-4.5, -2.5]$.

threshold of $M_{grad} > 1$ in Fig. 3.9(c). The red curves in Fig. 3.9(c) correspond to the stable manifolds, the blue curves to the unstable manifolds; the Lagrange point L_1 is shown as a green point and the region which is not energetically permitted is shown as grey. From the results presented in Fig. 3.9(c), we can clearly visualise the complicated manifold structure governing the escape of stars. Let us recall from Section 2.1.1, that the location of an unstable periodic orbit is at the intersection of its associated stable and unstable manifolds. In Fig. 3.9(c) there are too many intersecting manifolds to identify the position of the Lyapunov orbit on the configuration space. However, since the threshold for the LD gradient we chose to extract the manifolds, $M_{grad} > 1$, was arbitrary, we can adjust this value, so we see only the most prevalent phase space structures. If we instead consider only the points with an LD gradient $M_{grad} > 3$, we extract the manifolds shown in Fig. 3.9(d) [the same colouring scheme as Fig. 3.9(c) is used]. In this figure, we see a far less complicated manifold structure, with only one intersection of the stable and unstable manifolds occurring at $(x, y) \approx (0, 3.83)$. We will show that this is a good estimation of the Lyapunov orbits' location on the configuration space in Section 3.4.

We can perform a similar analysis to the one of Fig. 3.9, for the bottleneck at the bottom of the configuration space (Fig. 3.8). In Figs. 3.10(a) and (b) we respectively show the LD and LD gradient for a grid of $1,001 \times 1,001$ evenly spaced ICs on the intervals $x \in [-4, 4]$, $y \in [-4.5, -2.5]$. The manifolds obtained by setting thresholds for the LD gradient at $M_{grad} > 1$ and $M_{grad} > 3$ are shown in Figs. 3.10(c) and (d) respectively. We clearly see in Fig. 3.10(c) the manifolds of the system forming the "skeleton" of the dynamics, similar to Fig. 3.9(c). In Fig. 3.10(d), we identify the position of the Lyapunov orbit at the lower bottleneck as the intersection of the stable and unstable manifolds at $(x, y) \approx (0, -3.40)$. From the results presented in Figs. 3.9 and 3.10, we can identify both the structure of the manifolds governing the escape of stars from the potential well, and have an estimation of the position of the Lyapunov orbit.

3.4 Computation of the Lyapunov orbits

Due to the grid size of the LDs only an approximate guess of the two Lyapunov orbits' positions on the configuration space can be made. To verify that the points identified in Figs. 3.9 and 3.10 are a good estimation of the locations of the Lyapunov orbits and to find more accurate approximations, we implement a multidimensional Newton-Raphson method for finding periodic orbits.

Let us give here a brief outline of this scheme. We start with an initial guess on the configuration space, and evolve this IC until an intersection with the configuration space defined by $\dot{y} = 0$, $\dot{x} > 0$ is found at $t = t_C$. The same method

for finding the accurate intercept of an orbit with a plane for the computation of the PSS (Section 2.3.1) is used to find the location of this intersection accurately. We note that the resulting map is a Poincaré map (Section 2.1.1), for which a periodic orbit is a fixed point. To find the location of this fixed point we use the multidimensional Newton-Raphson's method with the following form

$$\mathbf{x}_{i+1}(0) = \mathbf{x}_i(0) - (A - \mathbb{I}_2)^{-1}(\mathbf{x}_i(t_C) - \mathbf{x}_i(0)), \quad i = 1, 2, \ldots, \tag{3.8}$$

where $\mathbf{x}_i$ is the i-th updated guess of the location of the periodic orbit, $\mathbb{I}_2$ the 2×2 identity matrix, and A a matrix which we compute at every iteration in the following manner. Taking two orbits which are initially close to $\mathbf{x}_i(0)$ and letting $\mathbf{w}_{1,2}(0)$ and $\mathbf{w}_{1,2}(t_C)$ be the deviation vectors from $\mathbf{x}_i$ to these orbits at $t = 0$ and $t = t_C$ respectively, the matrix A satisfies

$$\mathbf{w}_{1,2}(t_C) = A \cdot \mathbf{w}_{1,2}(0). \tag{3.9}$$

We let $\mathbf{w}_1(0) = (\Delta, 0)^T$, $\mathbf{w}_2(0) = (0, \Delta)^T$, $\mathbf{w}_1(t_C) = (a, b)^T$, and $\mathbf{w}_2(t_C) = (c, d)^T$, where Δ, a, b, c, and d are some real constants and compute A as

$$A = \frac{1}{\Delta} \begin{pmatrix} a & b \\ c & d \end{pmatrix}, \tag{3.10}$$

from which we update our approximation of the location of the periodic orbit until some desired tolerance for $|\mathbf{x}(t_C) - \mathbf{x}(0)|$ is reached.

From the LD plots in Figs. 3.9 and 3.10, we have approximate locations of the Lyapunov orbits' intersections with the configuration space at $(x, y) \approx (0, 3.83)$ and $(x, y) \approx (0, -3.40)$. We use these approximate positions as our initial guess for the periodic orbit finding algorithm outlined above. The deviation orbits used are $\mathbf{w}_1 = (10^{-12}, 0)^T$ and $\mathbf{w}_2 = (0, 10^{-12})^T$, with the algorithm being iterated until a desired tolerance of 10^{-14} is reached. We find the Lyapunov orbits to be located at

$$(x, y) = (-2.2948185113096246 \times 10^{-5}, 3.8445181482103776)$$

and

$$(x, y) = (-4.501505716185021 \times 10^{-5}, -3.4087110481474063),$$

demonstrating that the information extracted from the LDs gave a good estimation of the Lyapunov orbits' positions.

In Fig. 3.11 we show the projection of the evolution of the Lyapunov orbits on the configuration space with the energetically forbidden region shown in grey, as well as the Lagrange points (green points) surrounded by the Lyapunov orbits. We see that the Lyapunov orbits form ellipses surrounding the Lagrange points, as we would expect from the discussion in Section 3.1.

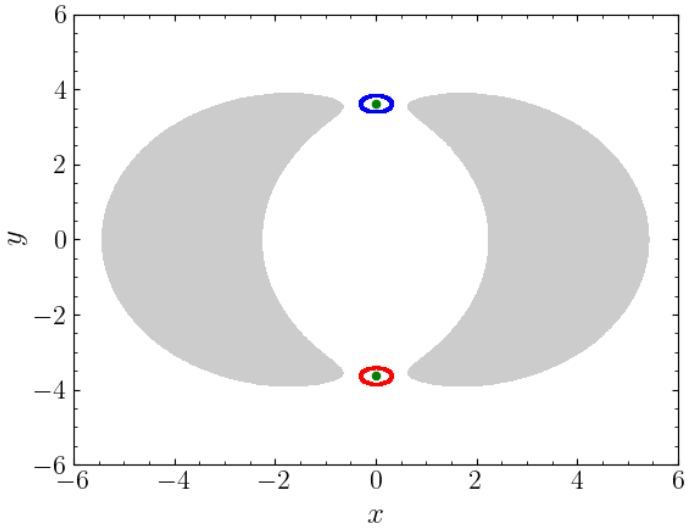

Figure 3.11: The projections of the two Lyapunov orbits (red and blue circles) on the plane of the galactic potential defined by $\dot{y} = 0$, $\dot{x} > 0$ at an energy of $E = -4.24$. The Lagrange points L_1 and L_2 are shown as the two green points, with the energetically forbidden region of the plane shown in grey.

In this study we have demonstrated the ability of LDs to visualise the manifolds of the galactic model 3.4 when the system does not allow for escapes [Fig. 3.4] and when orbits can exit the interior region [Figs. 3.7, 3.9(c) and 3.10(c)]. Furthermore, we use the LDs to give good estimations of the Lyapunov orbits' locations [see the discussion of Figs. 3.9(d) and 3.10(d)]. These phase space structures are crucial in studying the motion of stars in galactic models, with the LDs offering a straightforward-to-implement and computationally-quick method of visualising them.

Chapter 4

Chaos detection diagnostics based on the LDs of nearby orbits

As part of the discussion in Chapter 3 and the results presented in Fig. 3.3, we demonstrated that at long integration times, we can visually identify chaotic regions of the phase space as where the LD gradient is large. This is due to the manifolds of the dense periodic orbits in the chaotic regions being revealed at later times. Furthermore, in [97] it was demonstrated that LD values were "smoother" in regular regions than in chaotic ones. To demonstrate this, we consider a line of $2,500$ ICs for the Hénon-Heiles system (2.16) at $H = 1/8$, with $x = p_y = 0$, $p_x > 0$ on the interval $y \in [-0.5, 0.75]$. In Fig. 4.1(a) we show the PSS of the system for $x = 0$ and $p_x > 0$ and denote the ICs on $p_y = 0$ as the red, horizontal line. From the PSS we can pick which ICs on this line are regular and which ones are chaotic, but as a more accurate identification of the orbits' natures, we compute the SALI at $\tau = 10^5$, presenting these results in Fig. 4.1(b). Let us recall from Section 2.3.4 that the SALI characterises an orbit as chaotic if the SALI value is $\log_{10} \mathrm{SALI} \approx -16$ and regular if the SALI is a positive constant, so we indicate an appropriate threshold of $\log_{10} \mathrm{SALI} = -8$ as a horizontal red line in Fig. 4.1(b). We show the LD values of the ICs on the line, computed using the "p-norm" definition with $p = 0.5$ for a final integration time $\tau = 1,000$, in Fig. 4.1(c). In this figure we see that for the ICs which we categorise as belonging to regular orbits, from the results of the PSS [Fig. 4.1(a)] and the SALI plot [Fig. 4.1(b)], the LD values have smooth variations, while the LDs of ICs in chaotic regions vary erratically. This phenomenon is due to regular orbits which are initially nearby each other behaving similarly, and therefore having close LD values, while chaotic orbits diverge exponentially (with their deviation vectors growing in the direction corresponding to the mLCE), resulting in their LD values being unrelated.

Following the observation that chaotic regions of the Hénon-Heiles system can be visually identified from the LDs, we develop techniques for a global method to

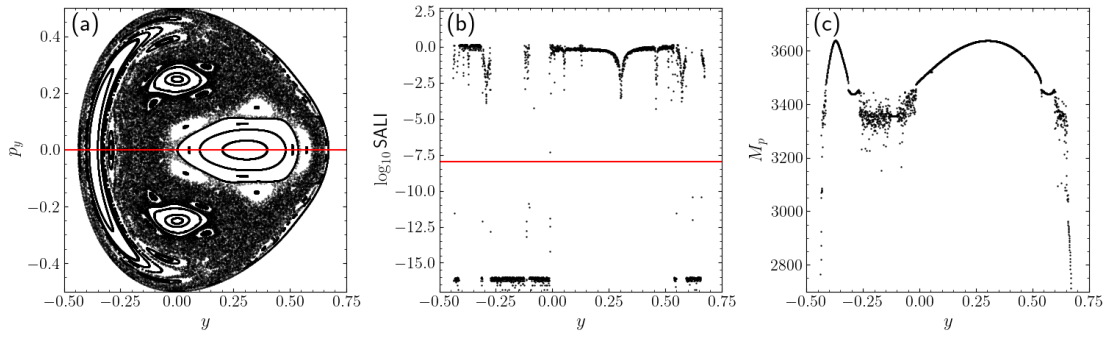

Figure 4.1: (a) The PSS of the Hénon-Heiles system at $H = 1/8$ for $x = 0$, $p_x > 0$. The line $p_y = 0$ is indicated by the red, horizontal line. (b) The $\log_{10}$ SALI values at time $\tau = 10^5$ of $2,500$ ICs on the red line in (a). To discriminate between ICs of regular and chaotic orbits, the threshold $\log_{10}$ SALI is shown as a red line. (c) The LD values at an integration time of $\tau = 1,000$ of the ICs considered in (b).

quantitatively characterise orbits as either regular or chaotic, using only computations of LDs. The newly developed chaos diagnostics are the difference and ratio of the LDs of nearby orbits, which we introduced in our work [8], as well as a finite difference approximation of the second spatial derivative of the LDs which was introduced in [3] and later used in [98]. We investigated the application of these three chaos detection methods to the Hénon-Heiles system and the 2D standard map in [8] and to a 4D symplectic map in [9].

The quantitative LDs-based chaos detection indices make use of the LDs of neighbouring orbits to characterise chaos. For an orbit with IC $\mathbf{x}_0$ in an ND phase space of a dynamical system, a set of neighbouring orbits is given by

$$\mathbf{y}_{\pm}^{(i)} = \mathbf{x}_0 \pm \sigma^{(i)} \hat{\mathbf{e}}_i, \quad i = 1, 2, \ldots, N, \tag{4.1}$$

where $\sigma^{(i)}$ is the grid spacing between ICs in the i-th direction of the phase space and $\hat{\mathbf{e}}_i$ is the i-th base unit vector. If we consider an orbit and its nearest neighbours in an $(n \leq N)$D subspace of the phase space, the difference of the LDs of nearby orbits, D_L^n, is defined as

$$D_L^n(\mathbf{x}_0, \tau) = \frac{1}{2n} \sum_{i=1}^{n} \frac{|M(\mathbf{x_0}, \tau) - M(\mathbf{y}_+^{(i)}, \tau)| + |M(\mathbf{x_0}, \tau) - M(\mathbf{y}_-^{(i)}, \tau)|}{M(\mathbf{x_0}, \tau)}, \tag{4.2}$$

where M is the LD computed using a generic norm, τ the final integration time at which the LDs are evaluated, and we refer to n as the order of the index. We also define the ratio of the LDs of nearby orbits, R_L^n, as

$$R_L^n(\mathbf{x}_0, \tau) = \left| 1 - \frac{1}{2n} \sum_{i=1}^{n} \frac{M(\mathbf{y}_+^{(i)}, \tau) + M(\mathbf{y}_-^{(i)}, \tau)}{M(\mathbf{x_0}, \tau)} \right|. \tag{4.3}$$

The third indicator we will discuss in this thesis is related to the finite difference second spatial derivative of the LD scalar field. Although it was initially introduced in [3] as the $||\Delta LD||$, in order to be consistent with the notation of (4.2) and (4.3) and to emphasise the order of the index, we rename this to the S_L^n with the following functional form

$$S_L^n(\mathbf{x}_0,\tau) = \frac{1}{n}\sum_{i=1}^{n}\left|\frac{M(\mathbf{y}_i^+,\tau) - 2M(\mathbf{x}_0,\tau) + M(\mathbf{y}_i^-,\tau)}{(\sigma^{(i)})^2}\right|. \tag{4.4}$$

We note that we introduced the factor of $1/n$ in the definition of the S_L^n to normalise the quantity with respect to the dimensions used in the indicators' computation.

The three LD based indicators (4.2), (4.3), and (4.4) quantify the smoothness of the LD field at an IC, with smaller index values corresponding to smooth behaviour and higher values to more erratic variations. In Figs. 4.2(a)-(c) we present the $\log_{10} D_L^1$ (4.2), $\log_{10} R_L^1$ (4.3), and $\log_{10} S_L^1$ (4.4) values for the ICs on the line considered in Fig. 4.1 respectively. To compute the indices, the LD values shown in Fig. 4.1(c) were used, setting the grid spacing between neighbouring ICs to $\sigma = 5 \times 10^{-4}$. From Fig. 4.2, we see that the chaotic ICs [which we identify as the ICs with SALI values below 10^{-8} from Fig. 4.1(b)] correspond to higher values for the LD based chaos quantifiers ($\log_{10} D_L^1 > -3, \log_{10} R_L^1 > -3.5$, and $\log_{10} S_L^1 > 7$) and regular ICs to lower values. We can use the difference in indicator magnitude to quantitatively distinguish between regular and chaotic behaviour for these ICs and, since this behaviour holds in general (which we will demonstrate in this chapter), for other dynamical systems as well.

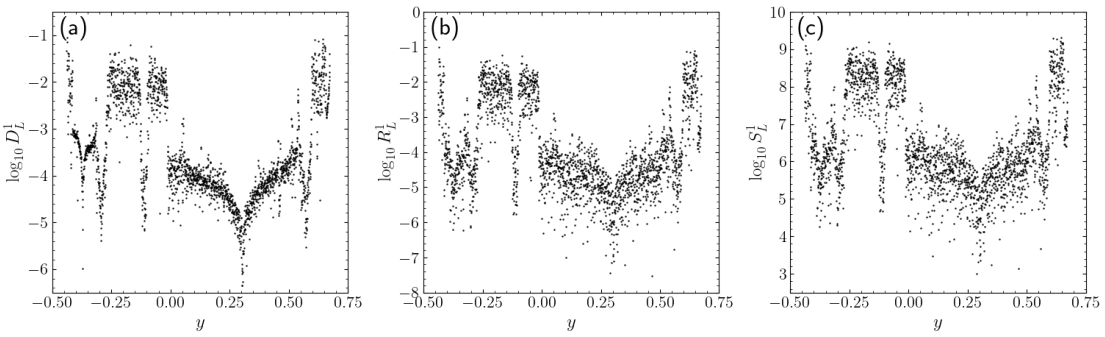

Figure 4.2: The values of the $\log_{10} D_L^1$ (a), $\log_{10} R_L^1$ (b) and $\log_{10} S_L^1$ (c) for the ICs and LDs considered in Fig. 4.1(c).

A variety of factors, such as the grid spacing σ, final integration time (or number of iterations for maps) τ/T, and the order n used in the computations of the indices, can affect how an orbit is characterised. We will discuss the impact of these factors on the accuracy of these indicators later in this chapter. Let us

remark that we only compute the forward LDs to evaluate the indicators, since the backward LDs do not offer any additional information on the chaoticity of orbits.

4.1 Application of the LDs-based chaos diagnostics to the Hénon-Heiles system

Let us now demonstrate the behaviour of the D_L^n (4.2), R_L^n (4.3), and S_L^n (4.4) indices for a low-dimensional Hamiltonian system, using the Hénon-Heiles system (2.16) as a test case. We start our analysis of the indicators by considering a regular and chaotic orbit of the model.

In Fig. 4.3(a) we show the PSS of the Hamiltonian (2.16) at $H = 1/8$ on the cross-section $x = 0$, $p_x > 0$. The light-blue and red points correspond to the intersections of a regular and chaotic orbit respectively, while the grey points belong to various other orbits. The IC of the regular orbit is $y = 0.05$ and $p_y = 0.25$ and the IC of the chaotic orbit is $y = -0.1$ and $p_y = 0.1$. We see that the light-blue points form a ring-like shape, the cross-section of the torus on which the regular motion occurs, while the red points are concentrated around some of the regular islands before entering the large chaotic sea of "randomly" distributed points. In Figs. 4.3(b) and (c) we plot the time evolution of the ftmLE, X_1, (2.54) and SALI (2.51) respectively for the two orbits. From these plots we see that both the ftmLE and SALI accurately characterise the chaoticity of each orbit: the regular orbit's ftmLE decreases proportionally to $\ln(t)/t$ and the chaotic one's ftmLE saturates to a positive value [in accordance with (2.55)]; the SALI value of the regular orbit remains constant, and for the chaotic orbit the SALI decreases at an exponential rate [see (2.52)]. Furthermore, in Figs. 4.3(d)-(f) the time evolutions of respectively, the $\log_{10} D_L^1$, $\log_{10} R_L^1$ and, $\log_{10} S_L^1$ values are shown for these two orbits. For these results, we set the grid spacing to $\sigma = 10^{-3}$ and compute the indicators along the y direction. Our results show that, initially, the index values for the regular and chaotic orbit are more or less of similar orders of magnitude, but as the exponential divergence of the chaotic orbit makes itself apparent, a large gap is seen to separate the indicators of these orbits. We are able to distinguish between the regular and chaotic orbits based on the results of the three LDs-based diagnostics, after approximately $\tau = 100$, a comparable integration time to when the ftmLE and SALI are able to identify the orbits' chaoticity, when the difference in magnitude of the two chaos indicators for the regular and chaotic orbit becomes noticeable. Let us note that the results of the D_L^n, R_L^n, and S_L^n methods are similar for greater values of n, with a large, constant difference in the indicator values of the regular and chaotic orbits existing at later times.

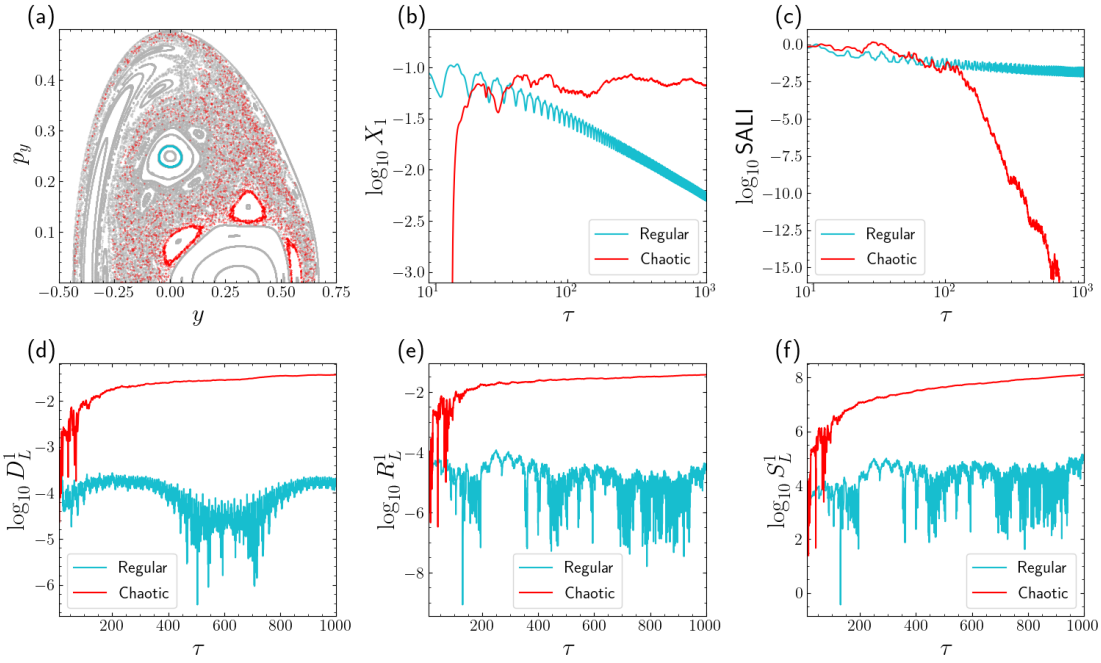

Figure 4.3: (a) The PSS of the Hénon-Heiles system (2.16) at $H = 1/8$ on the cross-section $x = 0$, $p_x > 0$. The intersection points of a regular orbit on this cross-section with IC $y = 0.05$ and $p_y = 0.25$ are shown as blue dots, and the consequents of a chaotic orbit with IC $y = -0.1$ and $p_y = 0.1$ are indicated by red dots. To show the structure of the phase space, the intersections of various other orbits are shown in grey. The time-evolution of the $\log_{10} X_1$ (b), $\log_{10}$ SALI (c), $\log_{10} D_L^1$ (d), $\log_{10} R_L^1$ (e), and $\log_{10} S_L^1$ (f) for the regular and chaotic orbit from (a) for $\tau = 1,000$. The D_L^1, R_L^1, and S_L^1 indices are evaluated along the y-direction with $\sigma = 10^{-3}$.

4.1.1 Global dynamics

Let us now test the ability of the LDs-based chaos quantifiers (4.2), (4.3) and (4.4) to correctly characterise orbits as either regular or chaotic for large ensembles of orbits of the Hénon-Heiles system. In particular, we apply the D_L^n, R_L^n, and S_L^n indices to a 2D subspace. From the results of Fig. 2.2 we can see that at an energy of $H = 1/8$, the y, p_y section with $x = 0$ and $p_x > 0$ displays both regular and chaotic motion, so we use this plane to test the indicators. Furthermore, since this subspace is symmetric with respect to the line $p_y = 0$, we restrict our study to the region $p_y \geq 0$ as the other half only gives redundant information.

To calculate the D_L^n, R_L^n, and S_L^n diagnostics, the forward LDs using the "p-norm" definition (2.63), with $p = 0.5$, are computed on a grid of $1,600 \times 800$ evenly spaced ICs on the intervals $y \in [-0.5, 0.75]$ and $p_y \in [0, 0.5]$ for a final

integration time of $\tau = 1,000$. Since we computed the LDs on a 2D plane, the D_L^n, R_L^n, and S_L^n are evaluated for $n = 2$ along the y and p_y directions. Evaluating in these directions makes use of all available LDs on the considered space and does not require the computation of additional LDs with ICs not on the plane under study. In Figs. 4.4(a)-(c) the studied ICs are coloured according to their $\log_{10} D_L^2$, $\log_{10} R_L^2$, and $\log_{10} S_L^2$, values using the colour scale at the top of each panel. From these plots, we identify the regular regions as those with low indicator values (purple regions) and chaotic regions as those corresponding to high indicator values (red and yellow regions). While we see that these indices clearly give a visual description of the chaoticity of the system, we can also use the information from the D_L^2, R_L^2, and S_L^2 indicators to give a quantitative characterisation of the orbits. The distributions of the $\log_{10} D_L^2$, $\log_{10} R_L^2$, and $\log_{10} S_L^2$ values are plotted in Figs. 4.4(d)-(f) respectively. We see that these distributions are bimodal, with two distinct, well-formed peaks. The peak at lower indicator values corresponds to regular orbits, while the peak at higher values corresponds to chaotic orbits. To distinguish between the two types of orbits, we select a threshold value as the index value located at the minimum between the two peaks. The threshold values selected are $\log_{10} D_L^2 = -2.9$, $\log_{10} R_L^2 = -3.4$, and $\log_{10} S_L^2 = 6.5$, and are represented by vertical, red, dashed lines in Figs. 4.4(d)-(f).

Using these thresholds, we characterise orbits below the threshold values as regular and the remaining orbits as chaotic. For us to gain an understanding on how accurately the D_L^n, R_L^n, and S_L^n indicators identify the regular or chaotic nature of orbits, we compare the characterisation made by them to the one obtained by the SALI method at a final integration time of $\tau = 10^4$. Since the SALI of chaotic orbits saturates to 10^{-16}, while that of regular orbits stays at a positive, practically constant value, we use a threshold of SALI $= 10^{-8}$ to discriminate between regular and chaotic orbits. We assume that the SALI accurately identifies the chaoticity of orbits and find that the percentages P_A of correctly characterised orbits for the LDs-based indices are $P_A \approx 91.8\%$ (D_L^2), $P_A \approx 92.3\%$ (R_L^2), and $P_A \approx 94.4\%$ (S_L^2). To further study which ICs were mischaracterised, Figs. 4.4(g)-(i) show the ICs which were incorrectly identified by the D_L^2, R_L^2 and S_L^2 methods respectively. The points which were falsely classified as regular (i.e., according to the SALI these are actually chaotic) are coloured red, while those incorrectly identified as chaotic are coloured light-blue. From Figs. 4.4(g)-(i) we see that all three indicators struggle in correctly characterising orbits on the borders of regular or chaotic regions. This is due to the relatively large grid size used in the calculations of these indices, meaning that for an IC on the edges of regular and chaotic motion, some of the neighbouring ICs we consider in the computation of the LDs-based indicators will have the opposite nature (i.e., if the orbit of an IC is regular/chaotic the nearby ICs may be chaotic/regular).

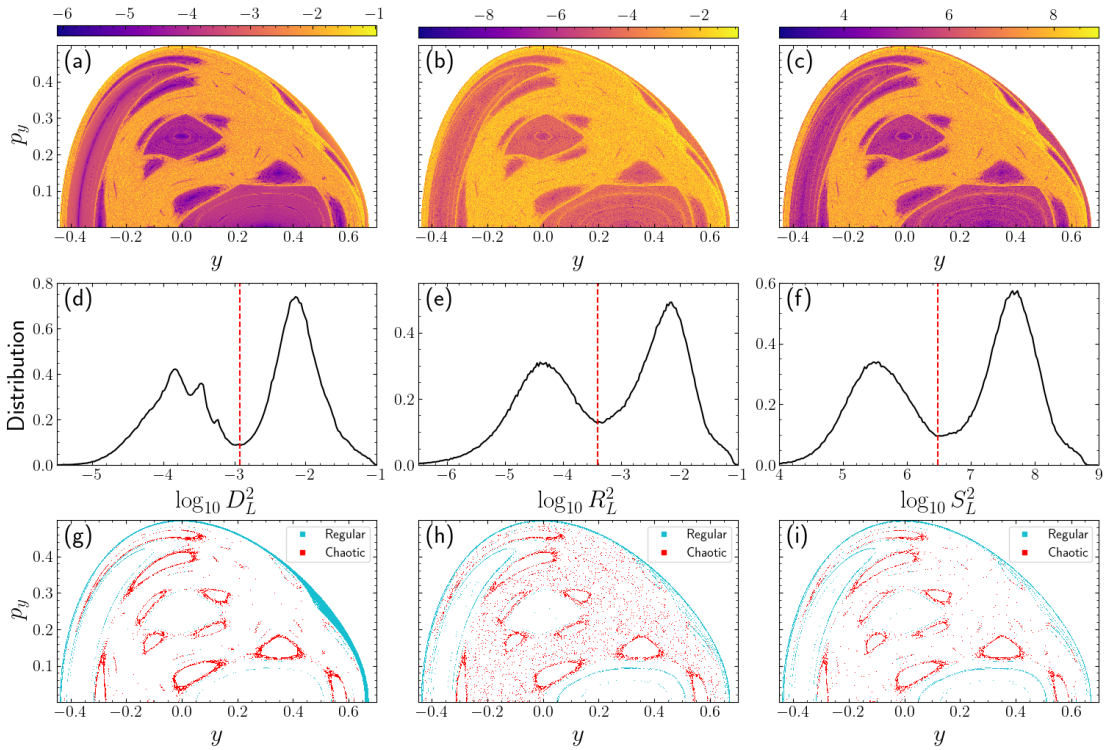

Figure 4.4: The (a) $\log_{10} D_L^2$ (4.2), (b) $\log_{10} R_L^2$ (4.3), and (c) $\log_{10} S_L^2$ (4.4), values after $\tau = 1,000$ for a grid of $1,600 \times 800$ evenly distributed ICs of the Hénon-Heiles system (2.16) on the intervals $y \in [-0.5, 0.75]$ and $p_y \in [0, 0.5]$ with $x = 0$ fixed and $p_x > 0$ computed from the Hamiltonian function. The ICs are coloured according to the colour scale at the top of each panel. Normalised distributions of the $\log_{10} D_L^2$ (d), $\log_{10} R_L^2$ (e), and $\log_{10} S_L^2$ (f) values of the orbits considered in (a)-(c). The values $\log_{10} D_L^2 = -2.9$, $\log_{10} R_L^2 = -3.4$ and $\log_{10} S_L^2 = 6.5$ are denoted by a red, dashed line as appropriate threshold values discriminating between regular and chaotic orbits. The set of ICs of the system which are incorrectly characterised by the (g) D_L^2, (h) R_L^2, and (i) S_L^2 indices, according to the classification obtained by the SALI method computed for $\tau = 10^4$ forward iterations. Light-blue points correspond to regular orbits which are falsely identified as chaotic, and red points to chaotic orbits which are incorrectly identified as regular.

Further inspection shows that the D_L^2 index [Fig. 4.4(g)] has more incorrectly characterised points on the edges of regular islands, as well as falsely identified the points on the border of the phase space. The R_L^2 indicator classifies better the points at which the D_L^2 method fails to classify correctly, but has the drawback of characterising more points in the chaotic seas incorrectly [see the red points in the chaotic sea shown in Fig. 4.4(g)]. The S_L^2 quantifier seems to be in the middle ground of the other two indices, identifying the orbits on the boundaries of the energetically allowed space and distinct regular and chaotic regions better than the D_L^2 index, but characterising more points in the chaotic sea incorrectly. From the analysis of which points are mischaracterised, we conclude that the D_L^n method will have a better performance than the other indicators in systems with a large degree of chaos and fewer regular regions, while the R_L^n has the advantage in regions with a more confined chaotic sea and more regular regions.

While the D_L^2, R_L^2, and S_L^2 indices are not as accurate in characterising orbits as the SALI, they require less computational time to compute and are easier to implement. We note that for the computation of the SALI, knowledge of both the equations of motion and the variational equations is required. For computation of the LDs-based chaos indicators, on the other hand, only the equations of motion of the system are necessary. This makes the LDs-based indicators easier to implement, especially in systems where finding an analytical expression for the variational equations is not straightforward. Furthermore, since the SALI requires the calculation of two deviation vectors, the D_L^2, R_L^2, and S_L^2 methods are, in general, computed considerably faster than the SALI for the same integration time. While the LDs-based chaos detection methods do not provide a perfect characterisation of the chaoticity of the system, they do offer a wealth of information without too much effort and in quick time.

4.1.2 Factors influencing the performance of the LDs-based chaos diagnostics

Let us now discuss the effect of the total integration time τ, grid spacing σ, and the system's chaoticity on the performance of the LDs-based chaos indicators. In Figs. 4.5(a)-(c) we plot the normalised distributions of the $\log_{10} D_L^2$ (4.2), $\log_{10} R_L^2$ (4.3), and $\log_{10} S_L^2$ (4.4) values respectively, for the set of ICs considered in Fig. 4.4 for three different final integration times $\tau = 100$, 500, and $1,000$. Similarly, in Figs. 4.5(d)-(f) the normalised distributions of the index values at $\tau = 1,000$ are plotted for ICs on the same subspace as Figs. 4.5(a)-(c) but for three grid spacings, $\sigma = 2 \times 10^{-3}$, 1×10^{-3}, and 5×10^{-4}. The threshold values used to distinguish between regular and chaotic motion are indicated by the dashed, vertical lines coloured according to the corresponding distribution. We note that the position of

the distributions for the D_L^2 and R_L^2 indices, and therefore threshold values, does not vary greatly with respect to either parameter, while the position of the S_L^2 distribution shifts to greater values for an increased integration time and decreased grid spacing. Furthermore, we see that each distribution displays two distinct peaks, the peak at lower index values consisting of the ICs of regular orbits, while that at higher values is composed of the chaotic orbits. As the integration time is increased, or the grid spacing decreased, we see the peaks growing more distinct. Since more distinct peaks means that we can choose an appropriate threshold value more accurately, we conclude that the indices will be more accurate in categorising the nature of orbits at higher integration times and lower grid spacings.

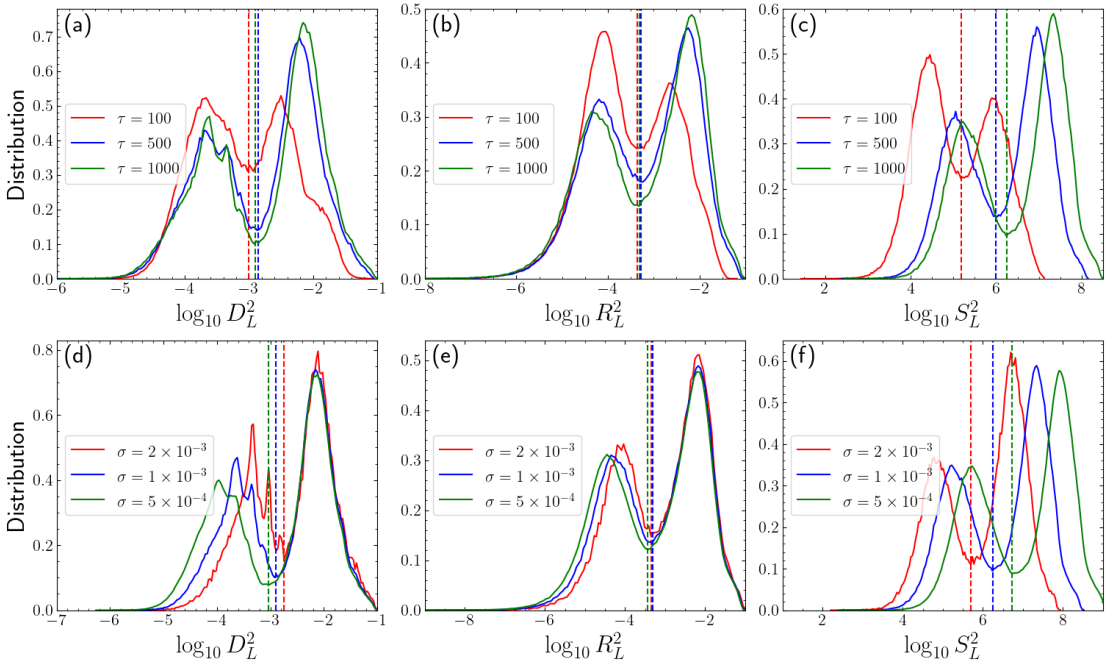

Figure 4.5: Results obtained for orbits having their ICs on the same subspace as Fig. 4.4. The normalised distributions of the $\log_{10} D_L^2$ (a), $\log_{10} R_L^2$ (b), and $\log_{10} S_L^2$ (c) for fixed $\sigma = 10^{-3}$ and three different final integration times of $\tau = 100$, 500 and 1,000. (d)-(f) the same as (a)-(c) but the total integration time is kept fixed at $\tau = 1,000$ and instead σ is varied to $\sigma = 2 \times 10^{-3}$, 1×10^{-3}, and 5×10^{-4}. The threshold value of each distribution is shown as a dashed, vertical line in the same colour as the corresponding distribution.

We next investigate how the change in the parameters used to compute the three indices affects the accuracy of the categorisation made. In Figs. 4.6(a)-(c) we show the percentage of orbits correctly characterised, P_A, when compared to

the categorisation made by the SALI evaluated at a time of $\tau = 1,000$, by the D_L^2, R_L^2, and S_L^2 indices respectively for ten different final integration times. The ICs of the orbits are on the subspace considered in Fig. 4.4 and are evenly distributed on the intervals $y \in [-0.5, 0.75]$, $p_y \in [0, 0.5]$ with four different grid spacings σ being considered. From the results in this plot, we see that for all indicators there is an initial increase in the accuracy as the integration time is increased, which starts levelling out at later times. The initial increase is due to the more chaotic orbits being accurately detected, as the exponential divergence of nearby orbits makes itself apparent and the LD values in the chaotic regions start behaving erratically [as we see in Fig. 4.1(c)]. As the majority of chaotic orbits are correctly characterised, the P_A starts levelling out. Furthermore, we see that the amount of correctly identified orbits is greater for a smaller grid spacing at almost all times. This is to be expected, as for smaller σ the indicators gain more accurate information about the behaviour of orbits close to the IC under consideration. For orbits on the borders of regular regions, which we noticed that the indicators struggle to identify accurately [Figs. 4.4(g)-(i)], a more accurate identification can therefore be made by decreasing σ. The drawback of decreasing σ is that the CPU time required to calculate the necessary LDs increases rapidly. If we consider computing the D_L^n, R_L^n, and S_L^n indices for $n = 2$ and reduce σ by a factor of 10, the CPU time required to compute the grid points will increase by a factor of 100. When computing the LDs-based chaos detection methods, the gain in accuracy has to be practically weighed with the amount of CPU time available for the computations, but we note that for early times and not too small grid sizes the indicators are able to achieve an accurate identification of orbits [see in Figs. 4.6(a) and (c) the P_A of the D_L^2 and S_L^2 indices at $\tau = 400$ and $\sigma = 1 \times 10^{-3}$]. We note that the increase in accuracy as the parameters change are what we expected from our discussion related to Fig. 4.5.

To further investigate the effect of the amount of regular and chaotic regions, also referred to the chaoticity of a system, on the accuracy of the D_L^n, R_L^n, and S_L^n, we consider the Hénon-Heiles system (2.16) at energies $H = 1/6$ and $1/9$. The PSS of the system at $H = 1/6$ on the cross-section $x = 0$, $p_x > 0$ is shown in Fig. 4.7(a). We clearly see that at this energy there are far more chaotic and less regular orbits, than at $H = 1/8$ (Fig. 4.4). The total percentage of chaotic orbits P_C of this PSS is $P_C \approx 96.7\%$, as categorised by the SALI at an integration time of $\tau = 10^4$. In order to have a global description of the dynamics, we calculate the LDs on a grid of $1,600 \times 800$ evenly spaced ICs on the intervals $y \in [-0.5, 1]$ and $p_y \in [0, 0.6]$ for a final integration time of $\tau = 1,000$. From these computed LDs, the D_L^2, R_L^2, and S_L^2 indices are calculated and appropriate threshold values for each indicator are selected from the distribution of their values. Comparing the characterisation made by the D_L^2, R_L^2, and S_L^2 methods to the ones made by the

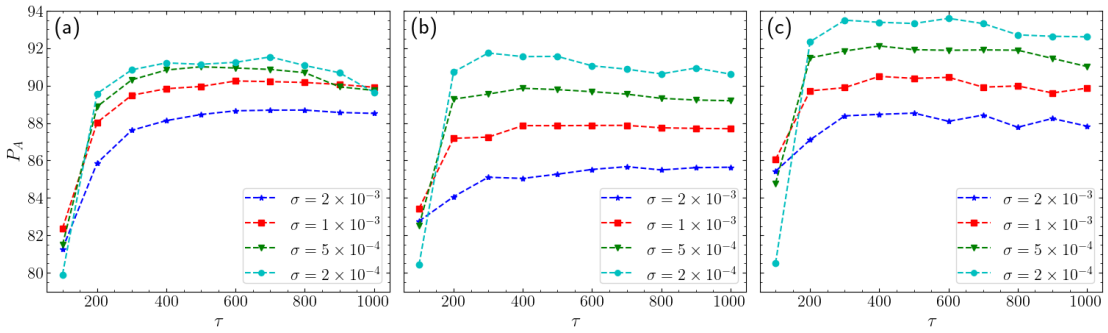

Figure 4.6: The percentage of correctly characterised orbits P_A when compared with the classification obtained by the SALI evaluated at $\tau = 1,000$ of the D_L^2 (a), R_L^2 (b), and S_L^2 (c) for a total of ten different final times τ and four different grid spacings σ. The ICs were computed for the same subspace of the Hénon-Heiles system (2.16) as in Fig. 4.4, with the total number of ICs corresponding to an evenly distributed grid using the appropriate grid spacing.

SALI on the same grid of ICs for the final integration time of $\tau = 10^4$, we find that $P_A \approx 99.4\%$, $P_A \approx 97.9\%$, and $P_A \approx 98.2\%$ of the studied orbits are categorised correctly by the D_L^2, R_L^2, and S_L^2 indicators respectively. In Figs. 4.7(b)-(d) the points incorrectly characterised by the three indices are shown, with the points misidentified as regular or chaotic coloured red or light-blue respectively. As we expected from our discussion in Section 4.1.1, the D_L^2 method [Fig. 4.7(b)] is the most accurate of the three indicators at classifying the orbits of highly chaotic systems, with the majority of incorrectly identified ICs stemming from the edges of the few regular regions. The R_L^2 technique [Fig. 4.7(b)] categorises a large number of ICs in the chaotic sea incorrectly, a drawback for a system with such a large chaotic area.

The PSS of the Hénon-Heiles system at $H = 1/9$ for $x = 0$, $p_x > 0$ is shown in Fig. 4.7(e). At this energy, there are fewer chaotic orbits, with the regular islands seen at $H = 1/8$ increasing in size. We find that at $\tau = 10^4$ the SALI characterises this PSS to consist of $P_C \approx 30.9\%$ chaotic orbits, significantly less than the previous two cases. The LDs are calculated on a grid of $1,600 \times 800$ evenly spaced ICs on the intervals $y \in [-0.5, 0.75]$ and $p_y \in [0, 0.5]$ for a final integration time of $\tau = 1,000$ and the D_L^2, R_L^2, and S_L^2 indices are computed on this grid. The ICs which the three indicators do not identify correctly are shown in Figs. 4.7(f)-(h) using the same colouring scheme as that of Figs. 4.4(g)-(i) and Figs. 4.7(b)-(d). We find that $P_A \approx 85.4\%$, $P_A \approx 88.5\%$, and $P_A \approx 88.5\%$ for the D_L^2, R_L^2, and S_L^2 indicators respectively. The accuracy of the methods is clearly far lower than in the previous two cases, due to the large number of

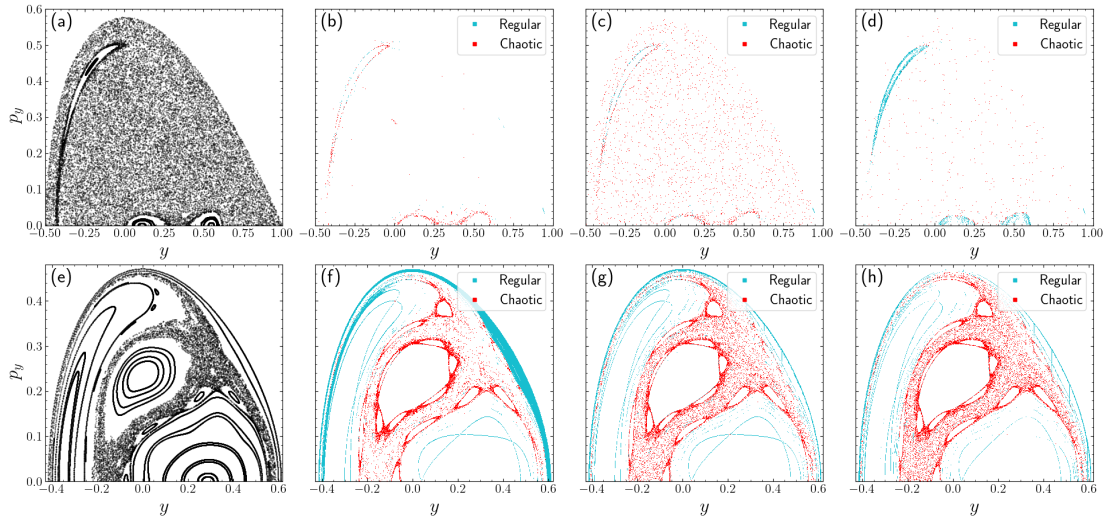

Figure 4.7: (a) The PSS of the Hénon-Heiles system (2.16) at $H = 1/6$ defined by $x = 0$, $p_x > 0$. (b)-(d) The points incorrectly characterised by the D_L^2 (b), R_L^2 (c), and S_L^2 (d) indices on the PSS from (a) at $\tau = 1,000$. The ICs of these points are on an $1,600 \times 800$ evenly spaced grid on the intervals $y \in [-0.5, 1]$ and $p_y \in [0, 0.6]$. (e) The same as (a) but for $H = 1/9$. (f)-(h) shows the points incorrectly characterised by the D_L^2 (f), R_L^2 (g), and S_L^2 (h) indicators for the PSS from (e). The ICs of these points are on a $1,600 \times 800$ evenly spaced grid on the intervals $y \in [-0.5, 0.75]$ and $p_y \in [0, 0.5]$. In (b)-(d) and (f)-(h), the points incorrectly characterised as chaotic, but which the SALI at $\tau = 10^4$ identifies as regular, are coloured light-blue, while those incorrectly characterised as regular are coloured red.

regular islands, at the edges of which the indices fail to characterise orbits correctly. The R_L^2 index clearly performs better than the D_L^2 indicator for this energy, with the D_L^2 method incorrectly identifying large regular regions on the edges of the energetically permissible phase space. From Fig. 4.7(g) it can be seen that the R_L^2 method once again characterises some ICs in the chaotic sea incorrectly, but due to the smaller chaotic sea, this does not have a great effect on the overall achieved accuracy. The R_L^2 and S_L^2 indices [Figs. 4.7(g) and (h) respectively] perform similarly, with the incorrectly characterised points stemming from the chaotic sea and the edges of regular islands.

4.2 Investigating the chaotic dynamics of the 2D standard map by the LDs-based chaos diagnostics

After showing how the D_L^2, R_L^2 and S_L^2 diagnostics can characterise orbits of a low-dimensional, conservative, continuous system, using the Hénon-Heiles model as a test case, we now investigate their performance in studying the chaoticity of low-dimensional symplectic maps. As an example case of a low-dimensional, symplectic map, we consider the 2D standard map (2.57).

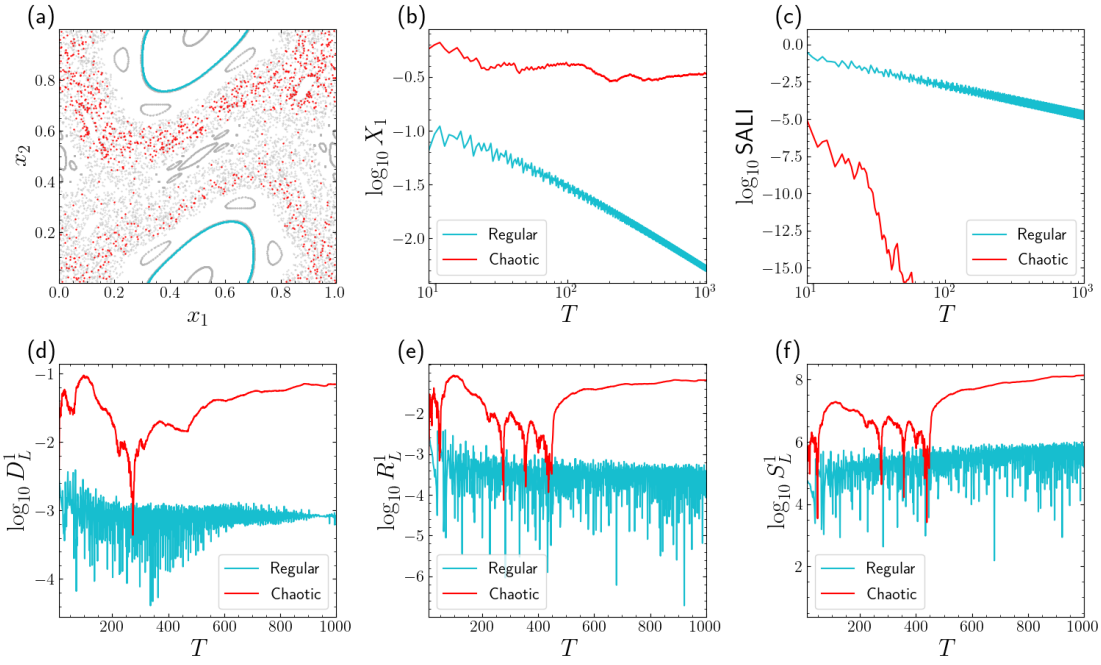

Figure 4.8: (a) The evolution of a regular (light-blue) and chaotic (red) orbit of the 2D standard map (2.57) with $K = 1.5$ for $T = 1,000$ forward iterations. Grey points correspond to the evolution of various other orbits. The IC of the regular orbit is $(x_1, x_2) = (0.7, 0.1)$ and that of the chaotic orbit is $(x_1, x_2) = (0.2, 0.2)$. The time-evolution of the $\log_{10} X_1$ (b), $\log_{10}$ SALI (c), $\log_{10} D_L^1$ (d), $\log_{10} R_L^1$ (e), and $\log_{10} S_L^1$ (f) for the regular and chaotic orbits from (a). The D_L^1, R_L^1, and S_L^1 indices are evaluated along the x_1 direction of the map with grid spacing $\sigma = 10^{-3}$.

Let us begin by studying the behaviour of the indicators for individual orbits of this map (2.57). In Fig. 4.8(a), the evolution of a regular orbit (light-blue) with IC $(x_1, x_2) = (0.7, 0.1)$ and a chaotic orbit (red) with IC $(x_1, x_2) = (0.2, 0.2)$ of the map (2.57) with $K = 1.5$ is shown for $T = 1,000$ forward iterations. The

regular orbit forms a ring [recall from Section 2.3.5 that the coordinates of the 2D map (2.57) are mod 1, so the opposite sides of the plot join together to form a torus] while the points of the chaotic orbit are scattered "randomly" in the phase space. The time evolution of the ftmLE, X_1, and SALI for the two orbits are shown in Figs. 4.8(b) and (c) respectively. From these figures, we see that the mLCE estimator and SALI behave as expected for 2D systems, following the laws provided in (2.55) and (2.53). More specifically, we see that for the regular orbit, the ftmLE and SALI values decrease proportionally to $\ln(T)/T$ and $1/T^2$ respectively, while for the chaotic orbit, X_1 saturates to a positive constant and the SALI decreases at an exponential rate. In Figs. 4.8(d)-(f) the time evolution of the $\log_{10} D_L^1$, $\log_{10} R_L^1$, and $\log_{10} S_L^1$ values are shown respectively. These indices are evaluated along the x_1 direction of the map with $\sigma = 10^{-3}$. It takes longer than the case of the Hénon-Heiles system [Figs. 4.3(d)-(f)] for there to be a noticeable difference between the LDs-based indicator values of the regular and chaotic orbits, but after about $T = 500$ iterations one can clearly distinguish between them, as the index values of the chaotic trajectory are approximately two orders of magnitude larger than those of the regular one.

4.2.1 Global dynamics

In order to demonstrate the ability of the LDs-based chaos indices to study the dynamics of the 2D map (2.57), we compute the LDs on a grid of $1,000 \times 1,000$ ICs on the intervals $x_1, x_2 \in [0, 1)$ with $K = 1.5$, for a total of $T = 1,000$ forward iterations. In Figs. 4.9(a)-(c) these ICs are coloured according to their $\log_{10} D_L^2$, $\log_{10} R_L^2$ and $\log_{10} S_L^2$ values respectively, using the colour scale at the top of each panel. We see, from a visual inspection of these plots, that the regular (chaotic) regions correspond to areas of low (high) indicator values. To identify the threshold for each indicator, which will allow for the characterisation of regular and chaotic orbits, the distributions of the $\log_{10} D_L^2$, $\log_{10} R_L^2$, and $\log_{10} S_L^2$ values are plotted in Figs. 4.9(d)-(f) respectively. From these distributions, the thresholds are selected as the minimum between the two peaks at $\log_{10} D_L^2 = -2.3$, $\log_{10} R_L^2 = -3.1$, and $\log_{10} S_L^2 = 6.5$ [the locations of these values are shown as red, dashed lines in Figs. 4.9(d)-(f)].

To gain an understanding of how accurately the D_L^2, R_L^2, and S_L^2 diagnostics identify orbits as regular or chaotic, we compare the characterisation made by these indicators to that made by the SALI at $T = 10^4$. Let us recall that the SALI of regular orbits in 2D systems tends to zero at a linear rate (Section 2.3.4). For a total of $T = 10^4$ iterations, the SALI of the regular orbits will however still be above SALI $= 10^{-12}$, while the SALI values of chaotic orbits are at the order of 10^{-16}. Thus, we select SALI $= 10^{-12}$ as such a threshold and find that the D_L^2, R_L^2, and S_L^2 methods correctly identify $P_A \approx 96.7\%$, $P_A \approx 95.2\%$, and

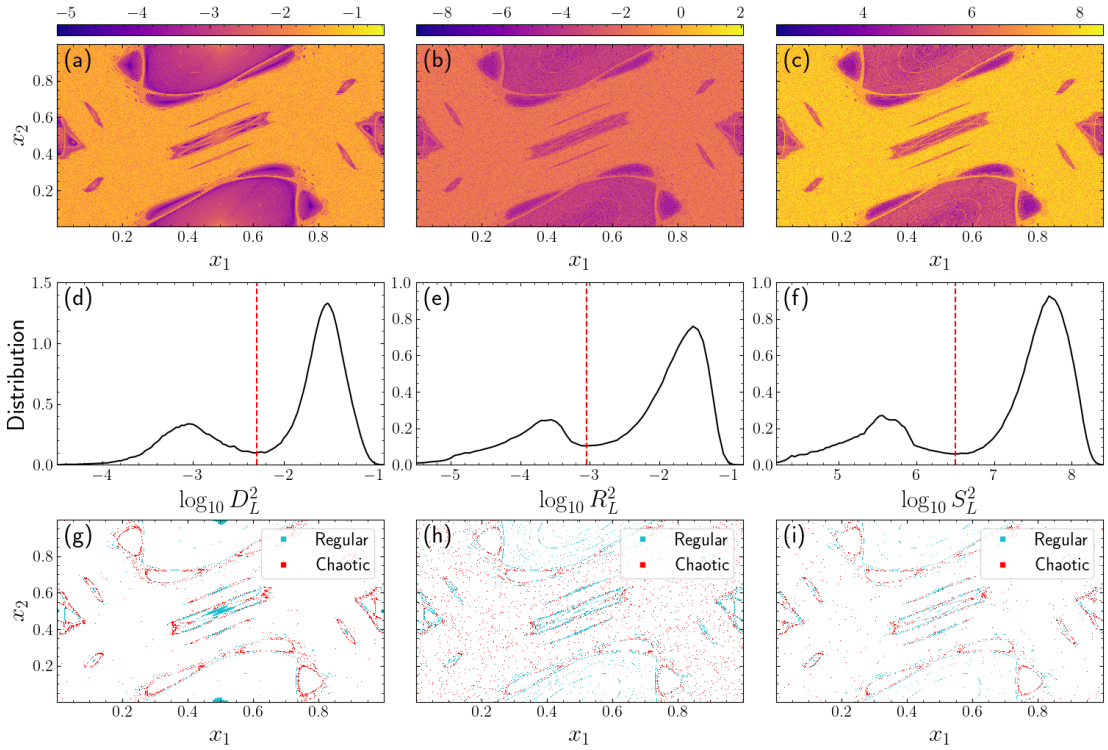

Figure 4.9: Results obtained for orbits of the 2D standard map (2.57) for $K = 1.5$ with ICs evenly distributed on a $1,000 \times 1,000$ grid on the intervals $x_1, x_2 \in [0, 1)$. The ICs are coloured according to their (a) $\log_{10} D_L^2$ (4.2), (b) $\log_{10} R_L^2$ (4.3), and (c) $\log_{10} S_L^2$ (4.4) values after $T = 1,000$ forward iterations using the colour scale at the top of each panel. (d)-(f) The normalised distributions of the $\log_{10} D_L^2$, $\log_{10} R_L^2$, and $\log_{10} S_L^2$ values of the orbits considered in (a)-(c) respectively. The values $\log_{10} D_L^2 = -2.3$, $\log_{10} R_L^2 = -3.1$, and $\log_{10} S_L^2 = 6.5$ are denoted by a red, dashed line to indicate the threshold values of the indices. The set of ICs of the system which are incorrectly characterised by the (g) D_L^2, (h) R_L^2 and (i) S_L^2 index, with respect to the classification obtained by the SALI method computed for $T = 10^4$ forward iterations. Light-blue points correspond to regular orbits which are falsely identified as chaotic and red points to chaotic orbits which are incorrectly identified as regular.

$P_A \approx 97.3\%$ of the ICs respectively. The ICs of the incorrectly characterised orbits are shown in Figs. 4.9(g)-(i) using the same colouring scheme as that of Figs. 4.4(g)-(i). From Figs. 4.9(g)-(i) we can once again retrieve the following general trends: the D_L^2 index fails to identify ICs at the edges of regular regions, the R_L^2 indicator incorrectly characterises more orbits in the chaotic sea, and the S_L^2 diagnostic shows neither of these pronounced drawbacks. Despite these outlined shortcomings, all three indicators give a highly accurate characterisation of the orbits, in general agreeing with the SALI for $\gtrsim 95\%$ of cases. Furthermore, since the LDs-based chaos diagnostics require neither the evaluation of the tangent map nor the computation of the deviation vectors, they are calculated significantly faster than the SALI.

4.2.2 Factors influencing the performance of the LDs-based chaos diagnostics

Let us now discuss the effect of the total number of map iterations T and grid spacing σ on the performance of the LDs-based indicators. In Figs. 4.10(a)-(c) the distributions of the D_L^2, R_L^2, and S_L^2 indices for the 2D map (2.57) with $K = 1.5$, for fixed grid size of $\sigma = 10^{-3}$ on the intervals $x_1, x_2 \in [0, 1)$ for three different final iteration numbers, $T = 100$, 500 and $1,000$, are shown. Appropriate threshold values are selected for each distribution and plotted as vertical dashed lines in the same colour as the corresponding distribution. The change in the distributions due to the dependence on the total number of iterations is similar to what we saw in the case of the Hénon-Heiles system [Figs. 4.5(a)-(c)]. We clearly see that the distributions at each T display the same general shape, with distinct peaks corresponding to the index values of regular and chaotic orbits (lower and higher indicator magnitudes respectively). A slight shift to the left is seen in the distributions of the D_L^2 and R_L^2 values as T is increased, while the S_L^2 index distribution shifts further to the right. In general, the distance between the regular and chaotic peaks grows larger as the number of iterations is increased. The larger separation between the two peaks would suggest that at later times the indicators are more accurate, since there exist fewer orbits of which one is uncertain on how to characterise (as discussed in Section 4.1.2). While most of the threshold values for the D_L^2 and R_L^2 indices are close, for the best characterisation of the orbits the distributions should be plotted and the threshold selected from them.

In Figs. 4.10(d)-(f) we show the distributions of the D_L^2, R_L^2, and S_L^2 values for the 2D map with $K = 1.5$ for a fixed number of total iterations $T = 1,000$, for three different grid spacings of $\sigma = 10^{-3}$, 5×10^{-4}, and 2×10^{-4} on the intervals $x_1, x_2 \in [0, 1)$. We see that the peak in the distribution at high indicator values of the D_L^2 and R_L^2 indices appear identical for each σ, while the position of the peak at

lower values shifts further to the left for decreasing σ. For the S_L^2 indicator, there is a large shift to greater values as σ is decreased, with the threshold values shifting accordingly. Because the extent of the gap between peaks grows as σ is decreased, we are able to pick a more accurate threshold value. From this analysis we draw the same conclusions as we did when investigating the Hénon-Heiles system: a decrease in σ will result in a better classification of the orbits [see Figs. 4.5(d)-(f) and the related discussion].

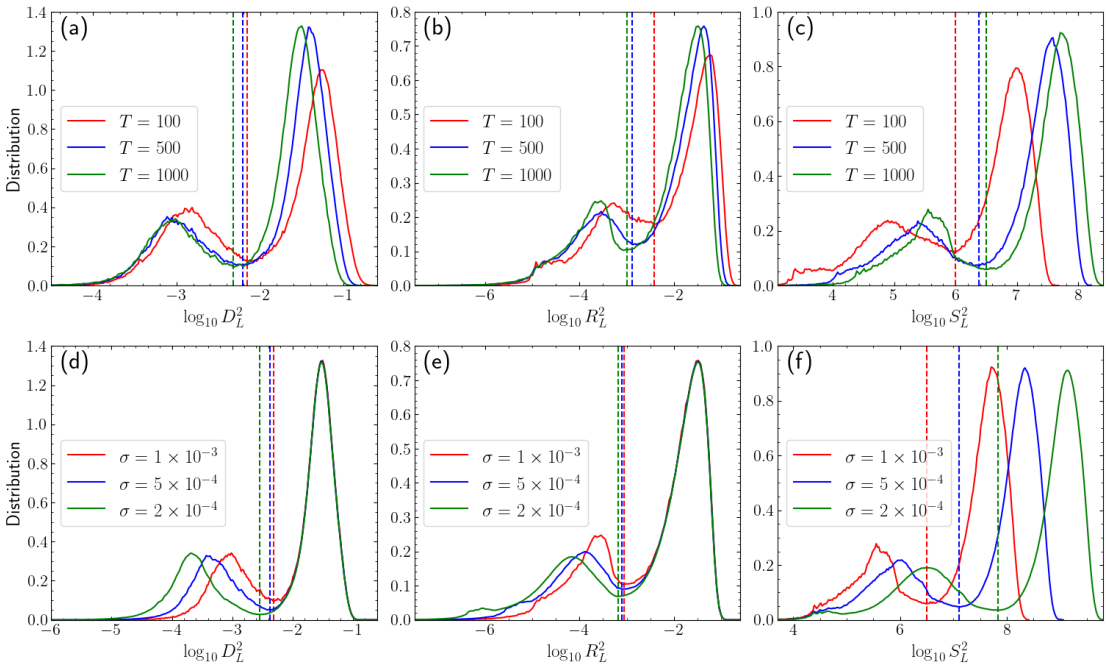

Figure 4.10: (a)-(c) The normalised distributions of the $\log_{10} D_L^2$ (a), $\log_{10} R_L^2$ (b) and $\log_{10} S_L^2$ (c) for the 2D map (2.57) with $K = 1.5$ for a fixed $\sigma = 10^{-3}$ and three different total iterations of $T = 100$, 500 and 1,000. (d)-(f) the same as (a)-(c) but the number of total iterations is kept fixed at $T = 1,000$ and instead σ is varied to $\sigma = 1 \times 10^{-3}$, 5×10^{-4}, and 2×10^{-4}. The threshold value of each distribution is shown as a dashed, vertical line in the same colour as the corresponding distribution.

Let us now investigate the effect of the total number of iterations and grid spacings on the accuracy of the D_L^2, R_L^2 and S_L^2 diagnostics in identifying regular and chaotic orbits. To study the dependence of the percentage of correctly categorised ICs, P_A, on these variables, we compute the D_L^2, R_L^2, and S_L^2 indices for the 2D map (2.57) at $K = 1.5$ for ten different final iterations and four different grid spacings (giving a total of 40 different cases). For each case, we select an appropriate threshold for separating regular and chaotic orbits from the corresponding

distributions, and compare the characterisation of the orbits made by the three indicators to that obtained by the SALI values computed for $T = 10^4$. Figures 4.11(a)-(c) show the P_A acquired by the D_L^2, R_L^2, and S_L^2 indices respectively, for the ten different T and four different σ values. From the result of Fig. 4.11 we see, in general, similar results to those in Fig. 4.6, with the accuracy increasing as T is initially increased and σ is decreased. We note, following our discussion in Section 4.1.2, that these effects are due to the chaotic nature of orbits being accurately revealed at later times and that closer ICs are taken into account when considering a smaller grid spacing. Unlike the results of Fig. 4.6, in Fig. 4.11 we see that at higher grid spacings, the indicators start falsely identifying more orbits for very large T [for example in Fig. 4.11(a) the P_A of the D_L^2 for $\sigma = 2 \times 10^{-3}$ at $\log_{10} T = 4$ is noticeably greater than at $\log_{10} T = 4.5$]. The LDs-based chaos diagnostics do however, generally, identify the large majority of orbits considered in Fig. 4.11 correctly, demonstrating their ability to characterise chaos in the 2D map for a variety of different parameters.

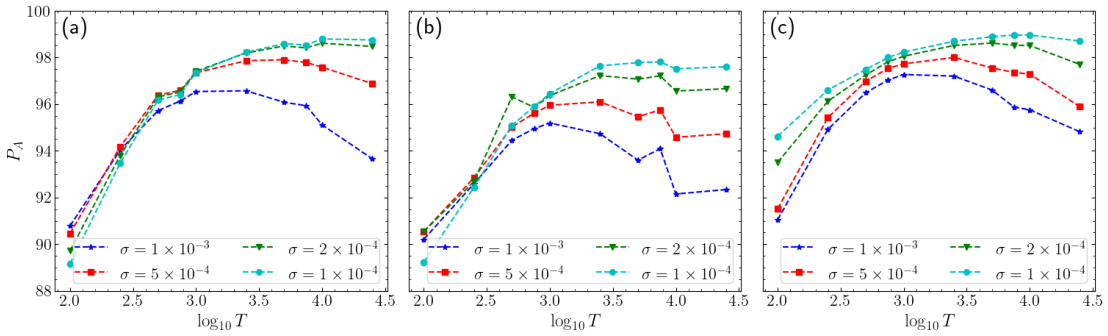

Figure 4.11: The percentage of correctly characterised orbits P_A when compared with the classification obtained by the SALI evaluated at $T = 10^4$ of the D_L^2 (a), R_L^2 (b), and S_L^2 (c) indices for a total of ten different final forward iterations T of the map and four different grid spacings σ. ICs were computed for the 2D standard (2.57) map with $K = 1.5$ on the intervals $x_1, x_2 \in [0, 1)$, with the total number of ICs corresponding to an evenly distributed grid on these intervals using the appropriate grid spacing.

Let us now discuss in more detail how the chaoticity affects the performance of the indicators for the 2D standard map (2.57). The parameter K controls the degree and magnitude of the chaoticity for this model, so since we have already performed a thorough analysis of the dynamics for $K = 1.5$ (a relatively high value), we now study the performance of the three indices for $K = 0.75$ and $K = 1.1$. For both cases the considered grid spacing is kept fixed at $\sigma = 5 \times 10^{-4}$ on the intervals $x_1, x_2 \in [0, 1)$ (as K decreases, the phase space area covered by regular regions will increase, so a low σ is favourable) and the accuracy of the

characterisation obtained by the LDs-based indices at ten different total iterations, compared to that achieved by the SALI evaluated at $T = 10^4$. In Figs. 4.12(a)-(b) we show the grid of $2,000 \times 2,000$ ICs (corresponding to $\sigma = 5 \times 10^{-4}$) coloured according to their $\log_{10}$ SALI value at $T = 10^4$ for $K = 0.75$ and $K = 1.1$ respectively. From Fig. 4.12(a) we see that for $K = 0.75$, the phase space consists of large regular regions (dark purple) with thin strips of chaos (orange) in-between them. For the case of $K = 1.1$, considerably more chaos is detected, with it occurring in large chaotic seas containing a variety of regular islands. The SALI characterises the system to be comprised of $P_C \approx 13.0\%$ and $P_C \approx 57.0\%$ chaotic orbits at $T = 10^4$ for $K = 0.75$ and $K = 1.1$ respectively. We note that for the previously considered case of $K = 1.5$ in Fig. 4.11, the system consists of $P_C \approx 72.0\%$ chaotic orbits.

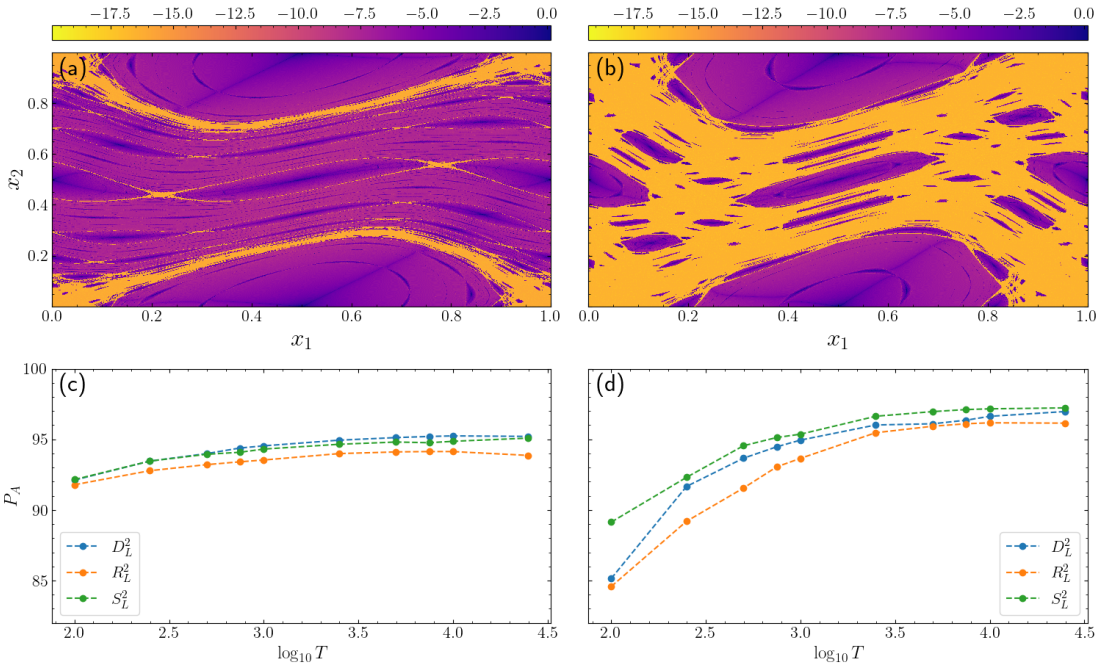

Figure 4.12: (a) A grid of $2,000 \times 2,000$ evenly spaced ICs on the intervals $x_1, x_2 \in [0, 1)$ of the 2D standard (2.57) for $K = 0.75$ coloured according to their $\log_{10}$ SALI values, after a total number of $T = 10^4$ iterations, using the colour scale on top of each panel. (b) The same as (a) but for $K = 1.1$. (c) The percentage accuracy P_A of the D_L^2, R_L^2, and S_L^2 indices for the ICs of (a) for ten different T (the P_A is calculated by comparing the characterisation obtained by the LDs-based indicators to that made by the SALI at $T = 10^4$). (d) the same as (c) except for the ICs considered in (b).

In Figs. 4.12(c) and (d) the total percentage of correctly identified orbits P_A

is shown for the D_L^2, R_L^2, and S_L^2 indices for the map with $K = 0.75$ and $K = 1.1$ respectively. For both cases considered, the indicators accurately identify chaos, with $P_A \gtrsim 90\%$ for most of the cases. Since, of course, there only exist $P_C \approx 13.0\%$ of chaotic orbits for $K = 0.75$, this could still mean a large number of these orbits are incorrectly identified, especially those in the very thin chaotic strips in the middle of the plot. While for $K = 0.75$ the P_A is approximately constant for all T values, for $K = 1.1$ the P_A increases until levelling off at later times. For both cases, the behaviour of the three different indicators is very similar, with there only being at most a difference in accuracy of $P_A \approx 1\%$. Unlike the case of $K = 1.5$ (Fig. 4.11) there is no decrease in accuracy of the indices at later times.

4.3 Investigating the dynamics of a 4D symplectic map

Thus far, we have only discussed the implementation of the D_L^n, R_L^n, and S_L^n indices for low-dimensional dynamical systems. In higher-dimensional models, due to the difficulty in obtaining a qualitative visualisation of the dynamics, quantifying chaos accurately becomes extremely important. To demonstrate the ability of the D_L^n, R_L^n, and S_L^n indicators to characterise chaos in higher dimensions, as well as study the effect of the order n on the performance of these indicators, the 4D standard map [6] is used as a prototypical model of a conservative, higher-dimensional system. The 4D standard map is composed of two coupled 2D standard maps and is given by

$$\begin{aligned} x_1' &= x_1 + x_2' \\ x_2' &= x_2 + \frac{K}{2\pi}\sin(2\pi x_1) - \frac{B}{2\pi}\sin[2\pi(x_3 - x_1)] \\ x_3' &= x_3 + x_4' \\ x_4' &= x_4 + \frac{K}{2\pi}\sin(2\pi x_3) - \frac{B}{2\pi}\sin[2\pi(x_1 - x_3)] \end{aligned} \quad (\text{mod } 1), \tag{4.5}$$

where K and B are real parameters, K controlling the chaoticity and B the coupling between the two 2D maps.

Let us begin our analysis by evaluating the D_L^n, R_L^n, and S_L^n indices for individual orbits of the 4D map (4.5). We set $K = 1.5$ and $B = 0.08$ and in Fig. 4.13(a) show the evolution of a regular (light-blue) and chaotic (red) orbit, projected on the (x_1, x_2) plane for $T = 1,000$ iterations. Additionally, we show the evolution of various other orbits in grey, to outline the structure of the phase space. The IC of the regular orbit is $(x_1, x_2, x_3, x_4) = (0.6, 0.05, 0.54, 0.01)$ and that of the chaotic orbit is $(x_1, x_2, x_3, x_4) = (0.784, 0.094, 0.54, 0.01)$. We see that the light-blue points

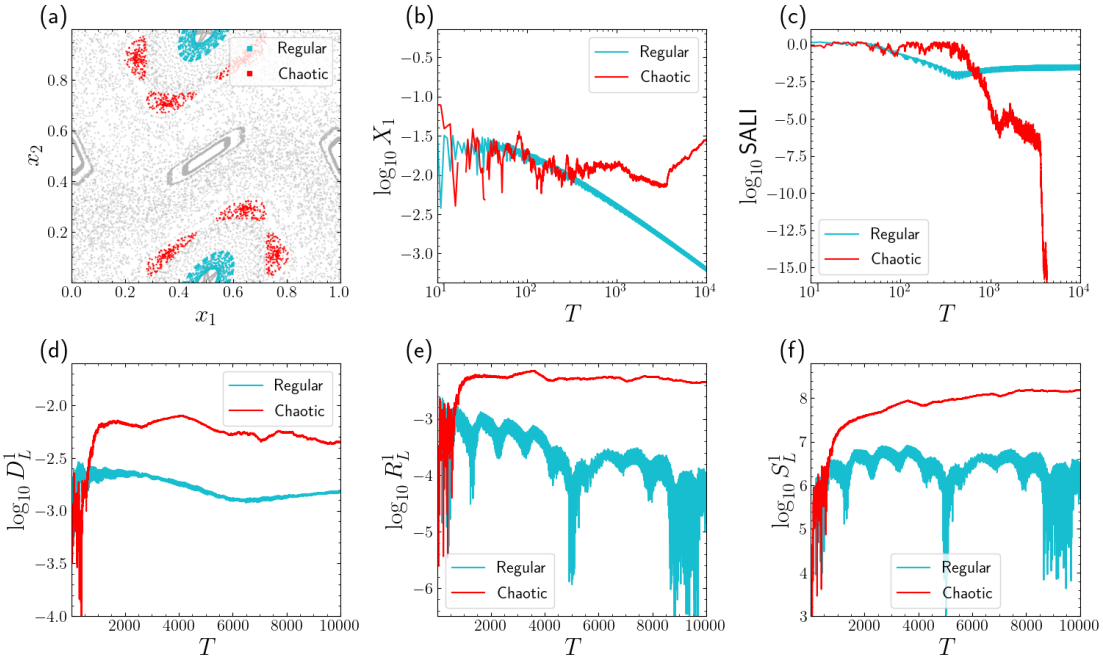

Figure 4.13: (a) The projection of a regular (light-blue) and chaotic (red) orbit of the 4D standard map (4.5) with $K = 1.5$ and $B = 0.08$ on the (x_1, x_2) subspace for $T = 1,000$ forward iterations. The IC of the regular orbit is $(x_1, x_2, x_3, x_4) = (0.6, 0.05, 0.54, 0.01)$ and that of the chaotic orbit is $(x_1, x_2, x_3, x_4) = (0.784, 0.094, 0.54, 0.01)$. In grey, the evolution of various other orbits are shown to indicate the phase space structure. The time-evolution of the $\log_{10} X_1$ (b), $\log_{10}$ SALI (c), $\log_{10} D_L^1$ (d), $\log_{10} R_L^1$ (e), and $\log_{10} S_L^1$ (f) values for the regular and chaotic orbits from (a). The D_L^1, R_L^1, and S_L^1 indices are evaluated along the x_1 direction with $\sigma = 10^{-3}$.

form a ring-like structure, while the red points appear randomly scattered around six lobes (at later times the chaotic orbit enters the chaotic sea, but as this is a 4D subspace, projecting the evolution on the plane hides other regular regions). From the time evolution of these orbits' ftmLE, X_1, [Fig. 4.13(b)] for $T = 10^4$ iterations, we see that the X_1 values for the regular orbit decrease proportionally to $\ln(T)/T$ while for the chaotic orbit the ftmLE saturates to a positive constant, following (2.55). In Fig. 4.13(c) we see that the SALI values of the regular orbit remain practically constant while they start decreasing exponentially fast at about $T \gtrsim 500$ for the chaotic orbit, as expected from (2.52). Both the ftmLE and the SALI only reveal the chaotic nature of the orbit at far later times than in the Hénon-Heiles system [Figs. 4.3(b) and (c)] and the 2D standard map [Figs. 4.8(b) and (c)], with the X_1 value suddenly increasing and the SALI only reaching $\log_{10}$ SALI $= -16$

at about $T = 4,000$. Figures 4.13(d)-(f) show the evolution of the $\log_{10} D_L^1$ (d), $\log_{10} R_L^1$ (e), and $\log_{10} S_L^1$ (f) evaluated along the x_1 direction with $\sigma = 10^{-3}$ for both orbits. We see that the two orbits can be distinguished at $T = 2,000$ by the large differences in their index values, which we also saw at earlier times in Figs. 4.3(d)-(f) and 4.8(d)-(f). The behaviour of the indicators for the regular and chaotic orbits are typical and are seen for other orbits as well.

4.3.1 Dynamics on a 2D subspace

Having verified that the indicators D_L^n, R_L^n, and S_L^n behave as expected for individual cases, we now investigate their ability to correctly characterise large ensembles of orbits. To begin this study, we consider ICs on 2D subspaces of the 4D phase space. In Figs. 4.14(a)-(c) the ICs considered, on an evenly spaced grid on the intervals $x_1, x_2 \in [0, 1)$, while $x_3 = 0.54$ and $x_4 = 0.01$ remain fixed, for the 4D map with $K = 1.5$ and $B = 0.08$, are coloured according to their $\log_{10} D_L^2$ (a), $\log_{10} R_L^2$ (b), and $\log_{10} S_L^2$ (c) values after $T = 10^4$ forward iterations of the map. Since the coupling constant B has a rather low value, the phase space on the (x_1, x_2) plane is very similar to that of the 2D map with the same K value. We note that chaotic orbits of the 4D map take longer to reveal their nature than those of the 2D map (as we see in Fig. 4.13), hence a total of $T = 10^4$ forward iterations are used in the computations as opposed to $T = 1,000$ for the 2D standard map. The normalised distributions of the $\log_{10} D_L^2$, $\log_{10} R_L^2$ and $\log_{10} S_L^2$ values are shown in Figs. 4.14(d)-(f) respectively, with appropriate threshold values, for identifying regular and chaotic orbits using these indices, indicated by the dashed, vertical, red lines at $\log_{10} D_L^2 = -2.4$, $\log_{10} R_L^2 = -3.6$, and $\log_{10} S_L^2 = 7.1$. The characterisation of the ICs, made by the D_L^2, R_L^2, and S_L^2 methods using these thresholds, is compared to that performed by the SALI at the same number of total forward iterations $T = 10^4$. We note that the threshold used for the SALI to distinguish between regular and chaotic orbits was set to SALI $= 10^{-8}$, as was also done for the Hénon-Heiles system (see Section 4.1.1). The total percentage of orbits which are correctly identified as regular or chaotic are $P_A \approx 94.2\%$ (D_L^2), $P_A \approx 95.2\%$ (R_L^2), and $P_A \approx 96.7\%$ (S_L^2). In Figs. 4.14(g)-(i) we show the points which are mischaracterised by the D_L^2, R_L^2, and S_L^2 indices. Points which the SALI identifies as chaotic, but the indicators incorrectly characterise as regular, are coloured red, while those falsely identified as chaotic are coloured light-blue.

From Fig. 4.14(g) we see that the D_L^2 indicator fails to correctly categorise a large number of chaotic orbits at the edges of the large regular regions, as we have seen in similar studies for the Hénon-Heiles system (Section 4.1.1) and the 2D standard map (Section 4.2.1). The R_L^2 and S_L^2 indices [Figs. 4.14(h) and (i) respectively] primarily mischaracterise orbits with ICs in the regular regions, something we had not seen in the two previous cases [see the results presented in Figs. 4.4(h)

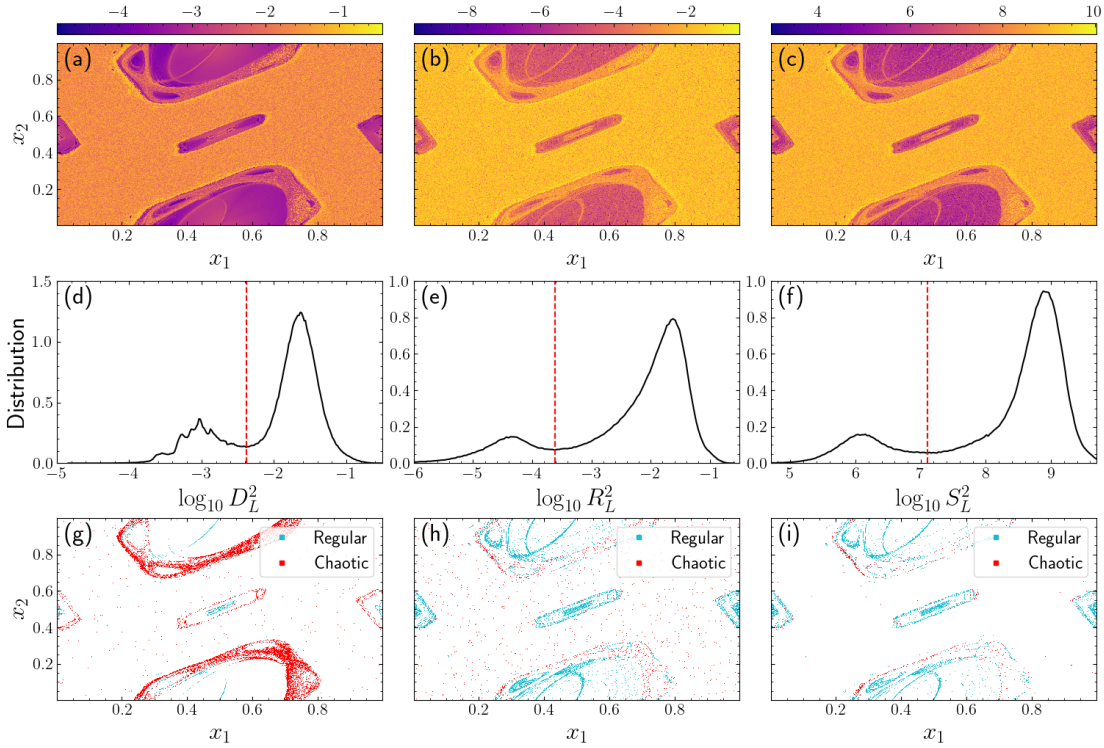

Figure 4.14: Results obtained for orbits of the 4D standard map (4.5) with $K = 1.5$ and $B = 0.08$ having their ICs on an evenly distributed $1,000 \times 1,000$ grid of the 2D subspace (x_1, x_2) and $x_3 = 0.54$, $x_4 = 0.01$. The ICs are coloured according to their (a) $\log_{10} D_L^2$ (4.2), (b) $\log_{10} R_L^2$ (4.3), and (c) $\log_{10} S_L^2$ (4.4) values after $T = 10^4$ forward iterations of the map using the colour scale at the top of each panel. Normalised distributions of the $\log_{10} D_L^2$ (d), $\log_{10} R_L^2$ (e), and $\log_{10} S_L^2$ (f) values of the orbits considered in (a)-(c). The values $\log_{10} D_L^2 = -2.4$, $\log_{10} R_L^2 = -3.6$ and, $\log_{10} S_L^2 = 7.1$ are respectively denoted by a red dashed line as appropriate threshold values to distinguish between regular and chaotic orbits. The set of ICs which are incorrectly characterised by the D_L^2, R_L^2, and S_L^2 indicators, according to the classification obtained by the SALI method computed for $T = 10^4$ forward iterations, are shown in panels (g)-(i). Light-blue points correspond to regular orbits which are falsely identified as chaotic and red points to chaotic orbits which are incorrectly identified as regular.

and (i) as well as Figs. 4.9(h) and (i)]. The accuracy of the characterisations made by the LDs-based chaos diagnostics are however very high, indicating that these indicators can be used to successfully investigate the dynamics of 2D subspaces of the 4D map.

4.3.2 Investigating the effect of various factors on the performance of the LDs-based chaos diagnostics

The effect of the total number of map iterations T and grid spacing σ on the distributions of the LDs-based indices is shown in Fig. 4.15, where the distributions of the indicator values are plotted for three different total map iterations with $\sigma = 10^{-3}$ [Figs. 4.15(a)-(c)] and for three grid spacings for a fixed $T = 1,000$ [Figs. 4.15(d)-(f)]. The ICs of the ensemble of orbits we consider in this figure are on the same 2D subspace as in Fig. 4.14. We indicate the threshold values to distinguish between regular and chaotic motion by dashed, vertical lines, coloured according to the corresponding distribution. The change in the shape and positions of the distributions due to the change in T and σ are similar to the results presented in Figs. 4.5 and 4.10, with the two peaks growing more distinct as T is increased and σ is decreased. Additionally, the positions of the distribution of the $\log_{10} D_L^2$ and $\log_{10} R_L^2$ values do not vary greatly while the $\log_{10} S_L^2$ values increase for greater T and smaller σ. Because the parameter effects on the distributions of the indices are consistent throughout the results presented in Figs. 4.5, 4.10 and 4.15, we conclude that they are general features of the indicators, which we expect to see in generic conservative dynamical systems.

We study the effect of T and σ on the percentage accuracy P_A of the LDs-based methods for the 4D map (4.5) in Fig. 4.16. As we did in Figs. 4.6 and 4.11, we compute the P_A of the indices at ten different total iterations and four different grid spacings. The ICs of the orbits we consider lie on the plane investigated in Fig. 4.14. From this figure, we see that the indicators are more accurate at identifying chaos for a larger number of iterations and smaller grid spacings. These results are consistent with those of Figs. 4.6 and 4.11. Due to the chaotic orbits of the 4D map taking long times to reveal their dynamics (take for example the orbit under consideration in Fig. 4.13) the LDs-based chaos diagnostics should be evaluated at long times as well [consider the significant increase in accuracy we see for the D_L^2 index from $T = 2,500$ to $T = 5,000$ in Fig. 4.16(a)]. At larger T, all indicators are exceptionally accurate with $P_A \gtrsim 90\%$, demonstrating their ability to accurately study the chaotic dynamics of 2D subspaces of higher-dimensional systems.

In our study of a 2D subspace (x_1, x_2) with $x_3 = 0.54$, $x_4 = 0.01$ of the 4D map (4.5), we computed the D_L^n, R_L^n, and S_L^n indices for order $n = 2$. However, since

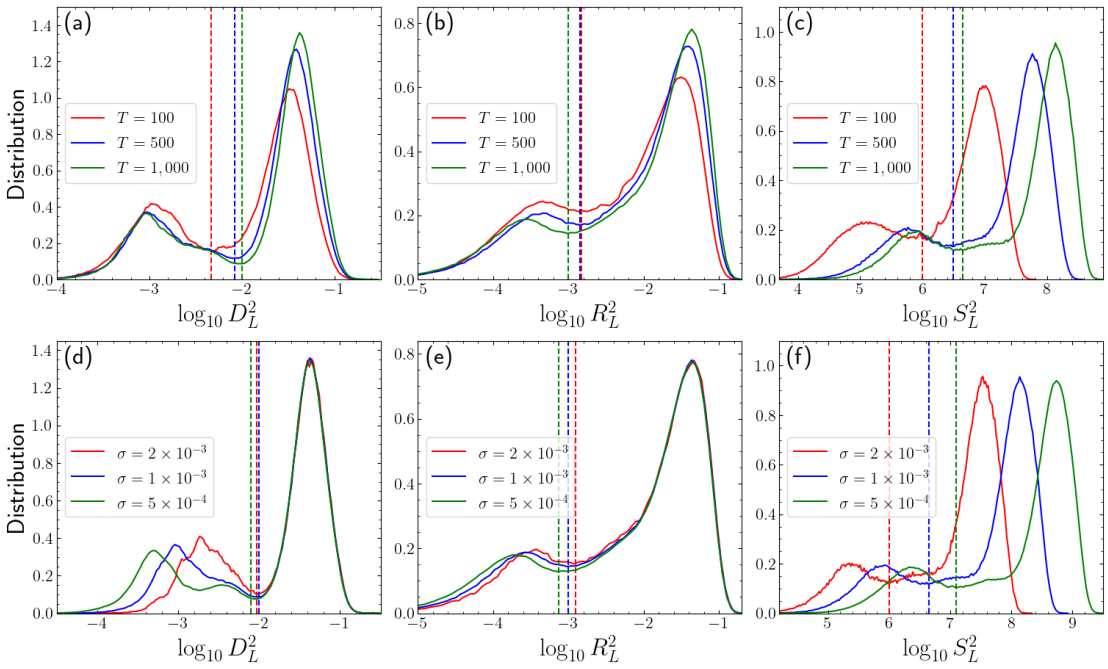

Figure 4.15: (a)-(c) The normalised distributions of the $\log_{10} D_L^2$ (a), $\log_{10} R_L^2$ (b), and $\log_{10} S_L^2$ (c) values for the 4D map (4.5) on the same subspace as in Fig. 4.14, for a fixed grid spacing $\sigma = 10^{-3}$ and three different total iterations of $T = 100$, 500, and 1,000. (d)-(f) the same as (a)-(c) but the number of total iterations is kept fixed at $T = 1,000$ and instead σ is varied to $\sigma = 2 \times 10^{-3}$, 1×10^{-3} and 5×10^{-4}. The threshold value to discriminate between chaotic and regular motion of each distribution is shown as a dashed, vertical line in the same colour as the corresponding distribution.

the map is a 4D system, orders of $n = 1, 3$ or 4 could be used in the calculation of the indicators as well. As the order is increased, we consider more nearby orbits in the computations of the LDs-based chaos diagnostics. Since, however, the deviation vectors of chaotic orbits will all grow in the direction corresponding to the mLCE, increasing the order of the indices would not necessarily lead to a better characterisation of an orbit's nature. Furthermore, an increase in the order would come with the drawback of an increase in CPU time, as we need to calculate the LDs for additional grid points. Let us note that computing the three indices of an individual orbit for $n = k > 1$, takes k times longer than computing the indicators for $n = 1$.

We show in Fig. 4.17 the distributions of the $\log_{10} D_L^n$, $\log_{10} R_L^n$, and $\log_{10} S_L^n$ values for the same set of ICs that were considered in Fig. 4.14, for $n = 1, 2, 3$, and 4. For $n = 1$, the indicators are evaluated along the x_1 direction, for $n = 2$

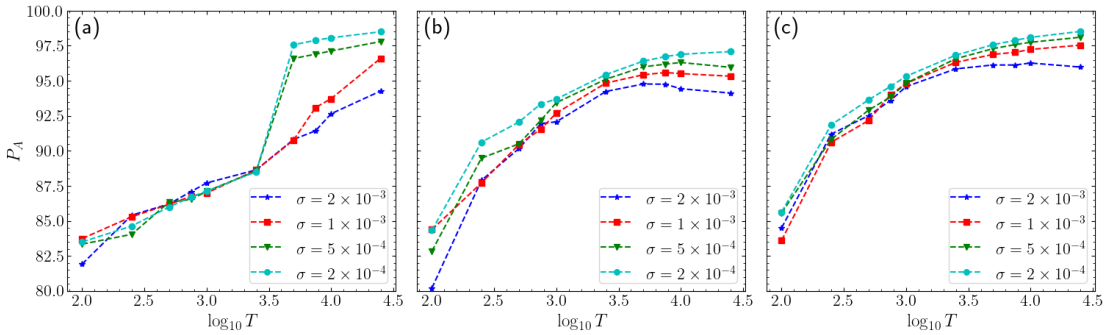

Figure 4.16: The percentage of correctly characterised orbits P_A when compared with the classification obtained by the SALI evaluated at $T = 10^4$ of the D_L^2 (a), R_L^2 (b) and S_L^2 (c) indices for a total of ten different final forward iterations T of the map and four different grid spacings σ. ICs were computed for the 4D standard (4.5) map on the same subspace as in Fig. 4.14, with the total number of ICs corresponding to an evenly distributed grid on these intervals using the appropriate grid spacing.

along the x_1 and x_2 directions, for $n = 3$ in the x_1, x_2, and x_3 directions, and for $n = 4$ all coordinate directions are used. From the results in Fig. 4.17 we see that for all three indices the positions of the regular and chaotic peaks remain at the same location. In fact, for the R_L^n index, n seems to have no impact on the shape of the distributions at all. For the $\log_{10} D_L^n$ and $\log_{10} S_L^n$ values, the peaks become more distinct as n is increased, with the distance between them increasing. Since there are only small changes in the positions and the shapes of the distributions, the associated threshold values for the indices also do not change greatly.

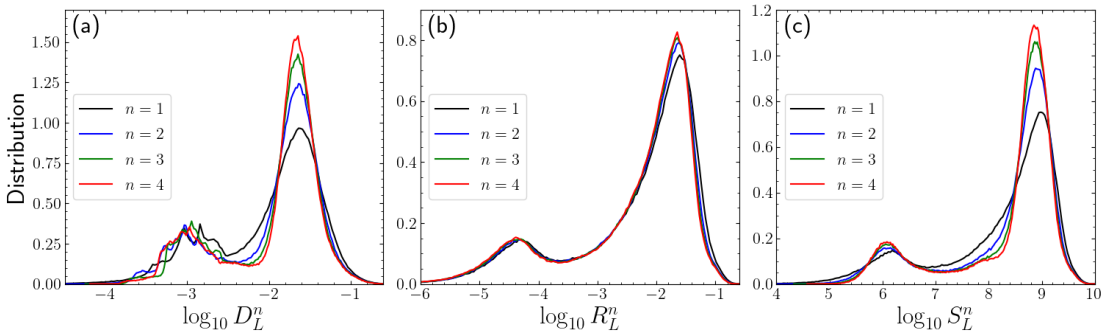

Figure 4.17: The distributions of the $\log_{10} D_L^n$ (a), $\log_{10} R_L^n$ (b), and $\log_{10} S_L^n$ (c) values for $n = 1, 2, 3, 4$, for orbits whose ICs are located on the same grid as in Fig. 4.14 for $\tau = 1,000$.

In order for us to determine the effect of n on the accuracy of the indicators, we

compute the related P_A results for the four n values on six different 2D subspaces of the system's phase space. The six 2D subspaces we consider are the (x_1, x_2); (x_1, x_3); (x_1, x_4); (x_2, x_3); (x_2, x_4); and (x_3, x_4) planes, with the other two variables fixed at $x_1 = 0.6$, $x_2 = 0.2$, $x_3 = 0.54$, and $x_4 = 0.01$, depending on the plane under consideration. These ensembles of orbits respectively consist of $P_C \approx 80.8\%$; $P_C \approx 94.6\%$; $P_C \approx 93.3\%$; $P_C \approx 87.2\%$; $P_C \approx 84.8\%$; and $P_C \approx 89.5\%$ chaotic orbits as characterised by the SALI at $T = 10^4$.

The D_L^n, R_L^n, and S_L^n indices are evaluated along the following directions for the different orders: at $n = 1$ along the coordinate x_i with the lower index i of the plane under consideration; in the directions of the two coordinates of the plane for $n = 2$; along the directions of the coordinates of the plane as well as that of the lower index fixed coordinate not on the plane for $n = 3$; and along all coordinate directions for $n = 4$. For example, let us consider the (x_2, x_4) plane. This plane consists of ICs on the intervals $x_2, x_4 \in [0, 1)$ with $x_1 = 0.6$ and $x_3 = 0.54$ fixed. We evaluate the three indices along the x_2 direction for $n = 1$, the x_2 and x_4 directions for $n = 2$, and the x_1, x_2, and x_4 directions for $n = 3$. For each plane and n, the distributions of the indicators are created, and the thresholds used to distinguish between regular and chaotic orbits selected as the minimum of the distribution between the two peaks.

In Fig. 4.18, the P_A is shown for the D_L^n (a), R_L^n (b), and S_L^n (c) indices for the six slices. For both the D_L^n and R_L^n methods, the accuracy stays approximately constant for all values of n, with a high accuracy of $P_A \gtrsim 90\%$ for all subspaces. An increase in accuracy can be seen from $n = 1$ to $n = 2$ for the S_L^n, but for $n \geq 2$ the accuracy remains practically constant. This information would suggest that $n = 2$ is sufficient for the evaluation of the LDs-based chaos diagnostics to achieve an accurate characterisation of the chaotic or regular nature of orbits in high-dimensional systems.

Furthermore, in Fig. 4.19 we show the percentage accuracy P_A of the indices for $n = 2$ with respect to the total percentage of chaotic orbits P_C for the six subspaces we considered in Fig. 4.18. We see that the indicators categorise more orbits correctly for the more chaotic planes, as we had demonstrated for the Hénon-Heiles system and 2D standard map in Sections 4.1.2 and 4.2.2 respectively.

4.3.3 Dynamics on a 4D subspace

While the ensembles of ICs studied thus far were on 2D subspaces of the system's 4D phase space, we now apply the D_L^n, R_L^n, and S_L^n indices to a 4D subset of the phase space of the 4D standard map (4.5). The subset under consideration is given by $x_1 \in [0.5, 0.6)$, $x_2 \in [0, 0.1)$, and $x_3, x_4 \in [0, 1)$. This subset constitutes 1% of the full phase space volume of the map and consists of $P_C \approx 83.1\%$ total chaotic orbits, as characterised by the SALI at $T = 10^4$ iterations. Since the results from

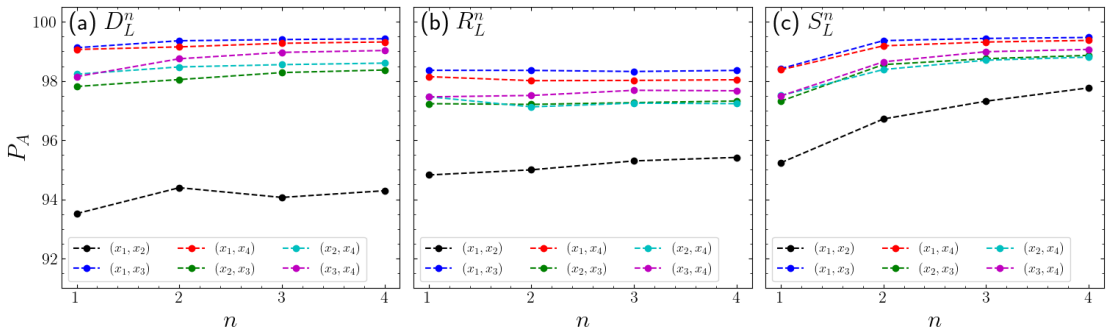

Figure 4.18: The percentage of correctly characterised orbits P_A of the D_L^n (a), R_L^n (b), and S_L^n (c) for $n = 1, 2, 3$, and 4, for a total of six different planes of the 4D map (4.5). The indicators were evaluated at $T = 1,000$ on a grid of $1,000 \times 1,000$ evenly distributed ICs on each respective plane.

Fig. 4.18 indicate that $n = 2$ is sufficient for an accurate evaluation of the chaoticity using the LDs-based indicators, the D_L^2, R_L^2, and S_L^2 indices are computed for an evenly distributed grid of 100^4 ICs on this subset (for each coordinate direction in the subspace 100 ICs are considered) for $T = 10^4$ iterations. The three diagnostics are evaluated along the x_1 and x_2 directions with the grid spacing set at $\sigma = 10^{-3}$.

In Fig. 4.20 the distributions of the $\log_{10} D_L^2$ (a), $\log_{10} R_L^2$ (b), and $\log_{10} S_L^2$ (c) values for the considered ICs are shown with appropriate threshold values, for discriminating between regular and chaotic orbits, at $\log_{10} D_L^2 = -2.7$, $\log_{10} R_L^2 = -3.6$, and $\log_{10} S_L^2 = 5.1$ indicated by the vertical, red, dashed lines. The shape of the distributions are similar to what was seen from the previous cases [Figs. 4.4, 4.9 and 4.14], with two well-formed peaks at low and high indicator values corresponding to the regular and chaotic orbits of the map respectively. Using the selected thresholds to characterise the orbits and comparing this characterisation to that obtained by the SALI at $T = 10^4$, we find that the indicators characterise $P_A \approx 96.7\%$ (D_L^2), $P_A \approx 96.4\%$ (R_L^2), and $P_A \approx 97.6\%$ (S_L^2) of orbits correctly. We note that the LDs-based chaos identifier give a very accurate categorisation of the chaoticity of the orbits in this 4D subspace where, as opposed to the results presented in Sections 4.1.1, 4.2.1, and 4.3.1, we cannot use them to visualise the dynamics. This analysis demonstrates the ability of these indicators to correctly characterise the nature of orbits of high-dimensional systems using the same methodology as in low-dimensional systems. From the investigations performed in this section, as well as Sections 4.1 and 4.2, we conclude that the LDs-based indices can be used as accurate chaos diagnostics for both lower and higher-dimensional, conservative dynamical systems.

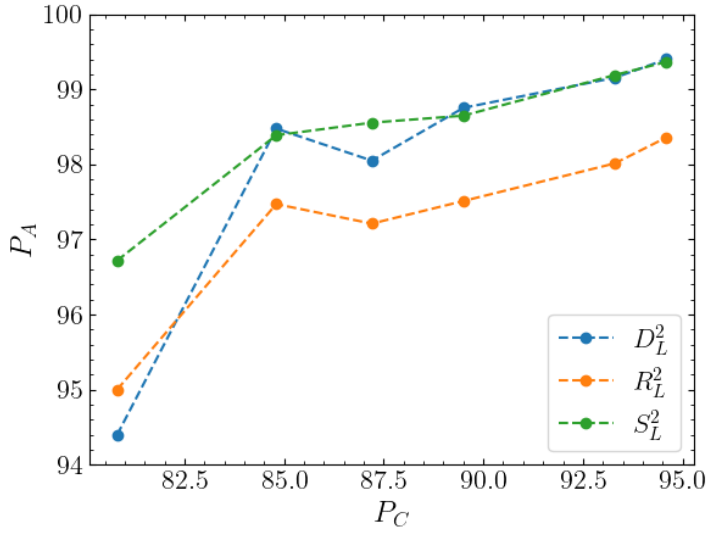

Figure 4.19: The percentage of correctly characterised orbits P_A of the D_L^2, R_L^2, and S_L^2 indicators for the six different planes considered in Fig. 4.18, with respect to the total percentage of ICs P_C which correspond to chaotic orbits.

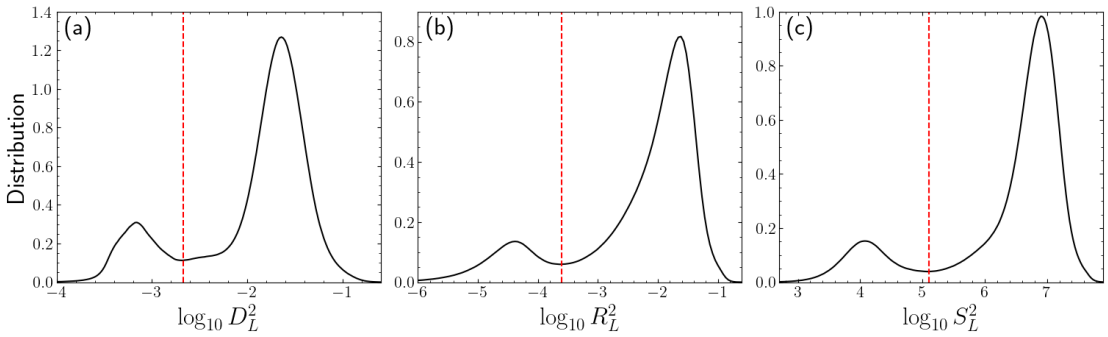

Figure 4.20: The distributions of the $\log_{10} D_L^2$ (a), $\log_{10} R_L^2$ (b), and $\log_{10} S_L^2$ (c) values for the 4D standard map (4.5) with $K = 1.5$ and $B = 0.08$ on a grid of 100^4 evenly distributed ICs on the intervals $x_1 \in [0.5, 0.6)$, $x_2 \in [0, 0.1)$, and $x_3, x_4 \in [0, 1)$ for $T = 10^4$. Appropriate threshold values, to distinguish between regular and chaotic motion, for each distribution are indicated as red, dashed lines at $\log_{10} D_L^2 = -2.7$, $\log_{10} R_L^2 = -3.6$, and $\log_{10} S_L^2 = 5.1$.

Chapter 5

Conclusions

In our work, several numerical investigations were performed to study the ability of LDs in revealing the characteristics of dynamical systems. In the first two chapters of this thesis, an overview of the theory of nonlinear dynamics was given, with a particular focus on Hamiltonian systems and symplectic maps, as these are the types of models on which we focused our attention. Due to the nonlinear nature of a large number of these dynamical systems, analytical solutions do not exist in general, so a variety of numerical techniques have been developed to study them. These numerical methods rely on accurate integrators, two types of which (a sixth-order RK and a fourth-order symplectic integrator) were implemented in this thesis. The most popular qualitative method for studying low-dimensional, time-continuous systems is the construction of the related PSS, which depicts the orbits of a $2N$D phase space on a $2(N-1)$D subspace. While this method offers a great deal of information for low-dimensional systems, for a more quantitative analysis, a variety of chaos indicators, like the mLCE or SALI, are used. The mLCE measures the growth/shrinking of the deviation vectors of an orbit to characterise its chaoticity. While the mLCE is one of the most popular chaos indicators, for a faster characterisation of the orbit's nature, the SALI, which measures the alignment of two deviation vectors, is used.

The primary computational method studied in this thesis was the recently developed phase space visualisation technique, the method of LDs. This method gives a qualitative description of the system's phase space, allowing for the identification of fixed points, periodic orbits and their associated manifolds.

The main results of this thesis were presented in Chapters 3 and 4. In Chapter 3, LDs were applied to study a Hamiltonian system modelling the movement of stars in a galaxy (3.5). This was a novel application of LDs to galactic dynamic models, demonstrating the applicability and behaviour this method allows for such systems. The LDs were applied to the system at various energies and the behaviour of the method for different integration times and for visualising

the manifolds of the system, discussed. A key feature of galactic models is the ability of stars to escape from the galaxy through the phase space region where Lyapunov orbits exist. The LDs were utilised to visualise the intersection of the Lyapunov orbits' manifolds with the configuration space of the system. From the approximate location of the Lyapunov orbits, identified by the LDs plots, a quantitative method was then used to accurately find the locations of the orbits. Our work demonstrates the ability of the LDs to study galactic models and reveal their phase space structures.

In Chapter 4, three chaos indicators, the D_L^n (4.2), R_L^n (4.3), and S_L^n (4.4) indices, which use calculations of LDs on a grid of ICs to quantitatively characterise orbits as either regular or chaotic, were discussed. The ability of the D_L^n, R_L^n, and S_L^n indicators to efficiently distinguish between individual regular and chaotic orbits was demonstrated for three basic dynamical systems: the Hénon-Heiles Hamiltonian (2.16), the 2D standard map (2.57), and the 4D standard map (4.5). These models are respectively prototypical examples of: a low-dimensional, conservative, continuous system; a low-dimensional, symplectic map; and a high-dimensional, symplectic map. The three indicators were shown to be capable of discriminating between individual regular and chaotic orbits for all three test systems, and they were also applied to investigate large ensembles of ICs from these test systems. For the performance of global analyses, the orbits are characterised as regular if their D_L^n, R_L^n, and S_L^n values are below a threshold value, defined as the minimum between the regular and chaotic peaks of the indicator distributions, and as chaotic otherwise. The characterisation made by the D_L^n, R_L^n, and S_L^n indices was then compared to the one obtained by the SALI method, with the indicators agreeing with the SALI for $\gtrsim 90\%$ of cases. This demonstrates that these indicators can be used to give an accurate estimate of the chaoticity of both low and high-dimensional conservative systems. Additionally, since these indicators do not rely on the computations of the variational equations or the tangent map (for continuous and discrete time settings respectively), they are both easier to implement and are computed faster than other standard chaos detection techniques.

The effect of various parameters, such as the final integration time for continuous time systems or the total number of iterations for maps, the grid spacing, the degree of chaos and the order n of the indices D_L^n, R_L^n, and S_L^n, was also discussed. These parameters had the following effects on the indicators' accuracy:

1. As the integration time or total number of iterations is increased, the indicators' accuracy P_A, in general, increases as well [see the results presented in Figs. 4.6, 4.11, 4.12(c)-(d), and 4.16].

2. The accuracy increases as the size of the grid spacing is decreased; this however comes with the drawback of the additional CPU time required for a smaller grid spacing [Figs. 4.6, 4.11, 4.12(c)-(d), and 4.16].

3. From the discussions in Sections 4.1, 4.2, 4.3.1, and 4.3.2 we conclude that all three indicators perform better for more chaotic systems, i.e., systems where the total percentage of chaotic orbits P_C is higher. The D_L^n index has the drawback of misidentifying numerous orbits on the edges of regular islands, while the R_L^n method identifies more points in the chaotic sea incorrectly. The S_L^n indicator finds a middle-ground between the other two, not having as obvious drawbacks for certain regions of the phase space (this can be seen from the results presented in Figs. 4.4, 4.7, 4.9, and 4.14).

4. The order, n, used in the evaluation of the D_L^n, R_L^n, and S_L^n indices was found to have an insignificant impact in the accuracy of the indicators, with $n = 2$ being sufficient in achieving an accurate characterisation, even for high-dimensional phase space subsets (see the results presented in Fig. 4.18 and Section 4.3.3).

This investigation demonstrates how these newly introduced chaos detection diagnostics can be applied to generic conservative, dynamical systems.

Bibliography

[1] J. Madrid and A. M. Mancho. Distinguished trajectories in time dependent vector fields. *Chaos: An Interdisciplinary Journal of Nonlinear Science*, 19(1), 2009.

[2] M. Katsanikas and P. A. Patsis. The structure of invariant tori in a 3D galactic potential. *International Journal of Bifurcation and Chaos*, 21(02), 2011.

[3] J. Daquin, R. Pédenon-Orlanducci, M. Agaoglou, G. García-Sánchez, and A. M. Mancho. Global dynamics visualisation from Lagrangian Descriptors. Applications to discrete and continuous systems. *Physica D: Nonlinear Phenomena*, 442(15), 2022.

[4] M. Hénon and C. Heiles. The applicability of the third integral of motion: Some numerical experiments. *The Astronomical Journal*, 69(1), 1964.

[5] B. V. Chirikov. A universal instability of many-dimensional oscillator systems. *Physics reports*, 52(5), 1979.

[6] H. Kantz and P. Grassberger. Internal Arnold diffusion and chaos thresholds in coupled symplectic maps. *Journal of Physics A: Mathematical and General*, 21(3), 1988.

[7] Ch. Skokos. Alignment indices: a new, simple method for determining the ordered or chaotic nature of orbits. *Journal of Physics A*, 34(47), 2001.

[8] M. Hillebrand, S. Zimper, A. Ngapasare, M. Katsanikas, S. Wiggins, and Ch. Skokos. Quantifying chaos using Lagrangian descriptors. *Chaos: An Interdisciplinary Journal of Nonlinear Science*, 32(12), 2022.

[9] S. Zimper, A. Ngapasare, M. Hillebrand, M. Katsanikas, S. Wiggins, and Ch. Skokos. Performance of chaos diagnostics based on Lagrangian descriptors. application to the 4D standard map. 2023. arXiv:2305.00978.

[10] J. Guckenheimer and P. Holmes. *Nonlinear oscillations, dynamical systems, and bifurcations of vector fields*. Number 42 in Applied mathematical sciences. Springer, 7th edition, 2002.

[11] H. Poincaré. Chapitre II. Etude des surfaces asymptotiques. *Acta Mathematica*, 13(1-2), 1900.

[12] A. J. Lichtenberg and M. A. Lieberman. *Regular and Chaotic Dynamics*, volume 38. Springer, 2 edition, 1992.

[13] V.I. Arnold. *Mathematical Methods Of Classical Mechanics*, volume 60 of *Graduate Texts in Mathematics*. Springer, 2nd edition, 1989.

[14] E. Hairer, C. Lubich, and G. Wanner. *Geometric numerical integration*, volume 31 of *Springer Series in Computational Mathematics*. Springer-Verlag, Berlin, 2nd edition, 2006.

[15] H. A. Luther. An explicit sixth-order Runge-Kutta formula. *Mathematics of Computation*, 22(102), 1968.

[16] S. Blanes, F. Casas, A. Farrés, J. Laskar, J. Makazaga, and A. Murua. New families of symplectic splitting methods for numerical integration in dynamical astronomy. *Applied Numerical Mathematics*, 68(6), 2013.

[17] R. Burden and J. Douglas Faires. *Numerical Analysis*, volume 915. Brooks/Cole, Cengage Learning, 9th edition, 2010.

[18] Proceedings of EPAC 2002. *Application of a New Class of Symplectic Integrators to Accelerator Tracking*, 2002.

[19] É. Forest. Geometric integration for particle accelerators. *Journal of Physics A: Mathematical and General*, 39(19), 2006.

[20] Senyange, B. and Skokos, Ch. Computational efficiency of symplectic integration schemes: application to multidimensional disordered Klein-Gordon lattices. *The European Physical Journal Special Topics*, 227(5-6), 2018.

[21] C. Danieli, B. M. Manda, T. Mithun, and Ch. Skokos. Computational efficiency of numerical integration methods for the tangent dynamics of many-body Hamiltonian systems in one and two spatial dimensions. *Mathematics in Engineering*, 1(3), 2019.

[22] H. Yoshida. Construction of higher order symplectic integrators. *Physics Letters A*, 150(5), 1990.

[23] J. Hadamard. Les surfaces à courbures opposées et leurs lignes géodésiques. *Journal de Mathématiques Pures et Appliquées*, 4, 1898.

[24] E. N. Lorenz. Deterministic Nonperiodic Flow. *Journal of Atmospheric Sciences*, 20(2), 1963.

[25] R. Devaney. *An Introduction to Chaotic Dynamical Systems, Second Edition.* Avalon Publishing, 1989.

[26] M. Hénon. On the numerical computation of Poincaré maps. *Physica D: Nonlinear Phenomena*, 5(2), 1982.

[27] Ch. Skokos and E. Gerlach. Numerical integration of variational equations. *Physical Review E*, 82(3), 2010.

[28] E. Gerlach and Ch. Skokos. Comparing the efficiency of numerical techniques for the integration of variational equations. *Discrete and Continuous Dynamical Systems- Series A*, 2011.

[29] A. M. Lyapunov. The general problem of the stability of motion. *International journal of control*, 55(3), 1992.

[30] V. I. Oseledec. A multiplicative ergodic theorem. Liapunov characteristic number for dynamical systems. *Transactions of the Moscow Mathematical Society*, 19, 1968.

[31] U. Parlitz. *Estimating Lyapunov Exponents from Time Series*, volume 915 of *Lecture Notes in Physics*, pages 1–34. Springer, 2016.

[32] Ch. Skokos. *The Lyapunov Characteristic Exponents and Their Computation*, volume 790, pages 63–135. Springer, 2010.

[33] G. Benettin, L. Galgani, A. Giorgilli, and J. M. Strelcyn. Lyapunov Characteristic Exponents for smooth dynamical systems and for Hamiltonian systems; a method for computing all of them. Part 1: Theory. *Meccanica*, 15(1), 1980.

[34] G. Benettin, L. Galgani, A. Giorgilli, and J. M. Strelcyn. Lyapunov Characteristic Exponents for smooth dynamical systems and for hamiltonian systems; a method for computing all of them. Part 2: Numerical application. *Meccanica*, 15, 1980.

[35] I. I. Shevchenko and V. V. Kouprianov. On the chaotic rotation of planetary satellites: The Lyapunov spectra and the maximum Lyapunov exponents. *Astronomy & Astrophysics*, 394(2), 2002.

[36] V. Achilleos, G. Theocharis, and Ch. Skokos. Chaos and Anderson-like localization in polydisperse granular chains. *Physical Review E*, 97(4), 2018.

[37] A. Ngapasare, G. Theocharis, O. Richoux, Ch. Skokos, and V. Achilleos. Chaos and Anderson localization in disordered classical chains: Hertzian versus Fermi-Pasta-Ulam-Tsingou models. *Physical Review E*, 99(3), 2019.

[38] M. Hillebrand, G. Kalosakas, A. Schwellnus, and Ch. Skokos. Heterogeneity and chaos in the Peyrard-Bishop-Dauxois DNA model. *Physical Review E*, 99(2), 2019.

[39] M. Hillebrand, B. M. Manda, George Kalosakas, Enrico Gerlach, and Ch Skokos. Chaotic dynamics of graphene and graphene nanoribbons. *Chaos: An Interdisciplinary Journal of Nonlinear Science*, 30(6), 2020.

[40] B. Wang, B. Chen, G. Wang, R. Li, C. Wen, J.and Lu, R. Tian, and J. Deng. Back propagation (BP) neural network prediction and chaotic characteristics analysis of free falling liquid film fluctuation on corrugated plate wall. *Annals of Nuclear Energy*, 148, 2020.

[41] Y. Q. Lei, X. H. Ge, and C. Ran. Chaos of particle motion near a black hole with quasitopological electromagnetism. *Physical Review D*, 104(4), 2021.

[42] A. Ngapasare, G. Theocharis, O. Richoux, Ch. Skokos, and V. Achilleos. Wave-packet spreading in disordered soft architected structures. *Chaos: An Interdisciplinary Journal of Nonlinear Science*, 32(5), 2022.

[43] C. Froeschlé, E. Lega, and R. Gonczi. Fast Lyapunov indicators. Application to asteroidal motion. *Celestial Mechanics and Dynamical Astronomy*, 67(1), 1997.

[44] R. Barrio. Sensitivity tools vs. Poincare sections. *Chaos, Solitons & Fractals*, 25(3), 2005.

[45] P. M. Cincotta and C. Simó. Simple tools to study global dynamics in non-axisymmetric galactic potentials - I. *Astronomy and Astrophysics Supplement Series*, 147(2), 2000.

[46] Ch. Skokos, T. C. Bountis, and Ch. Antonopoulos. Geometrical properties of local dynamics in Hamiltonian systems: The Generalized Alignment Index (GALI) method. *Physica D: Nonlinear Phenomena*, 231(1), 2007.

[47] Ch. Skokos, G. Gottwald, and J. Laskar. *Chaos Detection and Predictability*, volume 915 of *Lecture Notes in Physics*. Springer, 2016.

[48] Ch. Skokos, Ch. Antonopoulos, T. C. Bountis, and M. N. Vrahatis. Detecting order and chaos in Hamiltonian systems by the SALI method. *Journal of Physics A: Mathematical and General*, 37(24), 2004.

[49] Ch. Skokos and T. Manos. *The Smaller (SALI) and the Generalized (GALI) Alignment Indices: Efficient Methods of Chaos Detection*, volume 915 of *Lecture Notes in Physics*, pages 129–181. Springer, 2016.

[50] T. Manos, Ch. Skokos, E. Athanassoula, and T. Bountis. Studying the global dynamics of conservative dynamical systems using the SALI chaos detection method. *Nonlinear Phenomena in Complex Systems*, 11, 2008.

[51] Y. G. Petalas, C. G. Antonopoulos, T. Bountis, and M. N. Vrahatis. Evolutionary methods for the approximation of the stability domain and frequency optimization of conservative maps. *International Journal of Bifurcation and Chaos*, 18, 2008.

[52] J. Boreux, T. Carletti, Ch. Skokos, and M. Vittot. Hamiltonian control used to improve the beam stability in particle accelerator models. *Communications in Nonlinear Science and Numerical Simulation*, 17(4), 2012.

[53] P. Stránský, P. Hruška, and P. Cejnar. Quantum chaos in the nuclear collective model: Classical-quantum correspondence. *Physical Review E*, 79(4), 2009.

[54] L. M. Saha and N. Sahni. Chaotic evaluations in a modified coupled logistic type predator-prey model. *Applied Mathematical Sciences*, 6, 2012.

[55] T. Manos, T. Bountis, and Ch. Skokos. Interplay between chaotic and regular motion in a time-dependent barred galaxy model. *Journal of Physics A: Mathematical and Theoretical*, 46(25), 2013.

[56] D. D. Carpintero, J. C. Muzzio, and H. D. Navone. Models of cuspy triaxial stellar systems – III. The effect of velocity anisotropy on chaoticity. *Monthly Notices of the Royal Astronomical Society*, 438(4), 2014.

[57] N. Kyriakopoulos, V. Koukouloyannis, Ch. Skokos, and P. G. Kevrekidis. Chaotic behavior of three interacting vortices in a confined Bose-Einstein condensate. *Chaos: An Interdisciplinary Journal of Nonlinear Science*, 24(2), 2014.

[58] C. Mendoza and A. M. Mancho. Hidden geometry of ocean flows. *Physical Review Letters*, 105(3), 2010.

[59] G. T. Craven and R. Hernandez. Lagrangian descriptors of thermalized transition states on time-varying energy surfaces. *Physical Review Letter*, 115(14), 2015.

[60] G. T. Craven and R. Hernandez. Deconstructing field-induced ketene isomerization through Lagrangian descriptors. *Physical Chemistry Chemical Physics*, 18(5), 2016.

[61] G. T Craven, A. Junginger, and R. Hernandez. Lagrangian descriptors of driven chemical reaction manifolds. *Physical Review E*, 96(2), 2017.

[62] A. Junginger and R. Hernandez. Lagrangian descriptors in dissipative systems. *Physical Chemistry Chemical Physics*, 18(44), 2016.

[63] V. J. García-Garrido and J. García-Luengo. Painting the phase space of dissipative systems with Lagrangian descriptors. *Communications in Nonlinear Science and Numerical Simulation*, 104, 2022.

[64] F. Balibrea-Iniesta, C. Lopesino, S. Wiggins, and A. M. Mancho. Lagrangian descriptors for stochastic differential equations: A tool for revealing the phase portrait of stochastic dynamical systems. *International Journal of Bifurcation and Chaos*, 26(13), 2016.

[65] J. Curbelo, C. R. Mechoso, A. M. Mancho, and S. Wiggins. Lagrangian study of the final warming in the southern stratosphere during 2002: Part I. The vortex splitting at upper levels. *Climate Dynamics*, 53(5-6), 2019.

[66] M. Feldmaier, A. Junginger, J. Main, G. Wunner, and R. Hernandez. Obtaining time-dependent multi-dimensional dividing surfaces using Lagrangian descriptors. *Chemical Physics Letters*, 687, 2017.

[67] V. J. García-Garrido, J. Curbelo, A. M. Mancho, S. Wiggins, and C. R. Mechoso. The application of Lagrangian descriptors to 3D vector fields. *Regular and Chaotic Dynamics*, 23(5), 2018.

[68] M. Katsanikas, V. J. García-Garrido, and S. Wiggins. Detection of dynamical matching in a caldera hamiltonian system using Lagrangian descriptors. *International Journal of Bifurcation and Chaos*, 30(09), 2020.

[69] M. Katsanikas, M. Hillebrand, Ch. Skokos, and S. Wiggins. A new type of dynamical matching in an asymmetric Caldera potential energy surface. *Chemical Physics Letters*, 811, 2023.

[70] G. G. Carlo and F. Borondo. Lagrangian descriptors for open maps. *Physical Review E*, 101(2), 2020.

[71] V. J. García-Garrido. An extension of discrete Lagrangian descriptors for unbounded maps. *International Journal of Bifurcation and Chaos*, 30(05), 2020.

[72] A. Darwish, S. Norouzi, G. Di Labbio, and L. Kadem. Extracting Lagrangian coherent structures in cardiovascular flows using Lagrangian descriptors. *Physics of Fluids*, 33(11), 2021.

[73] M. Katsanikas, B. A. Sanjuan, F. G. Montoya, V. J. García-Garrido, and S. Wiggins. Bifurcation study on a degenerate double van der waals cirque potential energy surface using Lagrangian descriptors. *Communications in Nonlinear Science and Numerical Simulation*, 105, 2022.

[74] M. Agaoglou, B. Aguilar-Sanjuan, V. García Garrido, F. González Montoya, M. Katsanikas, V. Krajňák, S. Naik, and S. Wiggins. *Lagrangian Descriptors: Discovery and Quantification of Phase Space Structure and Transport*. 2020.

[75] C. Lopesino, F. Balibrea, S. Wiggins, and A. M. Mancho. Lagrangian descriptors for two dimensional, area preserving, autonomous and nonautonomous maps. *Communications in Nonlinear Science and Numerical Simulation*, 27(1-3), 2015.

[76] C. Lopesino, F. Balibrea-Iniesta, V. J. García Garrido, S. Wiggins, and A. M. Mancho. A theoretical framework for Lagrangian descriptors. *International Journal of Bifurcation and Chaos*, 27(01), 2017.

[77] A. M. Mancho, S. Wiggins, J. Curbelo, and C. Mendoza. Lagrangian descriptors: A method for revealing phase space structures of general time dependent dynamical systems. *Communications in Nonlinear Science and Numerical Simulation*, 18(12), 2013.

[78] A. S. Demian and S. Wiggins. Detection of periodic orbits in Hamiltonian systems using Lagrangian descriptors. *International Journal of Bifurcation and Chaos*, 27(14), 2017.

[79] Matthaios K., V. J. García-Garrido, M. Agaoglou, and S. Wiggins. Phase space analysis of the dynamics on a potential energy surface with an entrance channel and two potential wells. *Physical Review E*, 102(1), 2020.

[80] S. Naik and S. Wiggins. Finding normally hyperbolic invariant manifolds in two and three degrees of freedom with Hénon-Heiles-type potential. *Physical Review E*, 100(2), 2019.

[81] V. J. García-Garrido, S. Naik, and S. Wiggins. Tilting and squeezing: Phase space geometry of Hamiltonian saddle-node bifurcation and its influence on chemical reaction dynamics. *International Journal of Bifurcation and Chaos*, 30(04), 2020.

[82] V. J. García-Garrido, F. Balibrea-Iniesta, S. Wiggins, A. M. Mancho, and C. Lopesino. Detection of Phase Space Structures of the Cat Map with Lagrangian Descriptors. *Regular and Chaotic Dynamics*, 23(6), 2018.

[83] P. Patsis and M. Katsanikas. The phase-space of boxy-peanut and X-shaped bulges in galaxies I. properties of non-periodic orbits. *Monthly Notices of the Royal Astronomical Society*, 445, 2014.

[84] M. Richter, S. Lange, A. Bäcker, and R. Ketzmerick. Visualization and comparison of classical structures and quantum states of four-dimensional maps. *Physical Review E*, 89(2), 2014.

[85] F. Revuelta, R. M. Benito., and F. Borondo. Unveiling the chaotic structure in phase space of molecular systems using Lagrangian descriptors. *Physical Review E*, 99(3), 2019.

[86] Centre for High Performance Computing: https://www.chpc.ac.za.

[87] M. Miyamoto and R. Nagai. Three-dimensional models for the distribution of mass in galaxies. *Publications of the Astronomical Society of Japan*, 27, 1975.

[88] C. Jung and E. E. Zotos. Orbital and escape dynamics in barred galaxies – I. The 2D system. *Monthly Notices of the Royal Astronomical Society*, 457(3), 2016.

[89] G. Contopoulos. *Order and Chaos in Dynamical Astronomy*. Astronomy and Astrophysics Library. Springer Berlin Heidelberg, 1st edition, 2002.

[90] S. Naik, V. J. García-Garrido, and S. Wiggins. Finding NHIM: Identifying high dimensional phase space structures in reaction dynamics using Lagrangian descriptors. *Communications in Nonlinear Science and Numerical Simulation*, 79, 2019.

[91] A. Junginger and R. Hernandez. Uncovering the geometry of barrierless reactions using Lagrangian descriptors. *The Journal of Physical Chemistry B*, 120(8), 2016.

[92] A. Junginger, G. T. Craven, T. Bartsch, F. Revuelta, F. Borondo, R. M. Benito, and R. Hernandez. Transition state geometry of driven chemical reactions on time-dependent double-well potentials. *Physical Chemistry Chemical Physics*, 18(44), 2016.

[93] M. Agaoglou, B. Aguilar-Sanjuan, V. García Garrido, R. García-Meseguer, F. González Montoya, M. Katsanikas, V. Krajňák, S. Naik, and S. Wiggins. *Chemical Reactions: A Journey into Phase Space*. 2019.

[94] G. Contopoulos. Asymptotic curves and escapes in Hamiltonian systems. *Astronomy and Astrophysics*, 231(1), 1990.

[95] G. Contopoulos and K. Efstathiou. Escapes and recurrence in a simple Hamiltonian system. *Celestial Mechanics and Dynamical Astronomy*, 88, 2004.

[96] G. Contopoulos and P. Patsis. Outer dynamics and escapes in barred galaxies. *Monthly Notices of the Royal Astronomical Society*, 369(3), 2006.

[97] J. Montes, F. Revuelta, and F. Borondo. Lagrangian descriptors and regular motion. *Communications in Nonlinear Science and Numerical Simulation*, 102, 2021.

[98] J. Daquin and C. Charalambous. Detection of separatrices and chaotic seas based on orbit amplitudes. *Celestial Mechanics and Dynamical Astronomy*, 135(3), 2023.